UNIVERSITÀ
DEGLI STUDI
DI PADOVA

Sede Amministrativa: Università degli Studi di Padova

Dipartimento di Geoscienze

SCUOLA DI DOTTORATO DI RICERCA IN SCIENZE DELLA TERRA
CICLO XXII

MAGNETOSTRATIGRAPHY AND ROCK-MAGNETISM OF PALEOGENE MARINE SECTIONS FROM THE VENETIAN ALPS (ITALY)

(MAGNETOSTRATIGRAFIA E MAGNETISMO DELLE ROCCE DI SEDIMENTI PALEOGENEICI MARINI AFFIORANTI NELLE ALPI VENETE (ITALIA))

Direttore della Scuola: Ch.mo Prof. Gilberto Artioli
Supervisori: Ch.mo Prof. Domenico Rio
Ch.mo Prof. Giovanni Muttoni

Dottorando: Edoardo Dallanave

Magnetostratigraphy and rock-magnetism of Paleogene marine sections form the Venetian Alps (Italy)

Edoardo Dallanave

Supervisors: Prof. D. Rio
Geosciences Department
University of Padova

Prof. G. Muttoni
Department of Earth Science
University of Milan

Members of the dissertation committee:

Prof. D.V. Kent
Department of Earth and Planetary Science
Rutgers University
Lamont-Doherty Earth Observatory
Palisades, NY 10964

Prof. M. Mattei
Department of Geological Science
University of Roma 3

Prof. C. Stefani
Geosciences Department
University of Padova

...e questo si manifesta per lo ordine delle pietre faldate, che dalla sommità del monte insino al fiume si vede le conrispondenze delle falde essere così da l'un de lati del fiume come dall'altro. Dentro alli termini delle pietre son trovati rari e appaiati gusci, come quelli che furon lasciati dal mare sotterrati vivi dentro al fango, il qual poi si seccò e col tempo petrificò.

Leonardo da Vinci (1452–1519), Codice Leicester

Contents

Abstract

In this thesis, I present the magnetostratigraphy and the rock-magnetic properties from three selected early Paleogene hemipelagic sections (namely the Ardo, the Cicogna, and the Forada sections) from the Venetian Southern Alps (NE Italy). The contribution of this thesis to the present-day knowledge of the early Paleogene time is twofold and is discussed in two parts. In **Part 1** the implications and the improvements of the presented dataset to the current early Paleogene time scale are presented. The magneto-biochronology of the early Paleogene, especially the late Paleocene–early Eocene, is in fact still poorly defined; this is essentially because of the controversial and ambiguous relationships between paleontologic and magnetic events due to the presence of unconformities in several deep-sea and shallow water sections from the literature around the Paleocene–Eocene boundary, and the lack of (magnetic) resolution in the long Chron C24r interval. I present in **Part 1** a detailed magnetostratigraphy across the early Paleocene part of the Ardo section, as well as across the late Paleocene–early Eocene Cicogna section. The sediments of both the Ardo and the Cicogna sections preserved a well-defined record of the geomagnetic reversals, respectively from Chron C29r to C26r, and from Chron C25r to C23r, which allowed the construction of a robust age model by means of magnetostratigraphic correlation to the CK95 (Cande and Kent, 1995) geomagnetic polarity time scale. The dataset of the Cicogna section is also integrated with a detailed calcareous nannoplankton biostratigraphy; several new and potentially useful biohorizons that help refining the chronology of this critical interval of the current time scale of Berggren et al. (1995) were found.

In **Part 2,** rock-magnetic data from the Cicogna and the Forada sections are described. In particular, the data from Cicogna gave me the opportunity to better understand key aspects of the late Paleocene–early Eocene Earth's climate evolution. The late Paleocene–early Eocene climate was characterized by a general warming trend that eventually culminated with the early Eocene climatic optimum (EECO, ~52–50 Ma), which was characterized by globally warm climatic conditions, even at extremely high latitudes. This warming trend was punctuated by several short-lived hyperthermal events, the most prominent of which was the Paleocene–Eocene thermal maximum (PETM), globally marked by a 2‰–4‰ global negative carbon isotope excursion and extensive carbonate dissolution of deep-sea sediments. The early Eocene and PETM warm and humid climates should be characterized by enhanced land weathering rates, which would promote the sequestration of excess the greenhouse CO_2 by chemical weathering of silicates followed by the deposition of carbonates, in accordance with the negative feedback mechanism for the long-term stabilization of the Earth's surfaces temperature proposed by various authors. Enhanced land weathering rates of Fe-bearing silicates should be accompanied by the production of Fe^{3+}-oxides (e.g. hematite) as residuals of the weathering reactions, which then may be mobilized, transported, and deposited in adjacent sedimentary basins. The rock-magnetic properties of the Cicogna sediments generally indicate a relative increase in abundance of detrital hematite during times of enhanced warming (i.e. PETM and early Eocene warming trend), as revealed by a statistical correlation with the benthic oxygen isotopes record from the literature. These results confirm the existence of the silicate weathering machine as a buffer of climate warming on both short (10^5 kyr -PETM-) and long (10^6 kyr -EECO-) time scales. To find

a confirmation of this mechanism, I studied in detail the 8 m-thick Forada section across the PETM; the dataset from Forada, however, revealed that the sediments are pervasively contaminated by post-depositional chemical reduction processes that partially masked the primary, climate-controlled, rock-magnetic variability.

Riassunto

In questa tesi sono presentati e discussi i dati magnetostratigrafici e l'analisi delle proprietà magnetiche dei sedimenti di tre sezioni emipelagiche (Ardo, Cicogna e Forada) affioranti in Valbelluna (Alpi Meridionali Venete, Italia Nord-orientale). Il contributo di questa tesi alle attuali conoscenze riguardo al Paleogene inferiore è duplice e sarà discusso in due parti. La **Parte 1** riguarda le implicazioni dei dati collezionati sulla scala-tempo del Paleogene inferiore ed il suo miglioramento. La magneto-biocronologia del Paleogene inferiore, infatti, non è ancora ben definita, in particolare nell'intervallo di tempo compreso tra il Paleocene superiore e l'Eocene inferiore. Il motivo di questo va ricercato nel controverso e spesso ambiguo rapporto tra gli eventi paleomagnetici e paleontologici, dovuto alla presenza di lacune in molte sezioni oceaniche ed alla bassa risoluzione magnetostratigrafica durante il Chron C24r. Sarà quindi presentata una dettagliata magnetostratigrafia della sezione affiorante lungo il torrente Ardo (Paleocene inferiore) e della sezione affiorante lungo il torrente Cicogna (Paleocene superiore–Eocene inferiore). I sedimenti di entrambe le sezioni preservano un *record* ben definito delle inversioni del campo magnetico terrestre, più nel dettaglio dal Chron C29r al Chron C26r (Ardo) e dal Chron C25r al Chron C23r (Cicogna). I dati ricavati hanno permesso la costruzione di un preciso modello di età tramite correlazione con la scala delle inversioni

geomagnetiche di riferimento redatta da Cande e Kent (1995; CK95). La magnetostratigrafia della sezione del torrente Cicogna è stata inoltre integrata con una dettagliata biostratigrafia a nannofossili calcarei, la quale ha permesso di identificare molti nuovi eventi biostratigrafici molto utili a rifinire la cronologia di questo critico intervallo di tempo.

Nella **Parte 2** della tesi saranno discussi i risultati delle dettagliate analisi sulla mineralogia magnetica dei sedimenti che costituiscono le sezioni del torrente Cicogna e del torrente Forada; in particolare sarà illustrato come i dati provenienti dalle analisi dei sedimenti della sezione Cicogna hanno premesso una migliore comprensione dei meccanismi coinvolti nell'evoluzione climatica durante il Paleocene superiore–Eocene inferiore. Durante quest'intervallo di tempo il clima terrestre fu caratterizzato da un generale riscaldamento, il quale raggiunse il suo apice durante quello che è definito l'*early Eocene climatic optimum* (EECO, ~52–50 Ma); durante l'EECO il clima terrestre visse un periodo di caldo estremo, raggiungendo alte temperature anche alle alte latitudini. Il graduale *trend* di riscaldamento del Paleocene superiore–Eocene inferiore fu interrotto da alcuni eventi ipertermici (periodi geologici di breve durata caratterizzati da caldo estremo), il più intenso dei quali ebbe luogo al limite Paleocene–Eocene (~55 Ma) e prende il nome di *Paleocene–Eocene thermal maximum* (PETM); esso è distinto dalla presenza nel record sedimentario globale di un'escursione negativa (~2‰–4‰) degli isotopi stabili del carbonio e da una generale dissoluzione dei sedimenti carbonatici di mare profondo. Il clima caldo e umido del PETM ed in generale dell'Eocene inferiore fu verosimilmente caratterizzato da un rinvigorimento dei processi di alterazione delle rocce affioranti sui continenti; questo fenomeno avrebbe favorito il sequestro della CO_2 (gas

serra) in eccesso per tramite l'alterazione chimica dei minerali silicatici, seguito dalla deposizione dei carbonati negli oceani; questo sarebbe in accordo con il meccanismo di *feedback* negativo per la stabilizzazione a lungo termine delle temperature terrestri proposto da vari autori. Ad una più intensa alterazione dei minerali silicatici sui continenti, in particolare quelli contenenti Fe, dovrebbe corrispondere una maggiore formazione di ossidi ferrici (e.g. ematite) i quali andrebbero successivamente incontro a trasporto e sedimentazione nei bacini marini, processo favorito anche dall'incremento del ciclo idrogeologico caratterizzante i periodi di clima caldo. Le analisi delle proprietà magnetiche della sezione del torrente Cicogna indicano un incremento nell'abbondanza relativa dell'ematite detritica nei sedimenti durante i periodi di riscaldamento climatico (PETM e l'Eocene inferiore). Il legame temporale tra gli incrementi relativi in ematite e le paleotemperature è testimoniato da una correlazione chiara e statisticamente coerente con la curva delle variazioni globali degli isotopi stabili dell'ossigeno (*proxy* delle paleotemperature) ricavati da forme oceaniche bentoniche. I dati presentati confermano quindi l'esistenza del meccanismo di feedback negativo sulle variazioni delle temperature globali tramite l'alterazione dei minerali silicatici, sia su breve termine (10^5 kyr -PETM-) che su lungo termine (10^6 kyr -EECO-). Per cercare conferma di questo meccanismo in una sezione stratigrafica coeva sono stati descritti e campionati 8 m stratigrafici della sezione del torrente Forada a cavallo del limite Paleocene–Eocene. I dati ricavati dalle analisi rivelano tuttavia che i sedimenti della sezione Forada, benché mostrino un aumento generale dei parametri magnetici analogo a quello osservato durante il PETM nei sedimenti del torrente Cicogna, sono fortemente contaminati da fenomeni di riduzione chimica post-deposizionali, i quali hanno in gran parte alterato le proprietà magnetiche

della roccia e le loro variazioni stratigrafiche: i dati ricavati da questa sezione non sono quindi utilizzabili per interpretazioni di tipo paleoclimatico.

Chapter 1

Introduction

In this thesis I present magnetostratigraphic and rock-magnetic data from three selected Paleocene–early Eocene sections from the Belluno Basin (Venetian Southern Alps, NE Italy), namely the Ardo, Cicogna, and the Forada sections (Fig. 1.1).

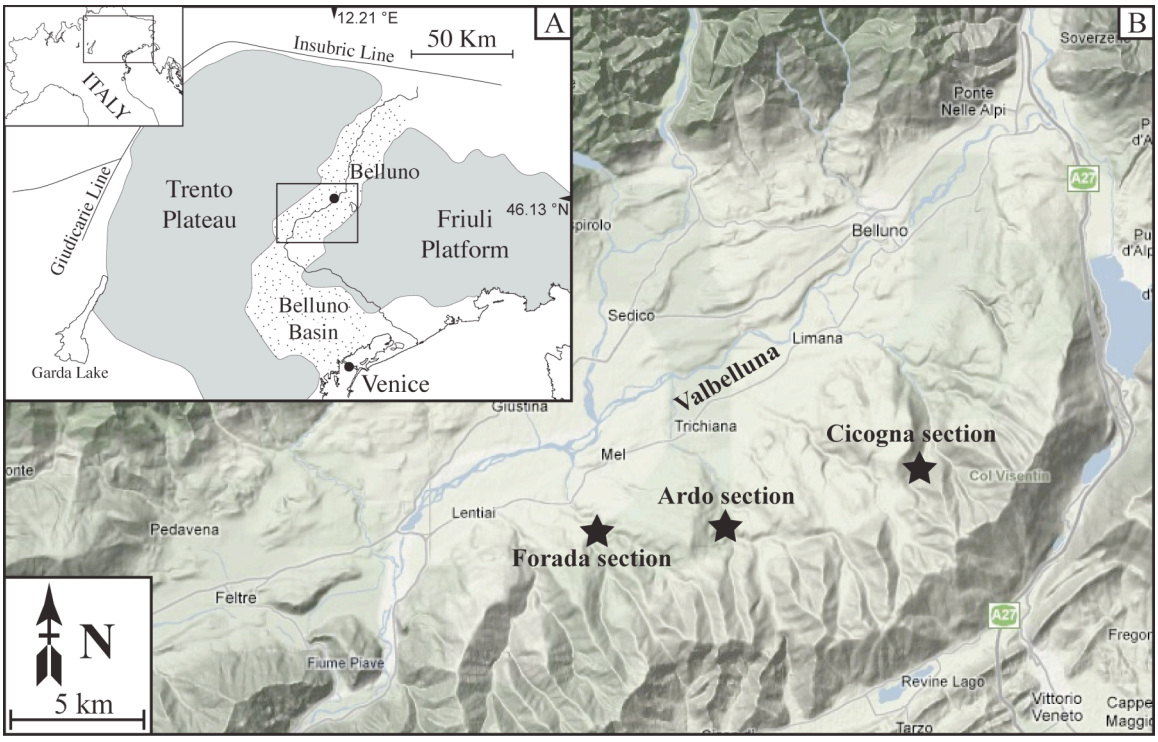

Figure 1.1. A) Geologic sketch map of the Venetian Southern Alps with indication of key paleogeographic domains; the geographic position and the coordinates of the city of Belluno are indicated. B) Physical map of the Valbelluna area; the black stars indicate the position of the sections studied in this thesis.

The Belluno Basin is a paleogeographic domain developed since the Early Jurassic, bounded to the West by the Trento Plateau and to the East by the Friuli Platform (Winterer and Bosellini, 1981; Castellarin and Cantelli, 2000; Zattin et al., 2006) (Fig. 1.1A). Cretaceous to lower Eocene sediments of the Belluno Basin crop out over a wide area in the Valbelluna. They consist of pelagic to hemipelagic successions up to 200–250

m in thickness, and are mainly represented by well-bedded, pink to red limestones and marly limestones, here referred to as Scaglia Rossa *sensu lato* (*s.l.*), which includes lithostratigraphic units that still need formal ratification (e.g., Cugnan Formation, Scaglia Cinerea, Marna della Vena d'Oro; Di Napoli Alliata et al., 1970; Costa et al., 1996). For additional information on the stratigraphy of the studied area, see the paper by Agnini, Dallanave, et al. (2008) published (in Italian) on the *Rendiconti online Soc. Geol. It.* and included as Appendix 1 of this thesis.

The contribution of this thesis to the present-day knowledge of the early Paleogene time is twofold and is discussed in two parts:

Part 1. **Improving the current early Paleogene time scale (Berggren et al., 1995).**

Part 2. **Understanding the long-term late Paleocene–early Eocene climate evolution.**

Part 1. **Improving the current early Paleogene time scale.** As discussed in **Chapter 2** of this thesis, the Berggren et al. (1995) reference timescale (BKSA95) is based on a limited number of Paleogene sections provided with reliable, although in the last decade the global magneto-biostratigraphic dataset for this time interval has been improved with data collected from both outcropping sections and deep-sea cores (Berggren et al., 2000; Bowles, 2006; Agnini et al., 2006, 2007; Dinarès-Turrel et al., 2007). One of the most problematic time intervals of the Paleogene is represented by Chron C24r (~55.9–53.35 Ma), where the Paleocene-Eocene boundary (~55 Ma) is placed. In this thesis will be presented the magnetostratigraphy of the early Paleocene part of the Ardo section **(Chapter 3)** and the upper Paleocene–lower Eocene Cicogna section **(Chapter 4)**. The magnetostratigraphy of the Cicogna section is also integrated with a detailed calcareous nannofossils biostratigraphy, and thus offers the possibility to assess in detail the

magneto-biochronology of the critical time interval around the Paleocene–Eocene boundary for comparison with, and improvement of, the BKSA95 reference time scale.

Part 2. **Understanding the long-term late Paleocene–early Eocene climate evolution.** During the early Paleogene the Earth's climate underwent through a complex evolution. In particular, from the mid-Paleocene (~59 Ma) to early Eocene (~52 Ma), global climate experienced a pronounced warming trend, which eventually culminated with the early Eocene climatic optimum (EECO; ~52–50 Ma), characterized by warm climate conditions even at extremely high latitudes (McKenna, 1980; Moran et al., 2006). This long-term evolution is punctuated by several short-lived hyperthermal events, the most prominent of which is the Paleocene–Eocene thermal maximum (PETM).

In this thesis, an introduction on the long-term carbon cycle and its implication on the Earth's climate are presented in **Chapter 5**. Detailed analyses on the rock-magnetic properties of the upper Paleocene–lower Eocene sediments of the Cicogna section are then discussed in **Chapter 6**; these rock-magnetic data confirm the existence in the Paleocene–Eocene of the silicate weathering negative feedback mechanism for the long-term stabilization of the Earth's surfaces temperature first proposed by Walker et al. (1981). In **Chapter 7** a detailed rock-magnetic survey using samples collected across the PETM in the Forada section is discussed; we anticipate that the magnetic minerals therein contained have been contaminated by chemical reduction processes of post-depositional (i.e. secondary) origin. A summary of the results and the main conclusions of this thesis are presented in **Chapter 8**.

Part 1

Improving the current early Paleogene time scale

Chapter 2

Paleogene time scale: state of the art

Berggren et al. (1995) presented a revised magneto-biochronologic time scale for the Cenozoic, hereafter referred to as BKSA95, by integrating several sources of data. The biostratigraphic events were correlated to the geomagnetic polarity time scale (GPTS) of Cande and Kent (1995), hereafter referred to as CK95. The construction of the CK95 GPTS was based primarily on the South Atlantic magnetic anomalies integrated with fine-scale data from magnetic profiles on faster spreading ridges in the Pacific and Indian Ocean. A cubic spline function fitted to 9 age calibration-anomaly distance tie-points (plus the zero-axis ridge axis) was used to generate the time scale of the reversal sequence (fig 2.1, fig. 2.2).

The Paleogene part of the BKSA95 (fig. 2.1, 2.2) is based on a small number of Paleogene sections with reliable magnetostratigraphy, either due to poor recovery (e.g., Hole 762C) or to the presence of unconformities (e.g., Holes 577, 577A). There are hence intervals where biostratigraphic events are still poorly tied to magnetochronology, like for example in the Paleocene–early Eocene, which is the main time interval studied in this thesis. Nonetheless, in the last decade the Paleogene magneto- and bio-stratigraphic dataset has been improved with data collected from both deep-sea cores (ODP Site 1262; Bowles 2006, Agnini et al., 2007) and outcropping sediments (e.g., Agnini et al., 2006; Dinarès-Turell et al., 2007). Among the deep-sea sites, DSDP Site 384 appears to offer the greatest completeness between Chron C25n and C29n (Berggren et al., 1995, 2000), while the more recent ODP Site 1262 (Walvis Ridge, southern Atlantic Ocean) (Fig. 2.3) shows an apparently continuous record from Chron C23n to C30n.

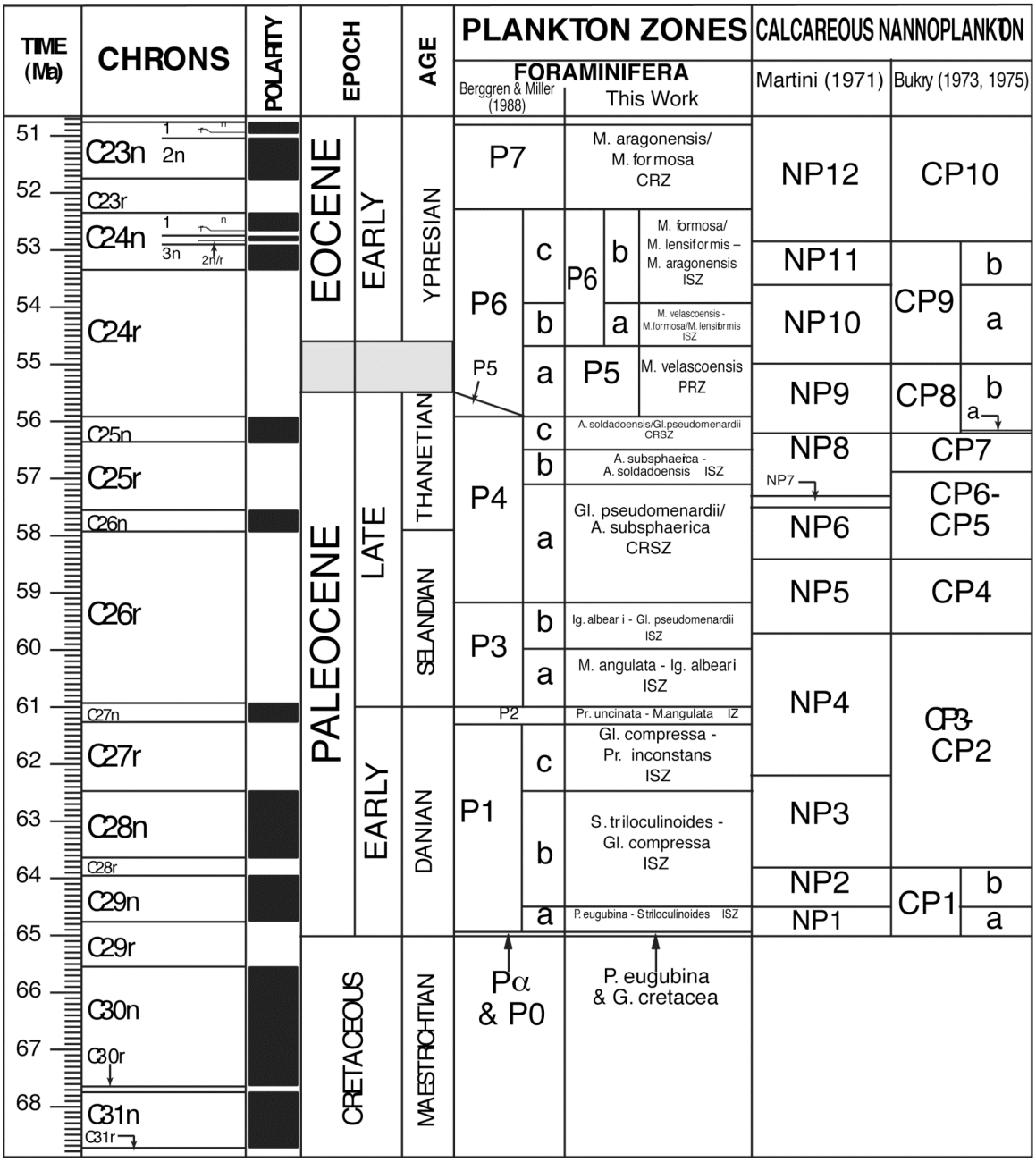

Figure 2.1. The chronology of the Cenozoic Era and its chronostratigraphic subdivision (Berggren et al., 1995); late Cretaceous to early Eocene time scale.

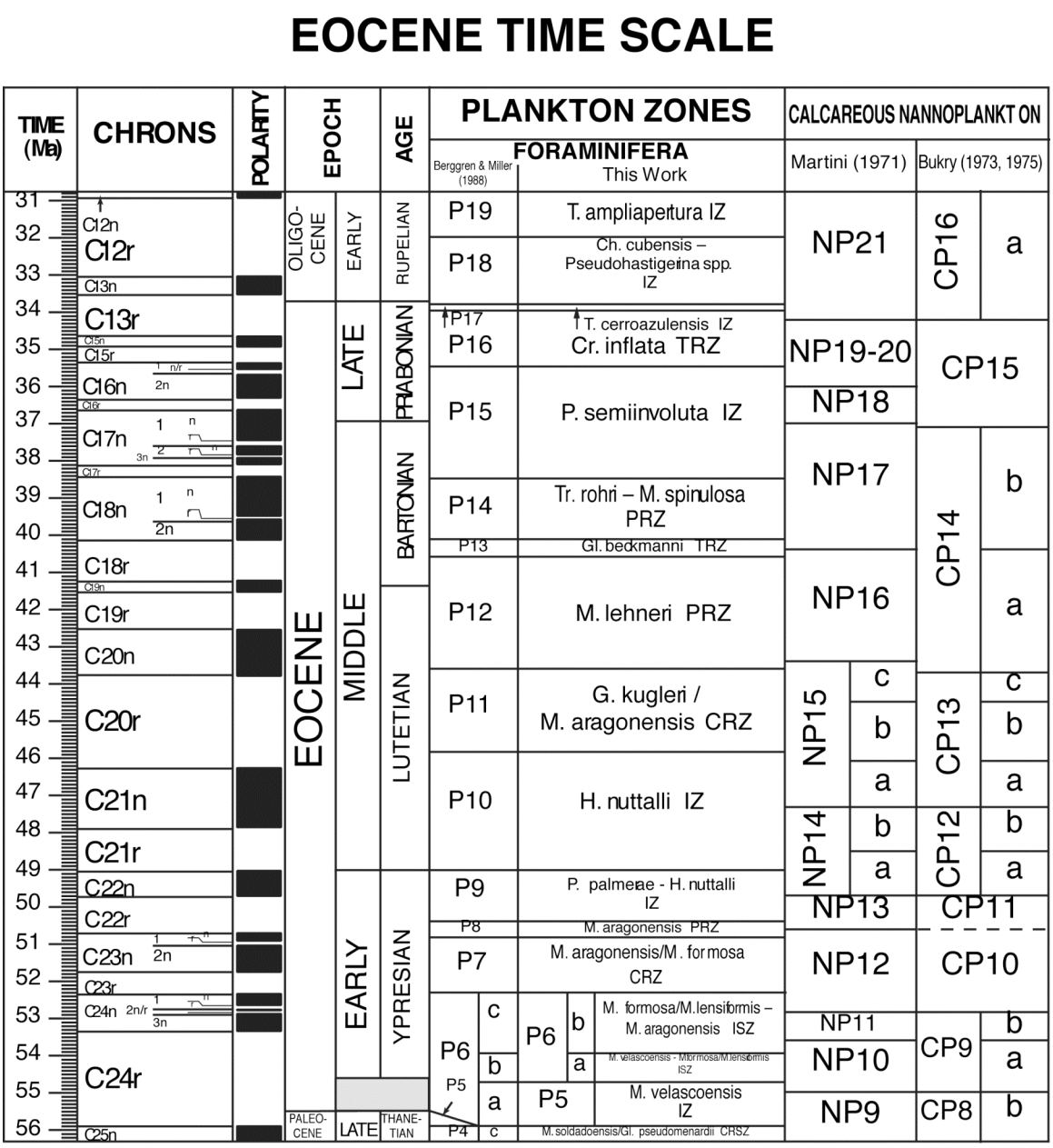

Figure 2.2. The chronology of the Cenozoic Era and its chronostratigraphic subdivision (Berggren et al., 1995); late Paleocene to early Oligocene time scale.

Despite these drilling efforts at sea, land sections frequently offer the possibility to retrieve more continuous and detailed data. The classic sections near Gubbio provided the first detailed magnetostratigraphic control of bioevents over the Late Cretaceous–Eocene

time interval (Lowrie et al., 1982; Napoleone et al., 1983; Monechi and Thierstein, 1985; Fig. 2.3). After these pioneering studies at Gubbio, several recent attempts to improve the magnetobiochronology across the Late Paleocene–Early Eocene time interval involved the study of sections in Spain and Italy.

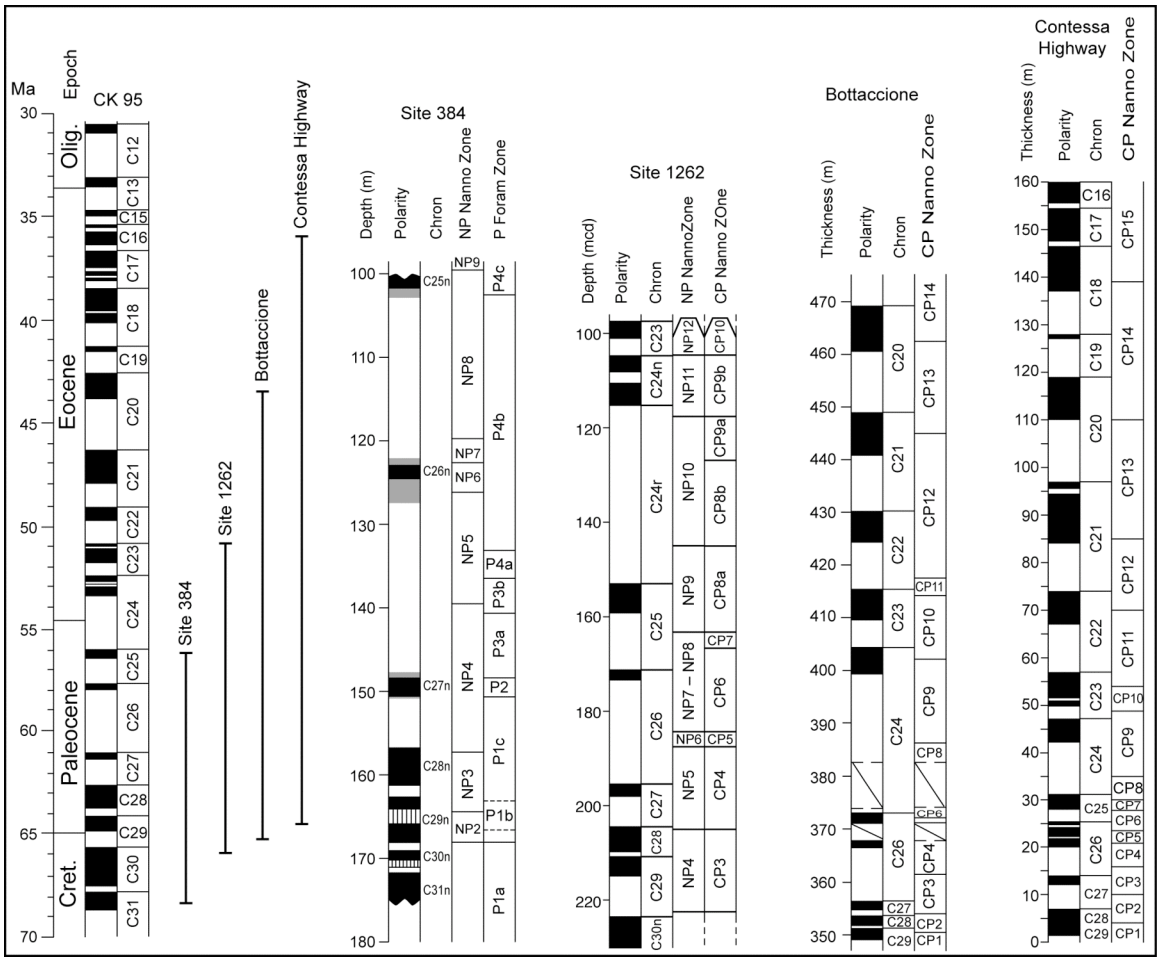

Figure 2.3. The magneto-biostratigraphy of the DSDP site 384, ODP Site 1262, and of the classic sections near Gubbio (Bottaccione and Contessa Highway sections), correlated with the CK95 time scale; see text for details.

The Zumaia section (Basque Basin, Northern Spain) provided an integrated magneto-bio- cyclostratigraphic framework for the Paleocene; it spans from Chron C29r to Chron

C24r and form calcareous nannoplankton Zone NP1 to Zone NP10 (Martini, 1971) (see Dinarès-Turell et al., 2002, 2003, 2007; Fig. 2.4). In Italy, Agnini et al. (2006) studied the Possagno section (Venetian Southern Alps, NE Italy), which spans from Chron C24r to Chron C20 and from calcareous nannoplankton Zone NP9a to Zone NP15b (=CP8a–CP13b following Okada and Bukry, 1980) (Fig. 2.4).

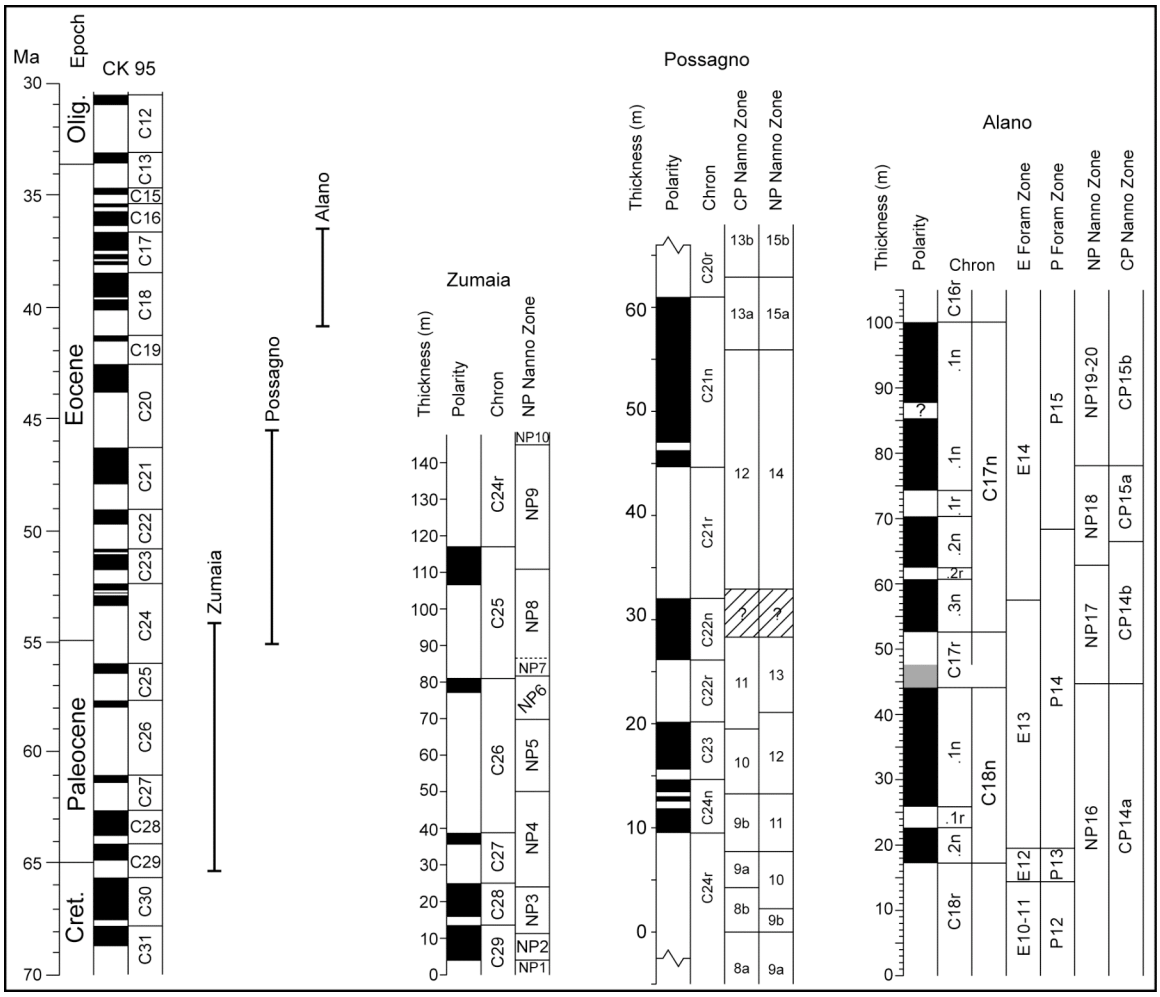

Figure 2.4. The magneto-biostratigraphy of the Zumaia, Possagno, and Alano sections, correlated with the CK95 time scale; see text for details.

Finally, a very recently studied section with good magneto-biostratigraphy is the Alano section (Venetian Southern Alps, NE Italy), which encompass Chrons C18r to C16r, calcareous nannoplankton Zones from NP16 to NP19–20 (=CP14a–CP15b), and planktonic foraminifera Zones from E10–11 to E14 (Berggren and Pearson, 2005) (which corresponds to Zones from P12 to P15 following Berggren et al., 1995).

From these studies it becomes apparent that one of the most problematic time intervals of the Cenozoic is Chron C24r (~55.9–53.35 Ma), where the Paleocene–Eocene boundary (~55 Ma) is placed. This is essentially because of the controversial and ambiguous relationships between paleontologic and magnetic events due to the presence of unconformities in several deep-sea and shallow water sections from the literature around the Paleocene–Eocene boundary (e.g. DSDP Sites 549 and 550) (Aubry et al., 1996), and the lack of (magnetic) resolution in the long Chron C24r interval (Berggren et al., 1995 and references therein).

In the next two chapters, the magnetostratigraphic dataset of the early Paleocene Ardo section and the late Paleocene–early Eocene Cicogna sections are presented (Fig. 2.5). In particular, the Cicogna section dataset is associated with a detailed calcareous nannoplankton biostratigraphy encompassing the Paleocene–Eocene boundary within critical Chron C24r. These data are thus aimed at refining the state of the art of the Paleogene time scale.

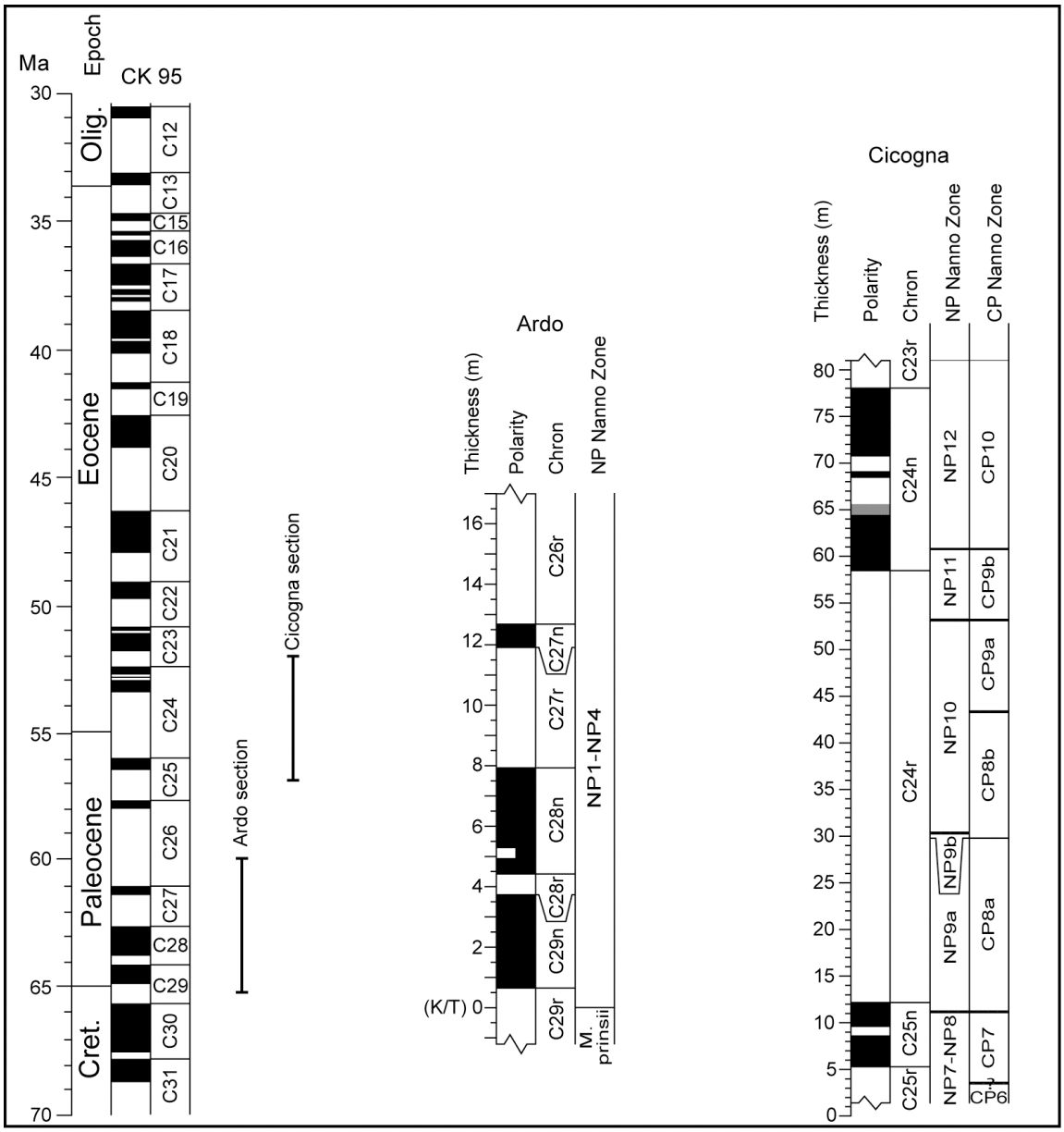

Figure 2.5. Magneto- biostratigraphy of the Ardo and the Cicogna sections, correlated with the CK95 GPTS; the biostratigraphy of the Ardo section is from Giusberti et al. (2007), and it is currently under refinement.

Chapter 3

The Ardo section

3.1 Introduction

The Ardo section (46.04°N, 12.15°E) is located ~1.5 km east of the S. Antonio Tortal village. The entire section is ~170 m thick and is here referred to as Scaglia Rossa (*s.l.*), although in the literature local names are used to describe the different lithologies constituting the section (*i.e.*, Cugnan Formation, Scaglia Cinerea, Marna della Vena d'Oro). The section crops out along the Ardo riverbed and spans from the upper Cretaceous to the lower Eocene (Costa et al., 1996); the general dip direction is ~345°N, and the dip is ~15°. The Cretaceous–Paleocene transition is represented by a ~1.5 mm-thick clay level, gray-greenish at the base and red above. From the clay level to ~15 m the section is constituted by well-stratified red marly limestones often interrupted by ~5–50 cm-thick white calcareous turbidite layers. At ~15 m the sediments become progressively gray in color, and are organized in ~0.2–0.3 m-thick marly limestones-marls couplets; from ~ 20 m to the section top the section consists of mainly gray marly limestones with rare turbidite layers ~1–5 cm-thick. For the purpose of this thesis, I have sampled the basal ~16 m of the section, which are represented in detail in Fig. 3.1. The sampled section spans calcareous nannoplankton zones from *Micula prinsii* of Perch-Nielsen (1979) to NP1–NP4 of Martini (1971) (Giusberti et al., 2007), thus encompassing the late Maastrichtian–Danian interval.

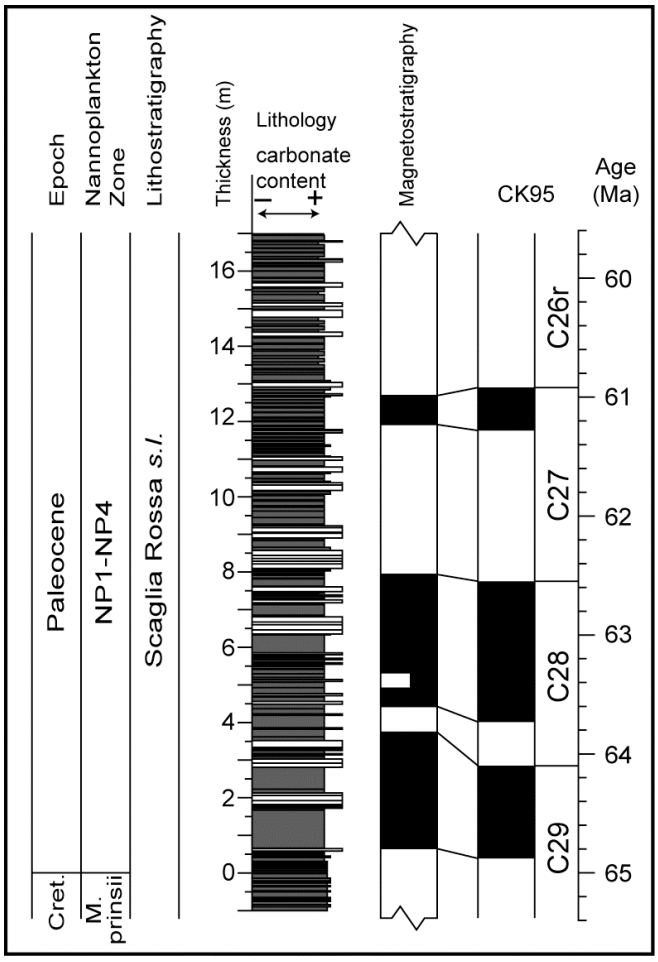

Figure 3.1. The late Cretaceous-early Paleocene Ardo section; on the left is represented the calcareous nannoplankton zonation from Giusberti et al. (2007); the magnetostratigraphic zonation from the Ardo section is correlated to the CK95 reference time scale (Cande and Kent, 1995).

3.2 Paleomagnetism

Paleomagnetic samples were drilled and then oriented with a magnetic compass in the field along ~16 m of section. The average sampling interval was ~0.24 m, for a total of 66 standard ~11 cc specimens for analyses, conducted at the Alpine Laboratory of Paleomagnetism (Cuneo, Italy). After the initial measure of the natural remanent magnetization (NRM), all the specimens were thermally demagnetized in maximum steps of 50 °C, and the component structure of the NRM was monitored after each demagnetization step by means of vector end-point demagnetization diagrams

(Zijderveld, 1967); steps of 10–25 °C were adopted close to critical unblocking temperatures.

The NRM intensity of the specimens ranges between ~0.02–21.1 mA/m, with a mean value of 8.86 mA/m. Low values are generally observed at the basal meter of the section, below the K/T boundary, and at the uppermost meter of the section, when the sediments gradually turn to gray in color; shifts toward lower values are generally observed also in correspondence of calciturbidite layers (e.g., at ~ 1.85, 2.87, and 3.45 m levels) (Fig. 3.2).

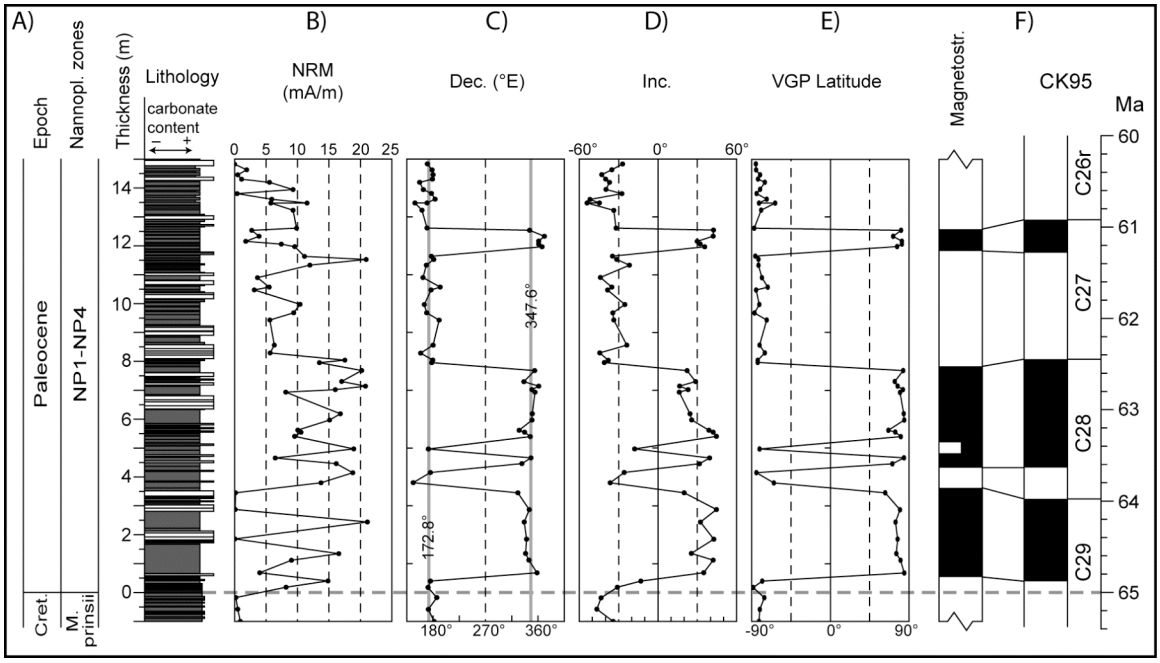

Figure 3.2. Magnetic stratigraphy of the Ardo section. A) Lithological log of the section placed aside the calcareous nannoplankton biostratigraphy of Giusberti et al. (2007); B) values of the natural remanent magnetization (NRM) across the section; C-D) declination and inclination of the magnetic characteristic components of each sample in tilt-corrected coordinates; E) virtual geomagnetic pole latitudes relative to the North pole axis; F) correlation of the obtained sequence of magnetic reversals with the CK95 reference time scale.

Down-pointing northward directions (in "*in situ*" coordinates) have been commonly isolated between room temperature and ~200–300 °C ("A" component; Fig. 3.3).

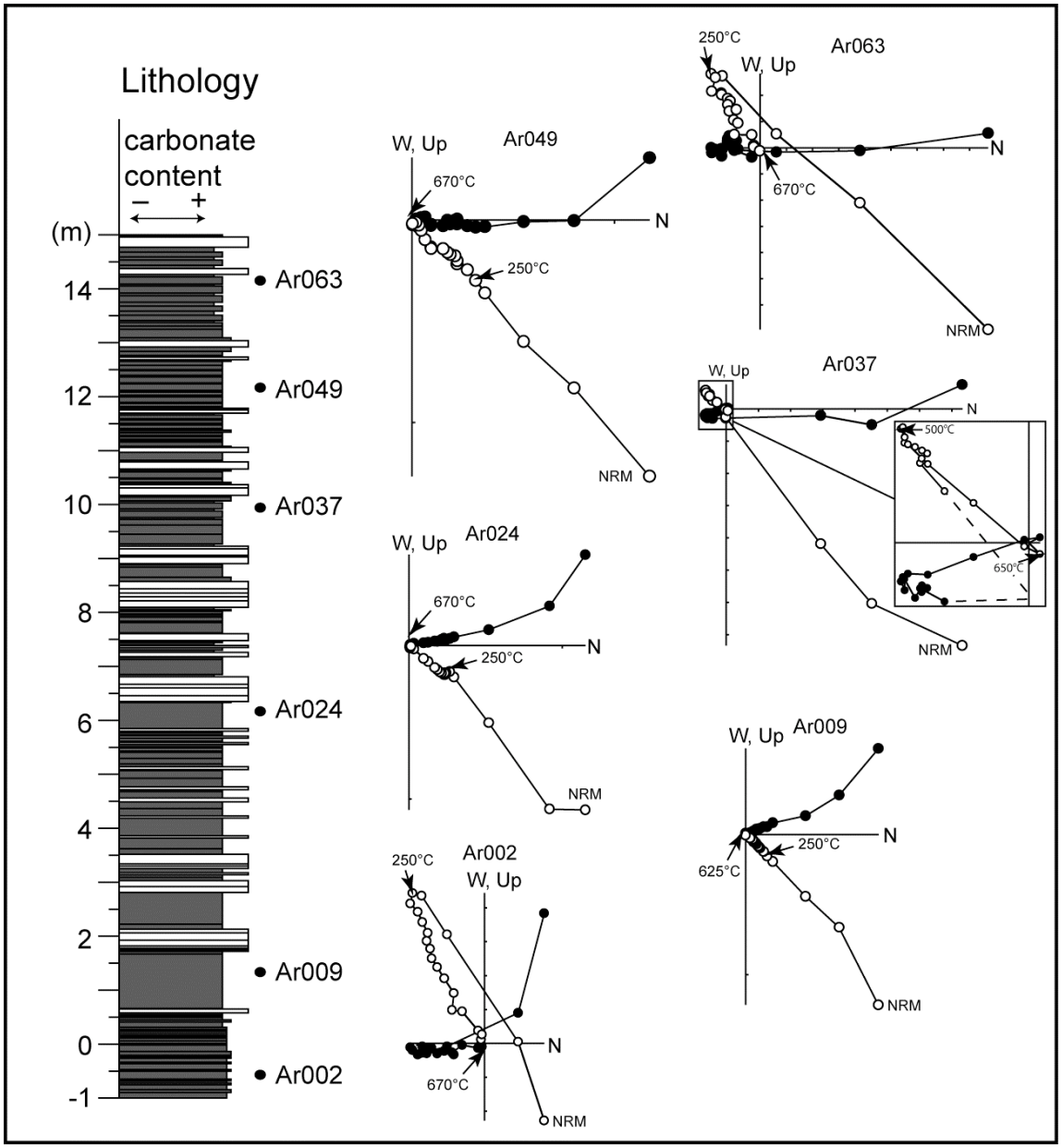

Figure 3.3. Vector end-point demagnetization diagrams of NRM of representative samples from the Ardo section in "*in situ*" coordinates; filled (open) circles represent projection onto the horizontal (vertical) plane; the position of each sample is indicated on the lithological log.

The distribution of the "A" component, which declination and inclination mean values, and the associated Fisher precision parameters (a95 and k) are shown in Fig. 3.4, is slightly shallower after correction for the homoclinal bedding tilt. Its average position in "in situ" coordinates depart from the present-day geomagnetic field direction, calculated using the geocentric axial dipole model (GAD; e.g. Butler, 1998), by 15.3° (Fig. 3.4).

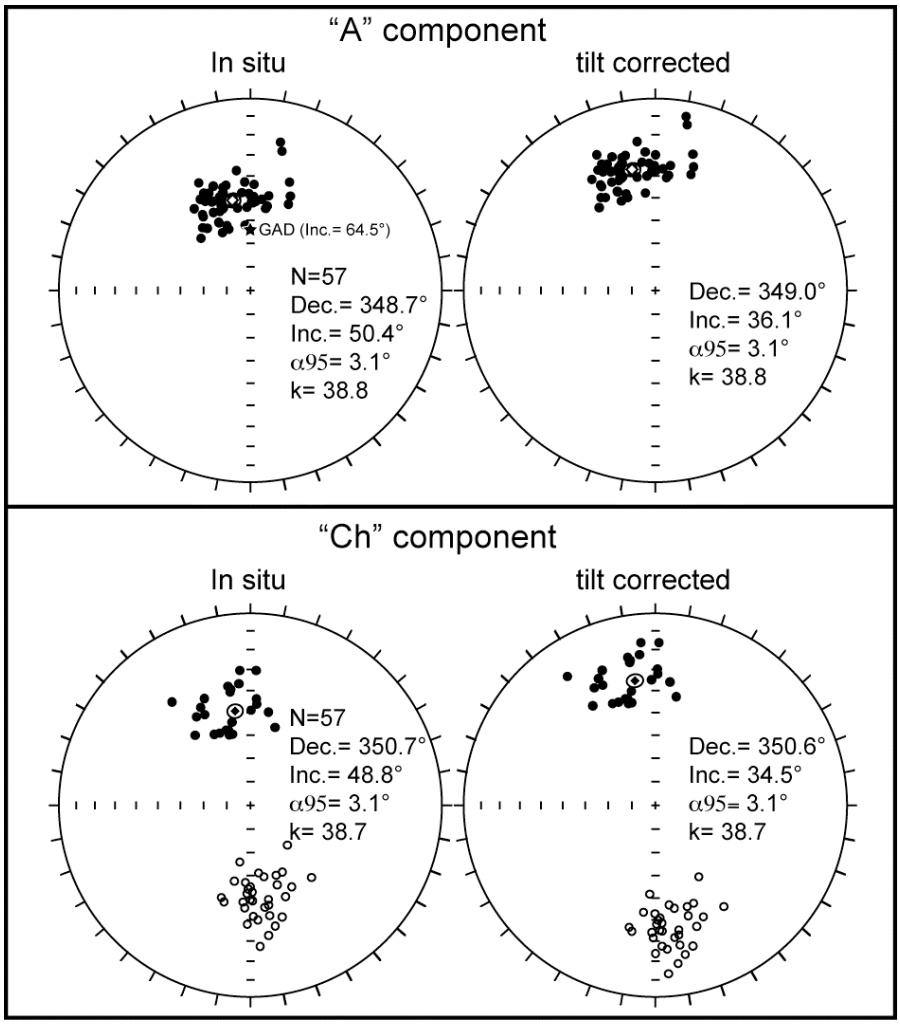

Figure 3.4. Equal area projections before (*in situ*) and after bedding tilt correction of the "A" and the characteristic ("Ch") component directions of the NRM; the open and filled diamonds represent the mean direction of the "A" and the "Ch" components, respectively, with the associated Fisher precision parameters α_{95} and k calculated (N= number of directions).

Removal of these spurious magnetizations revealed the presence of a characteristic component linearly trending to the origin of the demagnetization axes. This characteristic ("Ch") component was isolated in 57 (86.4%) specimens by linear interpolation of the vectors end-points between ~250 and ~625 °C (Fig. 3.3). The distribution of the "Ch" components, and its statistical parameters are shown in Fig. 3.4. The characteristic magnetizations are antipodal and oriented NNW-and-down or SSE-and-up in geographic (*in situ*) coordinates, whereas after correction for the homoclinal bedding tilt, they become somewhat shallower (Fig. 3.4).

The "Ch" directions depart from antipodality by 5.0° and pass the reversal test at the 95% level of confidence using the procedure suggested by Watson (1983) (V_w= 3.9; $V_{critical}$= 6.1; see also Tauxe, 2010), corresponding to reversal test class "A" of McFadden and McElhinny (1990). Inverting all directions to a common NNWward polarity we obtained a tilt corrected mean direction of Dec.= 350.6°, Inc.= 34.5° (N= 57, k= 38.7, α95= 3.1°).

We calculated the position of the virtual geomagnetic pole (VGP) for the characteristic direction of each sample from the Ardo section; we then determined the mean paleomagnetic pole (Ar1; Long. = 211.0°E, Lat. = 61.5°E, A95=2.9°; Fig. 3.5A) by averaging the VGPs positions. We compared the Ar1 paleopole to the late Cretaceous–early Miocene master apparent polar wander path (APWP) for Africa of Besse and Courtillot (2003) (hereafter referred to as BC03) to constrain the age of the characteristic magnetization and assign polarity to the NNW-and-down or SSE-and-up characteristic directions. During the Cenozoic Alpine deformation, relative less deformed part of the Southalpine belt (e.g., Dolomites) maintained substantial tectonic coherence with Africa

(within paleomagnetic resolution), and the paleogeographic affinity of the Southern Alps with Africa has been demonstrated at least since the Permian (Muttoni et al., 2001). The Ar1 paleopole is however removed from the early Paleocene APWP of Africa by 13.3° in the far side direction compared to the sampling site (Fig. 3.5A).

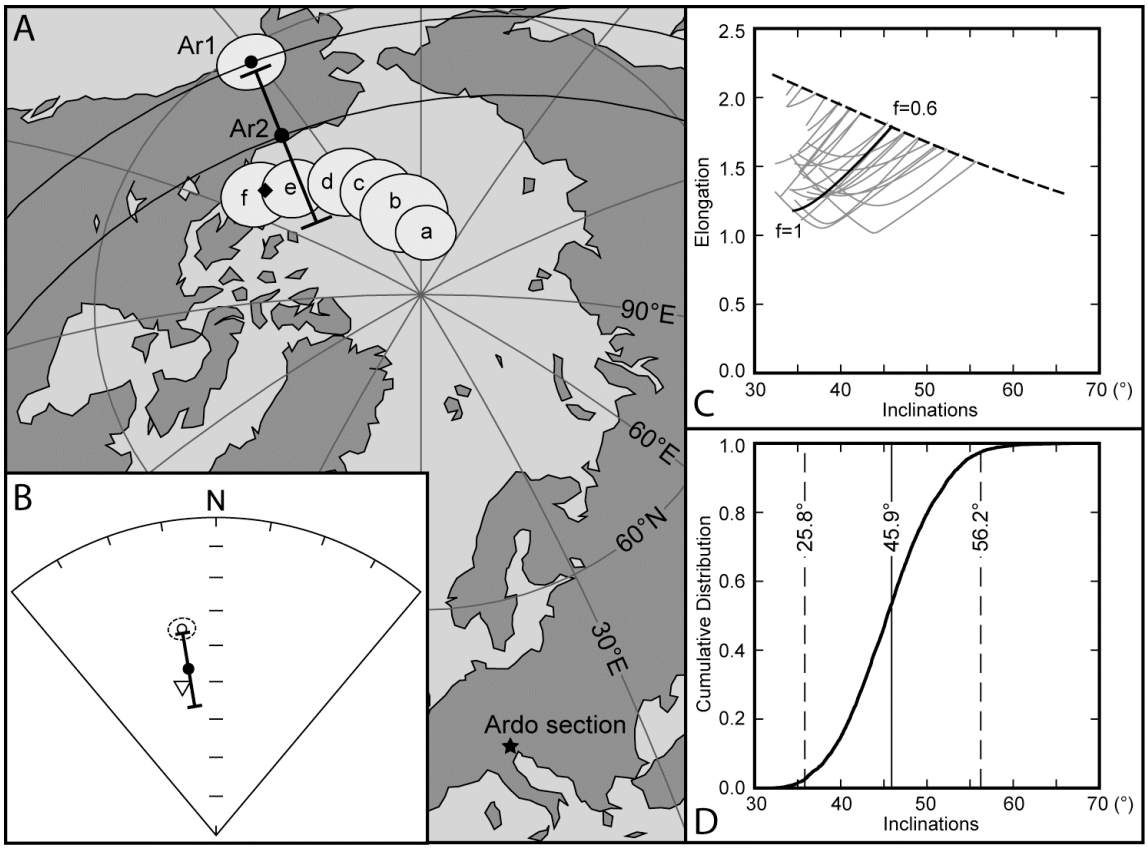

Figure 3.5. A) The mean paleomagnetic pole from the Ardo section before (Ar1) and after (Ar2) directional unflattening is compared with the apparent polar wander path (APWP) of Africa of Besse and Courtillot (2003; BC03) for the 20–70 Ma (a–f circles) time interval; the closed diamond represents the position of the reference pole for 62.5 Ma, estimated using the BC03 African APWP (map drawn with Paleomac by Cognè, 2003). B) The characteristic mean direction from the Ardo section before (open circle) and after (closed circle) directional unflattening, with the associated 95% confidence boundaries (dashed circle and error bar, respectively); these mean directions are compared to the mean direction expected at Ardo from the 62.5 Ma paleopole for Africa calculated from the Besse and Courtillot (2003) APWP curve. C) The E/I

values of the systematically unflattened directions with the unflattening parameter f ranging from 1 to 0.6 (heavy line) are compared to the E/I values predicted by the TK03.GAD geomagnetic field model (dashed line). 25 of 5000 boostrapped data set are shown by the light lines. D) Diagram of the cumulative distribution of all inclinations derived from the bootstrapped crossing points, with the associated 95% confidence boundaries (25.8°–56.2°) around the mean value (45.9°).

This deviation is the consequence of an inclination shallowing of the characteristic mean direction by 11.4° with respect to the expected direction at Ardo (estimated from the BC03 African APWP) (Fig. 3.5B). The unblocking temperature of the characteristic components suggests that the magnetization is carried by hematite; rock-magnetic experiments are at present in progress to confirm this inference. Acknowledging that shallow bias magnetic directions are often associated with detrital hematite (Tauxe and Kent, 1984), I attempted to correct for the inclination shallowing using the elongation/inclination (E/I) statistical method of Tauxe and Kent (2004; see also Kent and Tauxe, 2005; Tauxe et al., 2008). Following this method, the directions dataset is progressively "unflattened" applying gradually decreasing values of the "*f*" parameter first introduced by King (1955) by the formula:

$$\tan I_f = f \cdot \tan I_0$$

where I_f and I_0 are respectively the measured inclination and the true inclination of the magnetic field during the sedimentation; the "*f*" parameter can range from f=1 ($I_f = I_0$) to f=0 (completely flattened directions). The proper value of "*f*" is reached when the directional dataset assumes an E/I pair of values consistent with the paleosecular

variation TK03.GAD model (Tauxe and Kent, 2004; Tauxe et al., 2008). To evaluate the uncertainty of this estimate, I repeated the analyses by generating 5000 bootstrapped dataset. The results of these analyses are illustrated in Fig. 3.5 (C, D). A significant problem associated with the application of the E/I method to the Ardo dataset is the limited number of directions (N=57); as pointed out by Tauxe et al. (2008), a number of directions < ~100–150 limits the ability to apply the E/I method with an acceptable level of reliability. This uncertainty led to a 20.4°-wide confidence angle. Nonetheless, the new Ardo paleopole (Ar2) position, recalculated after the inclination shallowing correction, is moved by 8.3° toward the early Paleocene APWP, and falls only 5.6° away from the reference African pole for 62.5 Ma of Besse and Courtillot (2003).

3.3 Magnetostratigraphy and age model

We interpreted the polarity stratigraphy by means of interpretation of the VGPs position relative to the (north) pole axis (Lowrie and Alvarez, 1977; Kent et al., 1995). VGP relative latitudes approaching 90°N or 90°S are interpreted respectively as recording normal or reverse polarity. The VGP data revealed a main sequence of 6 magnetic reversals (Fig. 3.2). In particular, a ~1.5 m thick reverse polarity interval is observed at the section base; it is followed by two normal polarity intervals, respectively ~3.1 and ~3.5 m-thick, that straddle a ~0.7 m-thick reverse polarity interval. From 7.8 m up to the section top, the observed polarity is mainly reverse, aside for a ~ 0.8 m-thick normal polarity event recorded at the ~12 m level.

I compared the Ardo magnetostratigraphy with coeval data from the ODP Site 1262 (Walvis Ridge, Atlantic Ocean), as well as with data from outcropping sections

from the literature, namely the Zumaia section (Basque basin, Spain; Dinarès-Turrel et al., 2003), and the Contessa highway and Bottaccione sections near Gubbio (Northern Appenines, Italy; Lowrie and Alvarez, 1977; Lowrie et al., 1982; Napoleone et al., 1983) (Fig. 3.6).

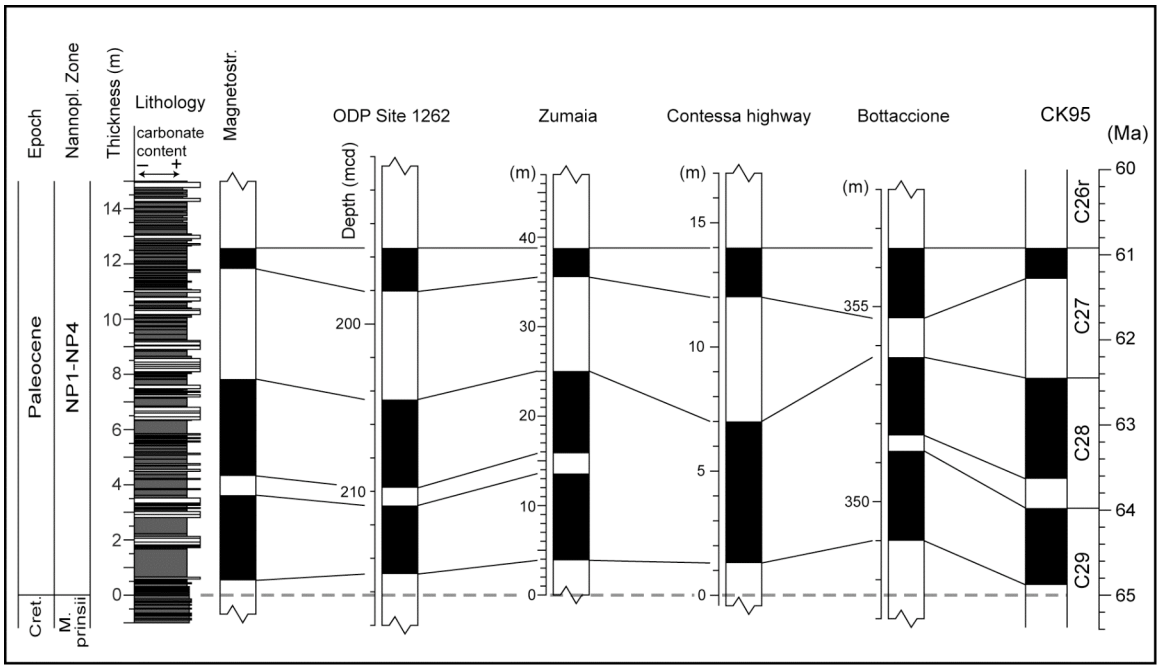

Figure 3.6. The magnetostratigraphy of the Ardo section is compared with the coeval magnetostratigraphy from ODP Site 1262, Zumaia (Basque Basin, Spain), Contessa highway and Bottaccione (Central Appennines, Italy); all the sections are compared with the CK95 reference time scale (Cande and Kent, 1995).

I observe an excellent magnetostratigraphic matching between the correlated sections and the CK95 reference geomagnetic polarity time scale (GPTS) (Cande and Kent, 1995). Based on these considerations, I conclude that the sampled part of the Ardo section encompasses an overall sequence of 7 magnetozones from Chron C29r to Chron C26r (~65 to 60 Ma).

I constructed an age-depth plot for the Ardo section by means of correlation with the CK95 GPTS. Specifically, the tie points used to construct the age model are (1) Chron 29r(0.0) (64.75 Ma), (2) Chron 29n(0.0) (63.98 Ma), (3) Chron C28r(0.0) (63.63 Ma), (4) Chron C28n(0.0) (62.5 Ma), (5) Chron C27r(0.0) (61.28 Ma), and (6) Chron C27n(0.0) (60.92 Ma) (see Cande and Kent, 1992 for the nomenclature). In addition, I used as a (7) chronological tie point also the Cretaceous/Paleogene boundary (K/T) placed at 65 Ma (Fig. 3.7).

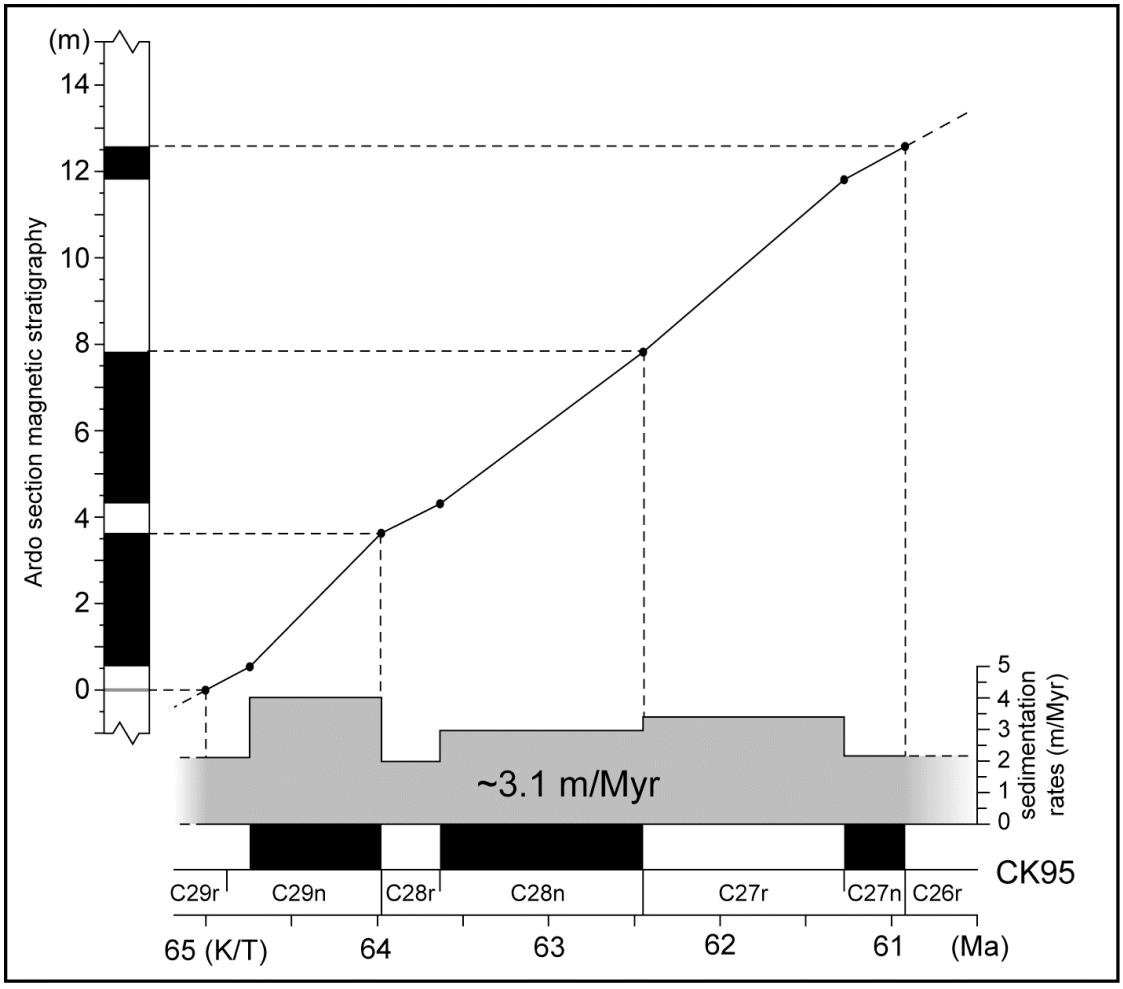

Figure 3.7. Age-depth model and derived sediment accumulation rates for the Ardo section obtained by magnetostratigraphic correlation with the CK95 reference timescale (Cande and Kent, 1995).

Sediment accumulation rates, calculated assuming linear interpolation between magnetic reversals, as well as between the K/T and the C29r/C29n boundary, are relatively constant on the order of ~3.1 m/Myr throughout the ~5 Myr encompassed by the section (Fig. 3.7).

3.4 Conclusions

The analyses conducted at the Ardo section provided a well-defined magnetostratigraphic sequence. A total of 6 geomagnetic reversals, plus the presence of the K/T boundary, allowed the construction of a detailed age model, with a robust age control across the entire section. The section encompass Chrons C29r to C26r; the sedimentation rates range from ~2.1 to ~4.0 m/Myr, with a mean value of ~3.1 m/Myr. In this chronologically calibrated framework, it will be possible to place the results of a detailed calcareous nannoplankton biostratigraphic study, currently in progress by Dott. C. Agnini (University of Padova), with the aim to improve the status of the current time scale for the early Paleocene.

Finally, more samples are necessary to better quantify the deviation of the mean characteristic direction from the expected field direction due to inclination shallowing; this is confirmed by the ~20°-wide confidence angle of the unflattened mean direction. Increasing the number of directions from a present value of 57 to the ~100–150 samples required by the E/I method would lead to a robust quantification of the shallow bias in the Scaglia Rossa at the Ardo section.

Chapter 4

This chapter consists the paper "*Magneto-biostratigraphy of the Cicogna section (Italy): Implication for the late Paleocene–early Eocene time scale*", published by Dallanave E., Agnini C., Muttoni G., and Rio D. on *Earth and Planetary Science Letters 285 (2009), 39–51*.

Data relative to the paper are presented in Appendix 4 (pag. 43): Table A1 = List of the late Paleocene–early Eocene biostratigraphic and magnetostratigraphic events from the Cicogna section; Table A2 = List of the paleomagnetic characteristic components derived from least-square analysis on the Cicogna samples; Table A3 = List of magnetic susceptibility and IRM values of the Cicogna samples.

Table A2 can be used to reconstruct Fig. 4F and Fig. 5B of the Dallanave et al. (2009) paper, whereas Table A3 can be used to reconstruct Fig. 4A, B, C and Fig. 8 of the same paper.

Earth and Planetary Science Letters 285 (2009) 39–51

Contents lists available at ScienceDirect

Earth and Planetary Science Letters

journal homepage: www.elsevier.com/locate/epsl

Magneto-biostratigraphy of the Cicogna section (Italy): Implications for the late Paleocene–early Eocene time scale

Edoardo Dallanave [a,b,*], Claudia Agnini [a], Giovanni Muttoni [b,c], Domenico Rio [a]

[a] Department of Geosciences, University of Padova, Via Giotto 1, I-35137 Padova, Italy
[b] ALP – Alpine Laboratory of Paleomagnetism, Via Madonna dei Boschi 76, I-12016 Peveragno (CN), Italy
[c] Department of Earth Sciences, University of Milan, Via Mangiagalli, 34 I-20133 Milano, Italy

ARTICLE INFO

Article history:
Received 26 January 2009
Received in revised form 21 April 2009
Accepted 22 May 2009
Available online 24 June 2009

Editor: P. DeMenocal

Keywords:
paleocene
eocene
magnetostratigraphy
biostratigraphy
magnetic properties
chronology

ABSTRACT

We present the magnetostratigraphy and calcareous nannofossil biostratigraphy of the ~81 m thick upper Paleocene–lower Eocene Cicogna section from the Belluno Basin of NE Italy. The Cicogna section extends in stratigraphic continuity from Chron C25r to Chron C23r and from nannofossil Zone NP7/NP8 to NP12 (=CP6–CP10), thus covering an interval of time comprised between ~56.6 and ~52.2 Ma. Inferred sediment accumulation rates were relatively constant in the order of ~18 m/Myr, and were used to estimate the age of standard calcareous nannofossil events for comparison with, and improvements of, current time scales. We found several new and potentially useful biohorizons that help refining the chronology of this critical interval of time encompassing a long and biochronologically poorly known Chron C24r. We furthermore observed an apparent correlation between rock-magnetic properties of the sediments and global climate variability as revealed by a reference benthic $\delta^{18}O$ record from the literature, whereby higher relative amounts of oxidized magnetic phases such as hematite and/or maghemite seem to correlate to extreme warm periods like the PETM at ~55 Ma and the early Eocene from ~54 to ~52.5 Ma. Mechanisms able to explain this apparent coupling between rock-magnetic variability and long-term global climate are presently under scrutiny.

1. Introduction

During the late Paleocene–early Eocene, the Earth experienced a global warming trend that culminated in the early Eocene climatic optimum (EECO; e.g. Zachos et al., 2001), characterized by warm climate conditions at even extreme high latitudes (McKenna, 1980; Moran et al., 2006), subdued latitudinal temperature gradients (Wolfe, 1980; Estes and Hutchison, 1980; Axelrod, 1984), and virtually nonexistent polar ice sheets (Wise et al., 1991; Zachos et al., 1994). This warming trend was punctuated by several short-lived hyperthermal events (Cramer et al., 2003), the most prominent of which was the Paleocene Eocene thermal maximum (PETM; e.g. Kennett and Stott, 1991).

The magneto-biochronology of this critical time interval is however still poorly defined, essentially because of the controversial and ambiguous relationships between paleontologic and magnetic events due to the presence of unconformities in several deep-sea and shallow water sections from the literature around the Paleocene–Eocene boundary (e.g. DSDP Sites 549 and 550) (Aubry et al., 1996), and the lack of (magnetic) resolution in the long Chron C24r interval (Berggren et al., 1995 and references therein).

We present the magnetostratigraphy and calcareous nannofossil biostratigraphy of the upper Paleocene–lower Eocene Cicogna section from the Venetian Southern Alps (NE Italy). The Cicogna section consists of ~81 m of continuously exposed marine marlstones, with no apparent variations in sediment accumulation rates, and thus offers the possibility to assess in detail the magneto-biochronology of this time interval for comparison with, and potential improvement of, the current reference time scale of Berggren et al. (1995, hereafter referred to as BKSA95). An assessment of the rock-magnetic content of the section is also presented and used in conjunction with benthic oxygen isotope data from the literature to put forward a speculative model of climate-controlled rock-magnetic variability over the late Paleocene–early Eocene, which will be extensively developed in a parallel paper in preparation.

2. Geological setting

The Venetian Southern Alps consist of a series of paleogeographic domains that developed since the Early Jurassic, namely the Trento Plateau, the Belluno Basin, and the Friuli Platform (Fig. 1) (e.g. Gaetani and Jadoul, 1979; Winterer and Bosellini, 1981; Doglioni and Bosellini, 1987; Castellarin and Cantelli, 2000). Cretaceous to lower Eocene marine sediments crop out extensively in the Belluno Basin to the south

* Corresponding author. Department of Geosciences, University of Padova, Via Giotto 1, I-35137 Padova, Italy.
E-mail address: edoardo.dallanave@unipd.it (E. Dallanave).

0012-821X/$ – see front matter © 2009 Elsevier B.V. All rights reserved.
doi:10.1016/j.epsl.2009.05.033

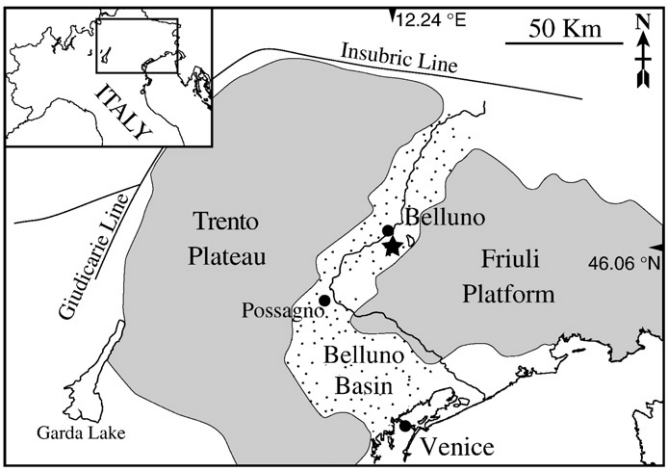

Fig. 1. Geologic sketch map of the Venetian Southern Alps with indication of key paleogeographic domains. The Cicogna section (star; Lat. = 46.06 °N; Long. = 12.24 °E) is located in the Belluno Basin ~8 km to the south of the town of Belluno along the Cicogna riverbed.

of the town of Belluno, where the Cicogna section of this study is located (Fig. 1). These pelagic to hemipelagic sediments, up to 200–250 m in thickness, are mainly represented by well bedded, pink to red limestones and marly limestones, hereafter referred to as Scaglia Rossa *sensu lato (s.l.)*, which includes lithostratigraphic units that still need formal ratification (Di Napoli Alliata et al., 1970; Costa et al., 1996). The Scaglia Rossa *s.l.* is overlain by lower–middle Eocene mainly siliciclastic turbidites pertaining to the Belluno Flysch (Stefani and Grandesso, 1991), which represents the foredeep deposits of the west-verging Dinaric thrusts (Doglioni and Bosellini, 1987).

2.1. The Cicogna section

The Cicogna section (46.06°N, 12.24°E) is located about 8 km south of Belluno along the Cicogna riverbed (Fig. 1), and consists of ~81 m of continuously exposed hemipelagic sediments pertaining to the Scaglia Rossa *s.l.*, capped by the Belluno Flysch (Fig. 2). Bedding planes dip to the NW (~315°N) by about ~45°. The basal 20 m of the section consists of gray-greenish couplets of marlstones and marly limestones, which are replaced, from ~20 m up to 28.7 m by pink-reddish marls with no apparent rhythmicity. The interval comprised between 28.7 m and 31.7 m consists of clayey marls attributed to the Clay Marl Unit (CMU), which represents the lithological expression of the PETM in the Belluno Basin (Giusberti et al., 2007). The interval from the top of the CMU up to 39.2 m is characterized by the re-occurrence of marl-limestone couplets, whereas from 39.2 m up to ~75.0 m at the first significant inception of siliciclastic material of the Belluno Flysch, the succession is essentially characterized by red marls with no apparent rhythmicity. Finally, the interval from 75.0 m to 80.6 m is characterized by red marls alternating with siliciclastic layers, which become dominant from 80.6 m (formal base of the Belluno Flysch) upward (Fig. 2).

3. Calcareous nannofossil biostratigraphy

Calcareous nannofossil analyses have been performed on 185 samples taken on average every 1 m; a sampling resolution of 10–20 cm was adopted close to key biohorizons and across critical intervals like the PETM. Standard smear-slides were prepared from all samples. The material was disaggregated by mechanical means and no anomalous or selective breakage due to preparation was observed. The nannofossil size fraction was not concentrated through settling techniques. Calcareous nannofossils were observed in the light microscope Zeiss Axiophot 40 at a magnification of 1250×. The taxonomy used in this paper is described in Perch-Nielsen (1985), and the zonal schemes adopted are those of Martini (NP; 1971) and Okada and Bukry (CP; 1980). Taxa abundances were determined by counting the index species along three smear-slide transects (representing an area of about 9 mm^2). The abundance patterns of *Fasciculithus*, *Zygrhablithus* and *Girgisia gammation* were determined by counting index species in a prefixed area (1 mm^2) (Backman and Shackleton, 1983). Abundance patterns of *Discoaster araneus*, *Discoaster anartios,* and *Sphenolithus radians* were determined by counting a prefixed number of taxonomically related forms (Rio et al., 1990), i.e., 50 discoasterids and 100 sphenoliths. The calcareous nannofossil biohorizons have been defined using the abundance patterns of the index species as follows: Lowest Occurrence (LO), Lowest Rare Occurrence (LRO), Lowest Common Occurrence (LCO), Highest Occurrence (HO), Highest Common Occurrence (HCO) and Crossover (CO) (see Raffi et al., 2006 for additional information).

Calcareous nannofossil assemblages are usually rich and well diversified, and the preservation varies from poor to moderate. Reworked forms are rare, saved for discrete, siliciclastic-rich intervals containing reworked Cretaceous specimens. In the lower part of the section, the assemblages are mainly composed of common *Toweius* and *Coccolithus* in association with *Sphenolithus*, *Fasciculithus*, *Zygrhablithus, Prinsius*, *Discoaster, Ericsonia*, and *Octolithus*. Upward, the relative abundance of heterococcoliths, which mainly consist of *Coccolithus* and *Toweius*, show a gradual decrease, associated with a prominent increase of *Sphenolithus* and *Zygrhablithus*.

In particular, we identified the following main calcareous nannofossil biohorizons (Fig. 2, Table A1).

- The LO of *Discoaster mohleri*, which defines the base of Zone NP7 (or CP6). In the Cicogna section, *D. mohleri* is found to be continuously present from the section base.
- The LO of *Discoaster multiradiatus*, which marks the base of Zone NP9a (and CP8a). This biohorizon occurs at the 9.90 m level and represents one of the most reliable Paleocene datums.
- The LO and HO of *Ericsonia robusta*, which designate a distinct stratigraphic range; in particular, the LO of *E. robusta*, observed at the 3.97 m level, shortly precedes the LO of *D. multiradiatus*, while the HO of *E. robusta*, identified at the 11.2 m level, correlates with the C25n/C24r boundary.
- Some heavily calcified *Fasciculithus* species suffered an abrupt extinction in correspondence with the onset of the PETM interval, which occurs at the 27.73 m level, thus decreasing the species diversity significantly.
- The LOs of the genus *Rhomboaster* and the Calcareous Nannofossil Excursion Taxa (CNET), which include *Rhomboaster calcitrapa* gr., *D. anartios,* and *D. araneus*, are used to subdivide Zones CP8 and NP9 (Bukry, 1973; Aubry et al., 2000). These unusual taxa are found to be stratigraphically restricted to the PETM, being distributed from 28.88 m to 32.52 m.
- *Fasciculithus* shows a first marked decrease in abundance in coincidence with the bloom of *Zygrhablithus bijugatus* at the 31.60 m level. The final extinction of this genus occurs above the PETM at the 34.73 m level.
- The *Tribrachiatus* lineage, which includes *T. bramlettei, T. contortus,* and *T. orthostylus*, provides several valuable biohorizons that are

Fig. 2. The late Paleocene–early Eocene Cicogna section. To the left: lithostratigraphic log of the section [T1 = Carbonate turbidite level; T2 = Sandy turbidite level; T3 = Belluno Flysch turbidite; CMU = clay marl unit (Giusberti et al., 2007); the carbonate content is referred to the Scaglia Rossa *s.l.* formation]. In the mid part of the diagram are the abundance patterns of selected calcareous nannofossil species discussed in the text. To the right are the standard nannofossil zonations placed next to magnetic polarity zones shown by filled (open) bars for normal (reverse) polarity, which have been correlated to the CK95 geomagnetic polarity time scale (Cande and Kent, 1995). See text for discussion.

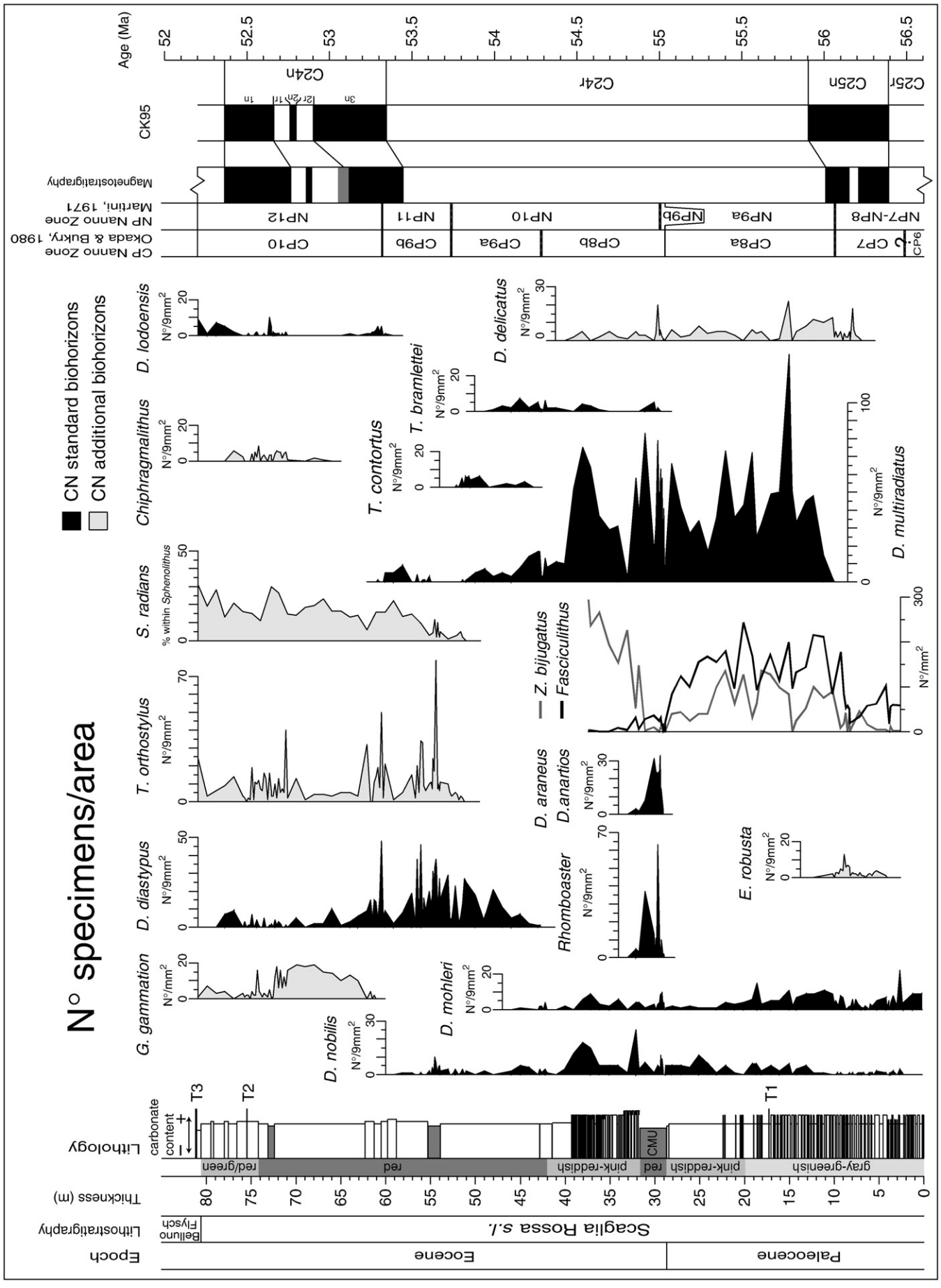
Age (Ma)
52
52.5
53
53.5
54
54.5
55
55.5
56
56.5
CK95
Magnetostratigraphy
C24n
C24r
C25n
C25r
CP Nanno Zone
Okada & Bukry, 1980
NP Nanno Zone
Martini, 1971
CP10
CP9b
CP9a
CP8b
CP8a
CP7
CP6
NP12
NP11
NP10
NP9b
NP9a
NP7-NP8
Epoch
Lithostratigraphy
Lithology
Thickness (m)
Paleocene
Eocene
Scaglia Rossa s.l.
Belluno Flysch
carbonate content
gray-greenish
pink-reddish
red
CMU
red/green
T1
T2
T3
N° specimens/area
CN standard biohorizons
CN additional biohorizons
D. lodoensis
Chiphragmalithus
S. radians
% within Sphenolithus
T. orthostylus
D. diastypus
G. gammation
D. nobilis
D. mohleri
T. contortus
T. bramlettei
D. delicatus
D. multiradiatus
Z. bijugatus
Fasciculithus
D. araneus
D.anartios
Rhomboaster
E. robusta
N°/9mm2
N°/mm2

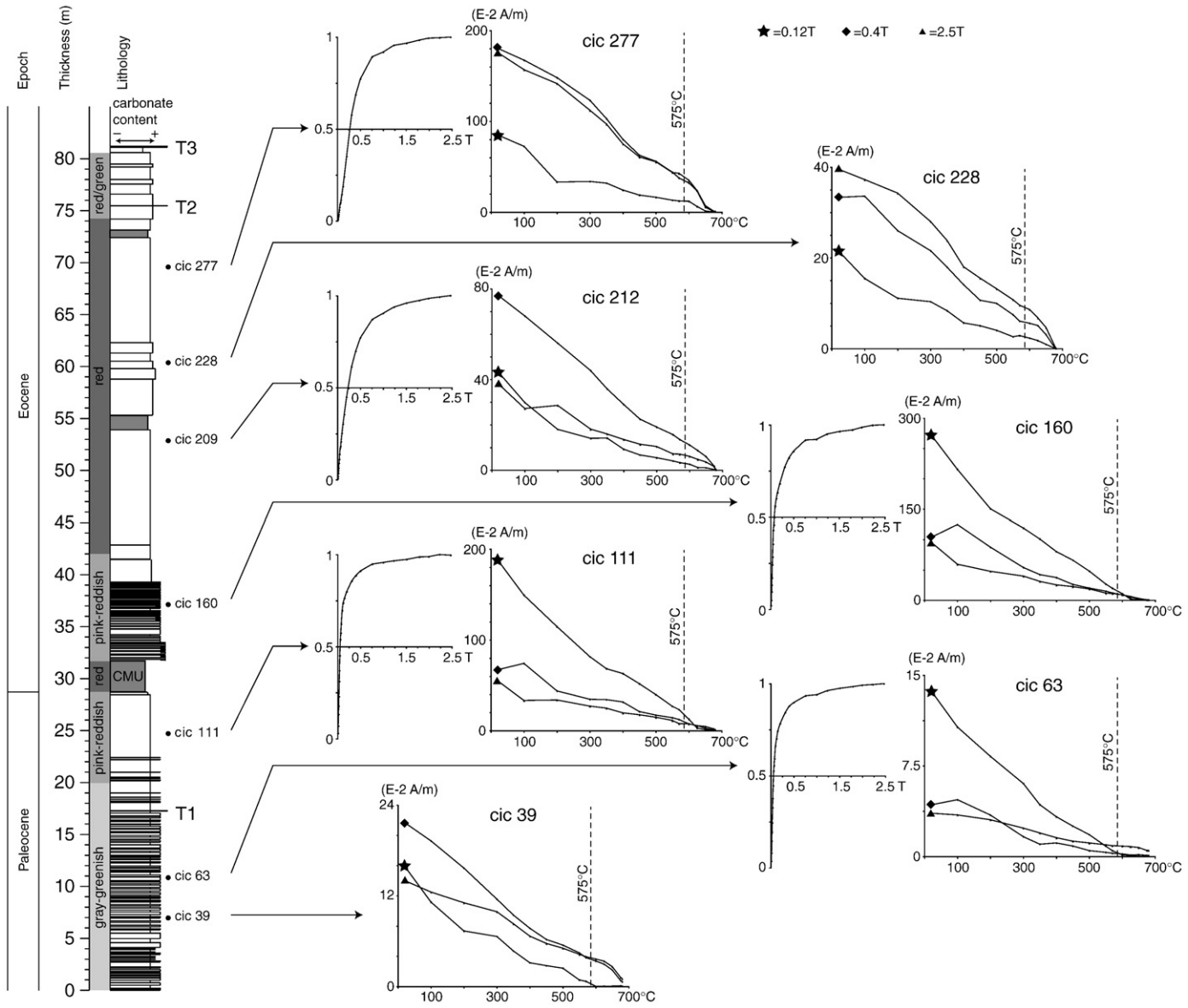

Fig. 3. Isothermal Remanent Magnetization (IRM) acquisition curves (normalized) and thermal unblocking characteristics of orthogonal axis IRMs for representative samples of the Cicogna section.

used to subdivide the early Eocene. The LO of *T. bramlettei*, at the 29.43 m level, marks the base of Zone NP10; the LO of *T. contortus*, at the 45.50 m level, defines, together with the LO of *Discoaster diastypus* (at the 42.70 m level), the base of Zone CP9a (Bukry, 1973); the HO of *T. contortus*, at the 52.70 m level, identifies the base of Zone NP11 (or CP9b). In addition, the extinction of *T. contortus* well correlates with three additional bioevents, namely the LOs of *T. orthostylus* and *S. radians*, found at the 51.30 m level, and the HCO of *D. multiradiatus*, observed at the 51.50 m level.

- The LO of *D. lodoensis* at the 60.40 m level is followed by an absence interval up to 71.10 m, from which level *D. lodoensis* has been consistently found again (*D. lodoensis* LCO). The LCO of *D. lodoensis* has been found to virtually coincide with the LCO of circular *Chiphragmalithus* (albeit circular specimens ascribable to this genus have been sporadically observed from the 66.5 m level).
- The LO of *G. gammation* lies between the LO and LCO of *D. lodoensis* at the 61.20 m level. This biohorizon is potentially useful to subdivide Zone CP9b (or NP11).

These biostratigraphic events indicate that the Cicogna section appears to be stratigraphically complete at least to within nannofossil biostratigraphic resolution, and spans a late Paleocene–early Eocene time interval encompassing Zones NP7/NP8–NP12, equivalent to Zones CP6–CP10. The Paleocene–Eocene boundary is placed at the base of the Clay Marl Unit and virtually coincides with the LOs of the genus *Rhomboaster* and the Calcareous Nannofossil Excursion Taxa, which define the base of Zones CP8b and NP9b (Bukry, 1973; Aubry et al., 2000).

4. Paleomagnetism

Paleomagnetic samples were drilled and oriented in the field at an average sampling interval of ~0.25 m giving a total of 319 standard ~11 cc specimens for analyses, conducted at the Alpine Laboratory of Paleomagnetism (Cuneo, Italy). A representative suite of samples was subjected to rock magnetic analysis using isothermal remanent magnetization (IRM) acquisition curves up to 2.5 T imparted by an *ASC Pulse Magnetizer*. The IRM curves can be divided into two groups,

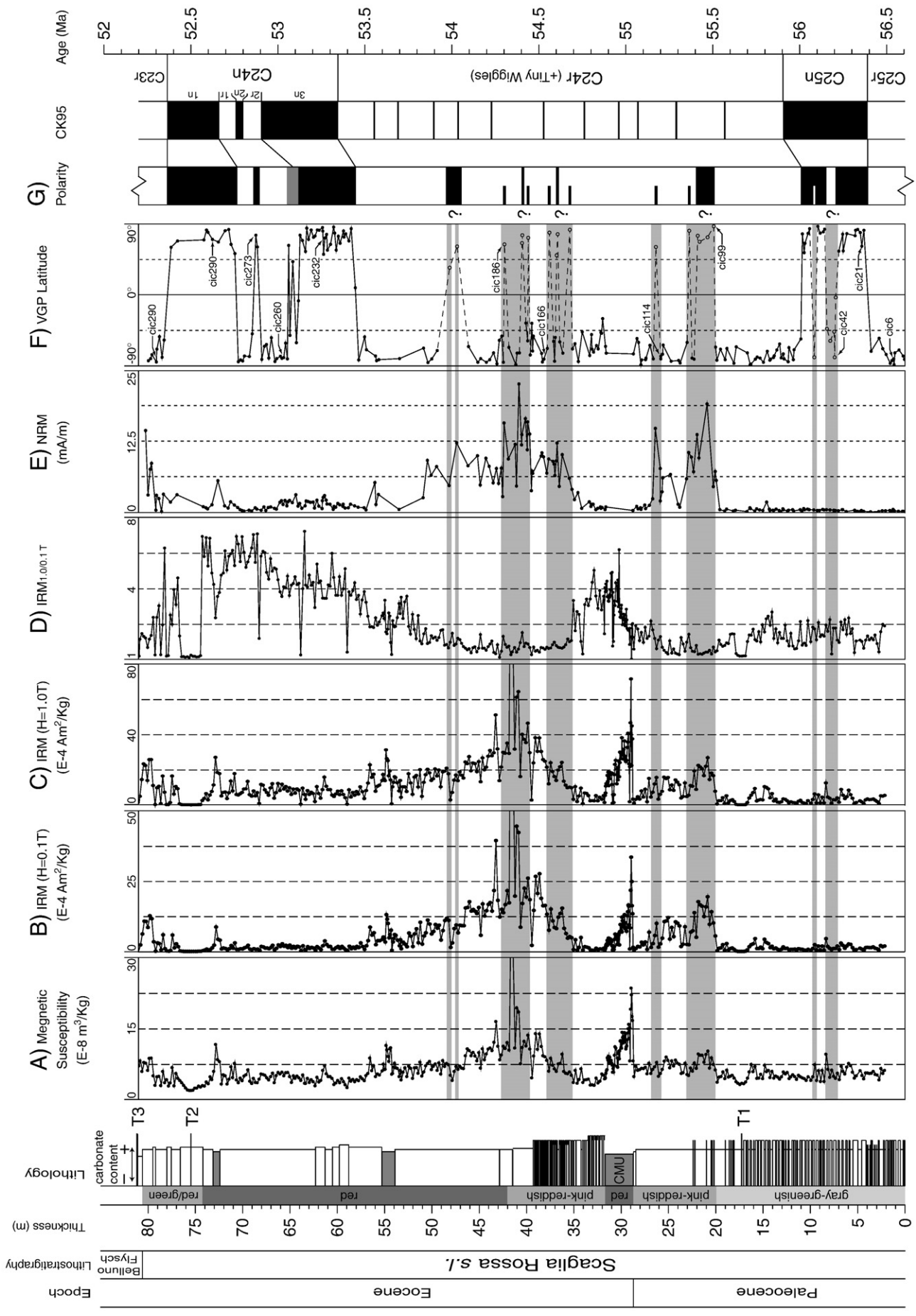

Fig. 4. Magnetic stratigraphy of the Cicogna section. Columns A–E summarize the main magnetic properties of the section as discussed in the text; column F reports the latitude of the virtual geomagnetic poles used to erect the magnetic polarity stratigraphy (G; black for normal polarity, white for reverse polarity); the correlation with the CK95 geomagnetic polarity time scale of Cande and Kent (1995) is also indicated. See text for discussion.

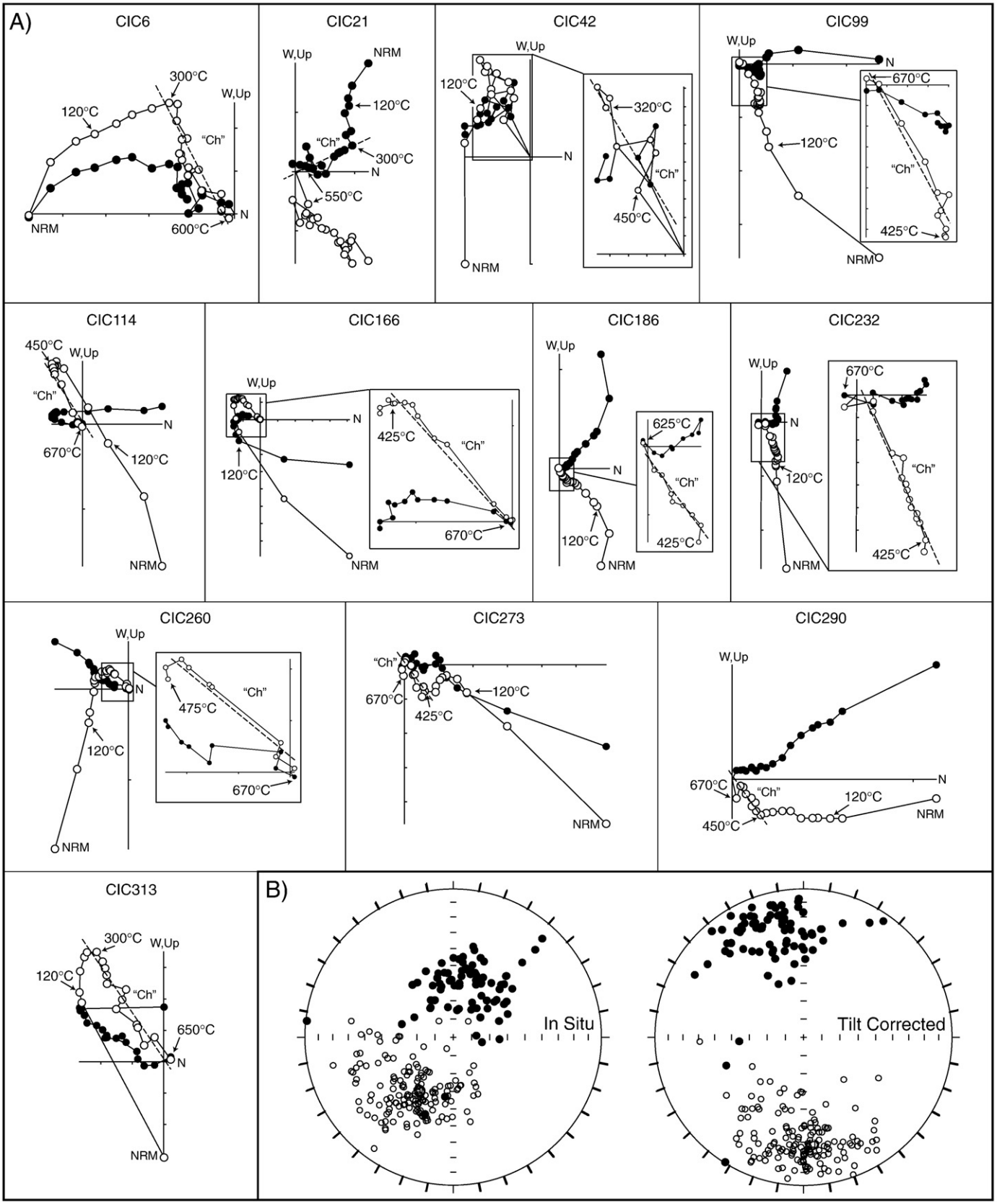

Fig. 5. (A) Vector end-point demagnetization diagrams of NRM of representative samples from the Cicogna section. Closed circles are projections onto the horizontal plane and open circles are projections onto the vertical plane in *in situ* coordinates. (B) Equal area projections before (*in situ*) and after bedding tilt correction for the characteristic "Ch" component directions from the Cicogna section. See text for discussion.

showing different behaviors. In samples collected from the lower gray-greenish to pink ~25 m of the section, the IRM increases initially steeply up to applied fields of ~0.2–0.3 T and then starts climbing gently without reaching saturation up to 2.5 T (Fig. 3, samples cic63, cic111). In samples collected from ~25 m up to the section top, the IRM increases initially less steeply up to fields of ~0.5 T and then continues to climb gently without reaching saturation up 2.5 T (Fig. 3, samples cic160, cic212, cic277). These types of behavior suggest the presence of variable amounts of low coercivity and high coercivity components, with a tendency for the high/low coercivity component ratio to increase upsection. These samples were successively subjected to thermal demagnetization of a three-component IRM imparted in 2.5, 0.4, and 0.12 T fields along three orthogonal directions (Lowrie, 1990) (Fig. 3). Thermal unblocking characteristics of orthogonal IRMs show that samples from the lower ~20 m of the section, green-gray in color, contain a low coercivity component (revealed by the 0.12 T curve) with maximum unblocking temperatures of ~570 °C interpreted as magnetite. The mid-high coercivity (0.4 T and 2.5 T) curves show maximum unblocking temperatures of 650–680 °C consistent with the occurrence of hematite; the presence in these curves of an inflection between ~300 and 400 °C suggests that at least part of this hematite may derive from the transformation of an original maghemite phase during thermal demagnetization treatment (Fig. 3, samples cic39 and cic63). From ~20 m up to the section top, where sediment color becomes progressively more red, samples show the exclusive presence of coercivity components with maximum unblocking temperatures around 650–680 °C, interpreted as hematite; similarly to what described above, the presence in the mid-high coercivity curves of an inflection between ~300 and 400 °C suggests the break-down of an original maghemite phase during thermal demagnetization (Fig. 3, samples cic111–cic277).

A total of 450 unoriented ~5 gr samples were also collected every 20 cm (every 5 cm across the CMU) to obtain detailed information on the rock-magnetic variations throughout the section. Magnetic susceptibility of each sample was measured on a AGICO KLY-3 Kappabridge susceptibility bridge (Fig. 4A). The samples were successively magnetized in 0.1 T and 1.0 T fields, and the values of the IRMs were measured on a *2G DC-SQUID* cryogenic magnetometer (Fig. 4B, C). The susceptibility and IRM curves show relatively high values corresponding to stratigraphic levels pertaining to the CMU as well as levels straddling the ~20–22 m and ~40–45 m interval. The 1.0/0.1 T IRM ratio ($IRM_{1.0/0.1\ T}$) (Fig. 4D) shows low values in the lower ~25 m of the section, followed by a ~7 m-thick excursion high values starting at the base of the CMU and ending above it at ~36 m. Above this level, the ratio follows a more progressive increasing trend from ~45 m up to the section top, interrupted by occasional levels with very low values correlative with more siliciclastic intervals. Recalling that the bulk rock-magnetic experiments showed that a magnetite–maghemite mixture dominates the lower gray-greenish ~20 m of the section, and that a hematite–maghemite mixture dominates the mid-upper part of the section, we conclude that the IRM ratio is ultimately controlled by the relative proportion of higher versus lower coercivity phases within the triad magnetite–maghemite–hematite, whereby the lower the ratio, e.g. in the lower ~20 m of the section, the higher the magnetite content, whereas the higher the ratio, e.g. across the CMU and from ~45 m upwards, the higher the contribution of hematite–maghemite.

The natural remanent magnetization (NRM) intensity of the 319 oriented ~11 cc specimens ranges between 0.04 and 22.6 mA/m with two peak values at ~20–27 and ~35–54 m that broadly correspond to those observed in the 0.1 and 1.0 T IRM curves (Fig. 4E). All the samples were demagnetized in maximum steps of 50 °C, and the component structure of the NRM was monitored after each demagnetization step by means of vector end-point demagnetization diagrams (Zijderveld, 1967); steps of 10–25 °C were adopted close to critical unblocking temperatures. Magnetic components were calculated by standard least-square analysis (Kirschvink, 1980) on linear portions of the demagnetization paths and plotted on equal-area projections.

Scattered magnetic component directions with positive (down-pointing) inclinations in geographic (*in situ*) coordinates have been commonly observed from room temperature up to an average of ~200–300 °C. Removal of these spurious magnetizations revealed the presence of a characteristic component linearly trending to the origin of the demagnetization axes. This characteristic component was isolated in 229 (71.5%) specimens by linear interpolation of the demagnetization steps from ~300 °C to ~525 °C in specimens from the lower ~20 m of the section (Fig. 5A, cic6–cic42), and from ~425 °C to ~625 °C in specimens from meter level ~20 to the section top (Fig. 5A, cic99–cic313). These characteristic magnetizations are oriented NE-and-down or SW-and-up in geographic (*in situ*) coordinates; after correction for homoclinal bedding tilt, they turn to NNW-and-down or SSE-and-up (Fig. 5B, Table 1). These populations depart from antipodality by ~16°, which we attribute to residual contamination from lower temperature components, and fail to pass the reversal test at the 95% level of confidence using the procedure suggested by Watson (1983) ($V_0 = 47.7$; $V_{critical} = 6.2$; for further details on the procedure, see also McFadden and McElhinny, 1990). The effect of the contaminating bias on the mean direction could be minimized by inverting all directions to common polarity, which resulted in a tilt corrected mean direction of Dec. = 355.4°, Inc. = 28.3° ($k = 12.2$, $\alpha_{95} = 2.8°$; Table 1).

To constrain the age of the characteristic magnetization and assign polarity to the NNW-and-down or SSE-and-up characteristic

Table 1
Characteristic component directions and paleomagnetic pole from the Cicogna section.

N	MAD	Geographic (in situ) coordinates				Bedding (tilt-corrected) coordinates				
		k	α_{95}	GDEC	GINC	k	α_{95}	BDEC	BINC	BINC*
Normal polarity directions										
79	7.7 ± 4.4	13.7	4.5	16.5	61.2	13.6	4.5	343.5	26.1	–
Reverse polarity directions										
150	6.9 ± 3.9	13.7	3.2	218.5	−50.8	13.6	3.2	181.8	−29.1	–
Reverse and normal polarity directions										
229	7.2 ± 4.1	12.4	2.8	32.2	54.8	12.2	2.8	355.4	28.3	$53.1^{59.8}_{44.3}$

Paleomagnetic pole Ci1					Paleomagnetic pole Ci2	
N	K	A_{95}	LONG	LAT	LONG	LAT
229	12.6	2.7	200.8	58.8	209.7	77.1

N=number of sample; MAD=mean angular deviation of the mean paleomagnetic direction expressed in degrees; *k* and K=Fisher precision parameter of the mean paleomagnetic direction and pole, respectively; α_{95} and A_{95}=Fisher angle of half cone of 95% confidence about the mean paleomagnetic direction and pole, respectively; GDEC and GINC=declination and inclination in geographic (*in situ*) coordinates of the mean paleomagnetic direction; BDEC and BINC=declination and inclination in bedding (tilt-corrected) coordinates of the mean paleomagnetic direction; BINC*=inclination of the mean paleomagnetic direction corrected for inclination shallowing; LONG and LAT=longitude and latitude of the mean paleomagnetic pole before (Ci1) and after (Ci2) correction for inclination shallowing.

directions, we compared the mean paleomagnetic pole from Cicogna (Ci1; Long. = 200.8°E, Lat. = 58.8°N, A_{95} = 2.7°; Fig. 6A, Table 1), obtained by averanging the virtual geomagnetic poles (VGPs) of the characteristic component directions, to the late Cretaceous–early Miocene master apparent polar wander (APW) path for Africa of Besse and Courtillot (2002, 2003). The paleogeographic affinity of the Southern Alps with Africa has been demonstrated at least since the Permian (Muttoni et al., 2001) insofar as relatively less deformed regions of Adria such as the Adriatic foreland or portions of the Southalpine chain (e.g., the Dolomites) maintained substantial tectonic coherence (within paleomagnetic resolution) with Africa during Alpine deformation in the Cenozoic (Muttoni et al., 2003; Muttoni et al., 2004; Rosenbaum et al., 2004; Agnini et al., 2006). The Cicogna Ci1 paleopole is however removed from the late Paleocene–

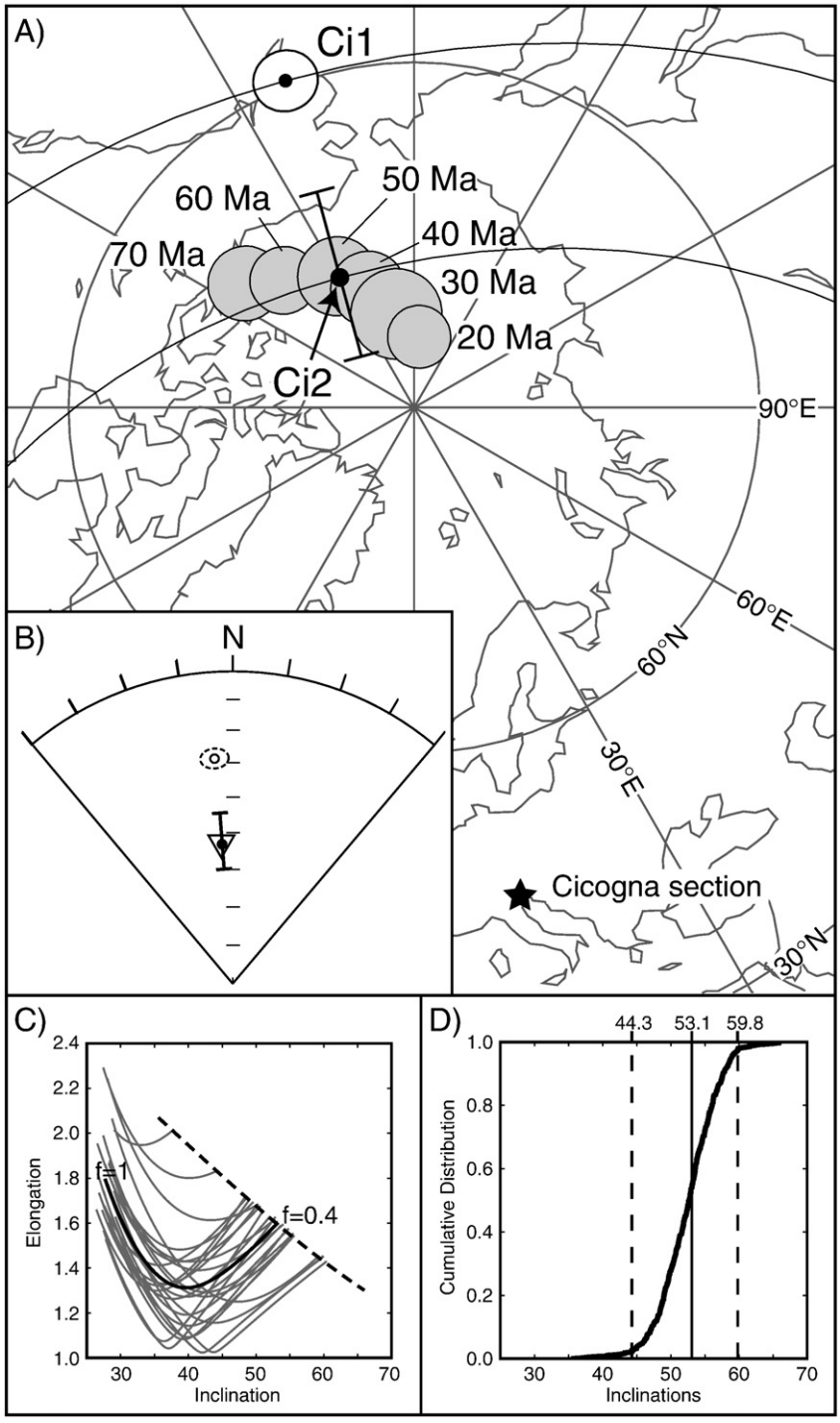

Fig. 6. (A) The mean paleomagnetic pole from the Cicogna section before (Ci1) and after (Ci2) directional unflattening is compared to the master apparent polar wander path of Africa for the 20–70 Ma interval (Besse and Courtillot, 2002, 2003) (map drown with PaleoMac; Cogné, 2003). (B) The characteristic mean direction from the Cicogna section before (open circle) and after (closed circle) directional unflattening, with the associated 95% confidence boundaries (dashed circle and error bar, respectively); these mean directions are compared to the mean direction expected at Cicogna from the 50 Ma paleopole of Africa (open triangle). (C) The *E*/*I* values of the systematically unflattened directions with the unflattening parameter *f* ranging from 1 to 0.4 (heavy line) are compared to the E/I values predicted by the TK03.GAD geomagnetic field model (dashed line). 25 of 500 boostrapped dataset are shown by the light lines. (D) Diagram of the cumulative distribution of all inclinations derived from the bootstrapped crossing points, with the associated 95% confidence boundaries (44.3°–59.8°) around the mode (53.1°).

early Eocene APW path of Africa by ~18° in the far-side direction of the sampling site (Fig. 6A). This is because the characteristic component mean direction is shallower by ~25° with respect to the inclination expected at Cicogna from the African APW path (Fig. 6B). The mean unblocking temperature of characteristic component and the rock-magnetic analyses suggest that the magnetization at Cicogna is carried primarily by hematite. Hematite particles can be associated with magnetic inclination that is shallower compared to the external geomagnetic field direction (Tauxe and Kent, 1984). We used the elongation/inclination (E/I) method of Tauxe et al. (2008) to detect and correct for inclination shallowing. In brief, a given directional data set is progressively "unflattened" and the elongation parameter E is evaluated at each unflattening step with the aim to find the unflattening level (f) at which the inclination and elongation are consistent with a statistical dipole field model (TK03.GAD; see Tauxe et al., 2008 for further information).

We systematically unflattened the Cicogna characteristic directions by applying values of f ranging from 1 to 0.4, and at each unflattening step, E/I values were calculated (Fig. 6C, heavy curve); at $f=0.4$, the E/I pair most consistent with the TK03.GAD field model (Fig. 6C, dashed line) was attained. To assess the uncertainty of this estimate, we repeated the analysis by means of bootstrap technique;

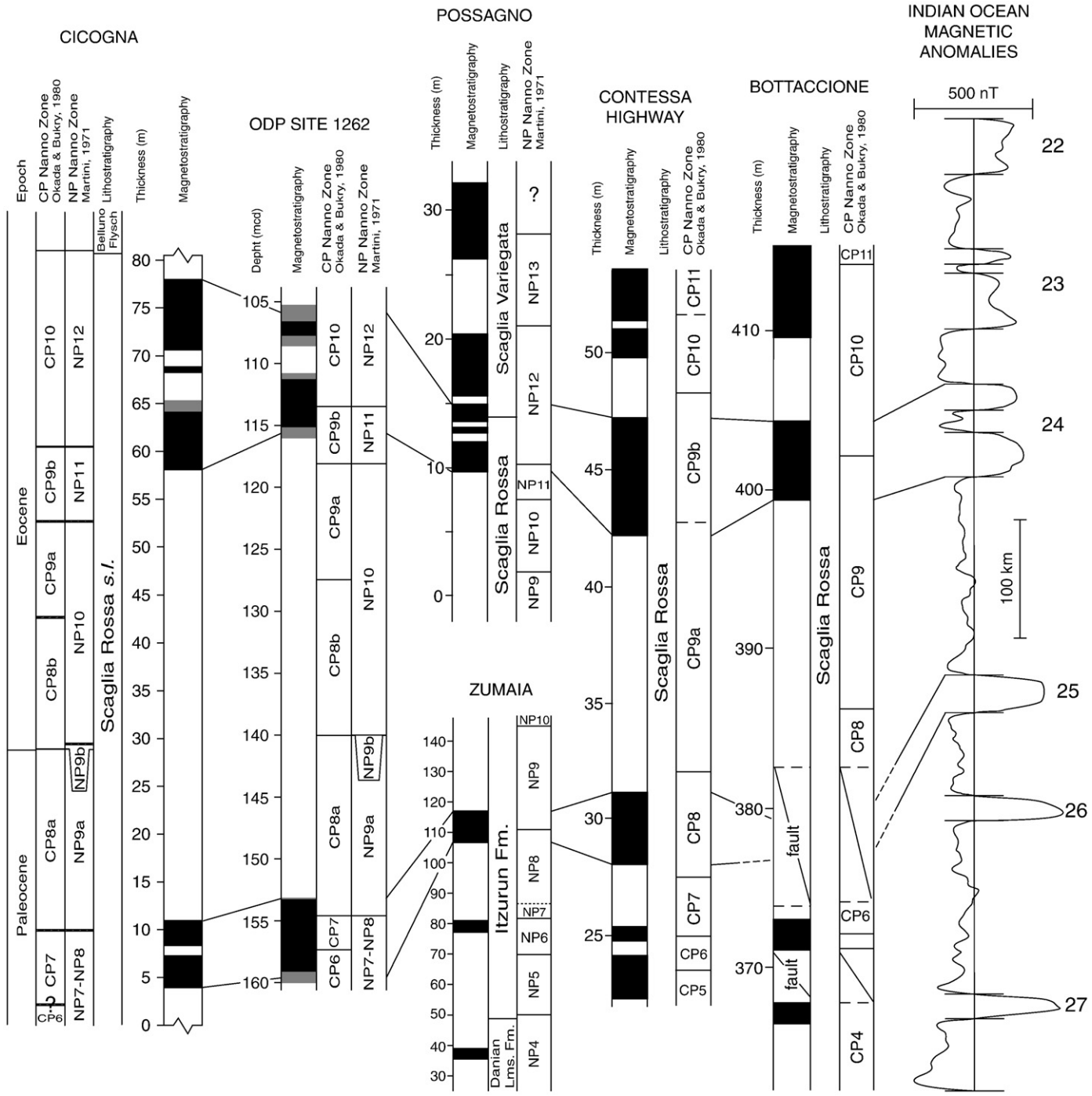

Fig. 7. The magneto-biostratigraphy of the Cicogna section is correlated to coeval magneto-biostratigraphies from ODP Site 1262, Possagno (Venetian Southern Alps, Italy), Zumaia (Basque Basin, Spain), Contessa Highway and Bottaccione (Central Apennines, Italy), as well as to a composite stacked profile of Indian Ocean marine magnetic anomalies from anomaly 27 to 22 (Cande and Kent, 1992). See text for discussion.

25 of 500 examples of bootstrapped data are shown as light lines in Fig. 6C. The corrected (unflattened) mean charcteristic inclination and associated 95% confidence band (Inc. = $53.1^{59.8}_{44.3}$, Fig. 6D) is now in excellent agreement with the inclination expected at Cicogna from the 50 Ma paleopole of Africa (Fig. 6B). The Cicogna paleopole position after the shallow bias correction (Ci2; Long. = 209.7°E, Lat. = 77.1°N; Table 1) is virtually indistinguishable from the 50 Ma African paleopole (Fig. 6A). We can therefore consider this part of the Alps as tectonically coherent with Africa since the late Paleocene.

5. Magnetostratigraphy

For each sample characteristic magnetization, a virtual geomagnetic pole (VGP) was calculated. The latitude of the samples VGP relative to the mean paleomagnetic (north) pole axis was used for interpreting polarity stratigraphy (Lowrie and Alvarez, 1977; Kent et al., 1995). VGP relative latitudes approaching +90°N or −90°S are interpreted as recording normal or reverse polarity, respectively (Fig. 4F). The VGP data show a ~4 m-thick reverse polarity interval at the base of the section, followed by ~7 m of dominantly normal polarity embedding a ~1 m thick reverse polarity interval documented by five samples (Fig. 4F, G). A reverse polarity sample at 9.6 m was also found. From ~11 m to ~57.7 m, the VGP curve shows prevalent reverse polarity, interrupted by several short normal polarity events in the ~20–49 m interval. These events are mainly represented by one or two specimens, except for the ~2 m-thick interval centered at ~21 m with 4 consecutive normal polarity specimens; these events seem to show a consistent correlation to peak values of susceptibility, IRM, and NRM (Fig. 4). Finally, from ~57.7 m up to the section top (~81 m), the VGP curve shows a well-defined sequence of normal and reverse polarity intervals (Fig. 4F, G).

We compared the Cicogna magneto-biostratigraphy to coeval data from classic sections from the literature, namely Possano from the Southern Alps (Agnini et al., 2006), Bottaccione and Contessa Highway from the Northern Appennines near Gubbio (Lowrie et al., 1982; Napoleone et al., 1983; Monechi and Thierstein, 1985), as well as Zumaia from the Basque Basin (Dinarès-Turell et al., 2002, 2003, 2007) and ODP Site 1262 from the Walvis Ridge (Agnini et al., 2007 and

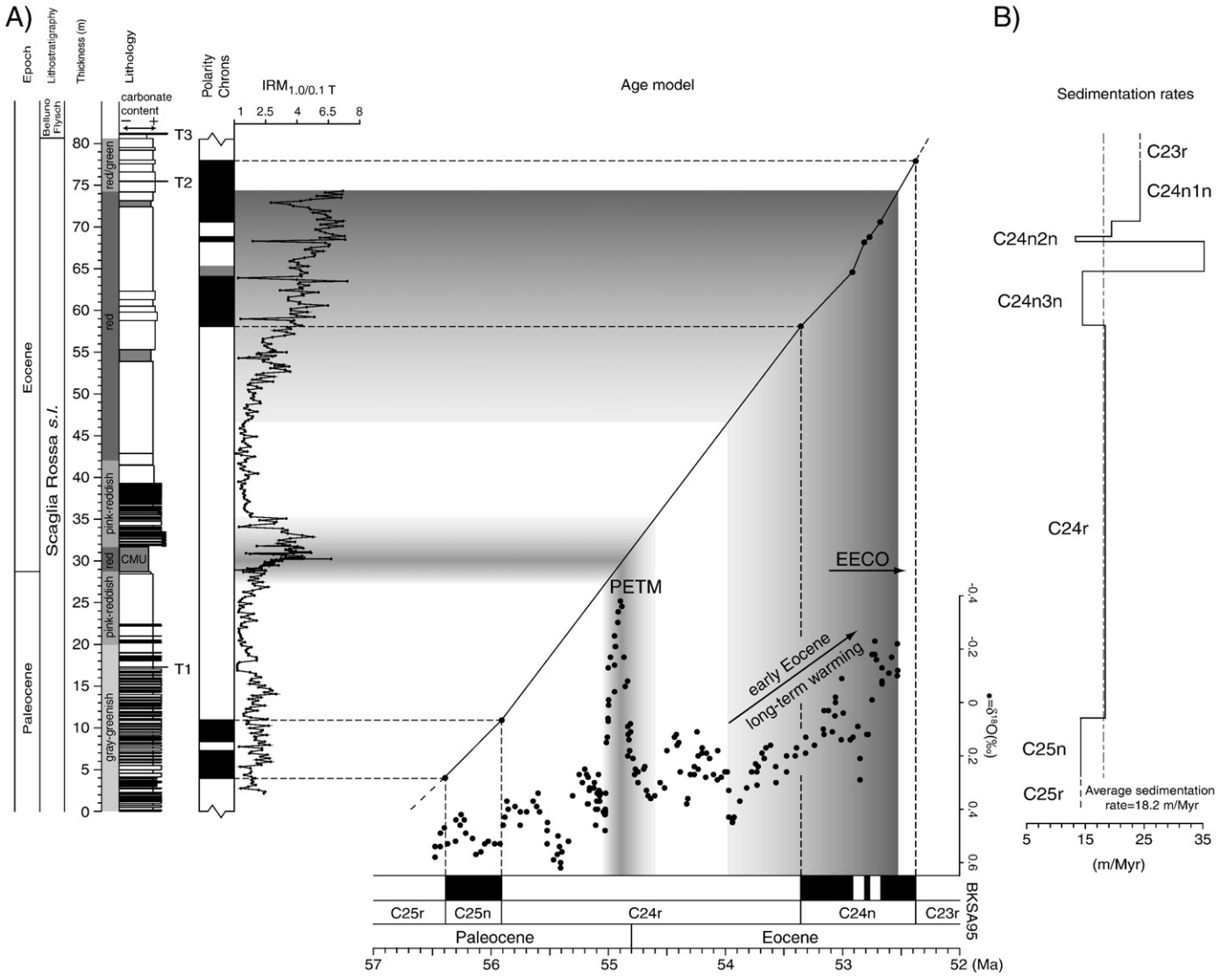

Fig. 8. Age-depth model and derived sediment accumulation rates for the Cicogna section obtained by magnetostratigraphic correlation to the CK95 geomagnetic polarity time scale of Cande and Kent (1995). $IRM_{1.0/0.1\ T}$ values are plotted on the vertical axis to show the correlation with the $\delta^{18}O$ dataset of Miller et al. (2005; horizontal axis). The gray bands highlight positive correlations between high $IRM_{1.0/0.1\ T}$ values (corresponding to high amounts of maghemite–hematite) and low $\delta^{18}O$ values, indicative of warm climate e.g., during the PETM. See text for discussion.

reference herein) (Fig. 7). An excellent magnetostratigraphic matching straddling similar nannofossil zonations was observed between the Cicogna section and the correlative sections from the literature. All these sections could be correlated to the stacked profile of magnetic anomalies 22–27 from the Indian Ocean (Cande and Kent, 1992) (Fig. 7). Within this correlation framework, we observe that the frequently single sample-based normal polarity events present at Cicogna in the ~20–49 m interval and that correlate to peak values of rock-magnetic parameters (Fig. 4), have no obvious counterparts in any of the coeval sections discussed above, nor can be successfully correlated to known tiny wiggles present between marine magnetic anomaly 25 and 24 (Figs. 4G and 7; Cande and Kent, 1992). Hence, we interpret the northward-and-down characteristic directions isolated in these samples as overprints of diagenetic origin recording a post-depositional geomagnetic field of normal polarity. In addition, the ~1 m-thick reverse polarity interval found at Cicogna within Chron C25n (Figs. 4G and 7) was not observed elsewhere in seemingly correlative levels (Fig. 7), and is therefore provisionally considered as dubious. On the basis of these considerations, the Cicogna section shows an overall sequence of 9 magnetozones, encompassing marine magnetic anomalies from 25 to 23 and Chrons from C25r to C23r.

6. Age model of sedimentation and biochronology

We constructed an age-depth plot and derived sediment accumulation rates at Cicogna by means of magnetostratigraphic correlation to the geomagnetic polarity time scale of Cande and Kent (1995; CK95) across the C25r–C23r interval, assuming constant sedimentation rate between magnetochronologic control points (Fig. 8A). We adopted a total of 8 magnetic polarity reversals as chronologic control points, identified between the base of Chron C25n and the top of Chron C24n. The derived age model implies a relatively constant average sediment accumulation rate of ~18 m/Myr throughout the section (Fig. 8B).

Our CK95-based age-depth function has been used to place the sequence of biohorizons recognized at Cicogna in a temporal reference frame for comparison with similar bioevents reported in the BKSA95 time scale, as well as with recent data from ODP Site 1262. Our age-depth function has been also used to place the rock-magnetic variability previously described, particularly the $IRM_{1.0/0.1\ T}$ ratio, in a same temporal reference frame for comparison with climate-proxy data from the literature, as discussed below.

7. Discussion and conclusions

Apart from standard biohorizons, whose ranking and spacing have found to be largely consistent with previous studies (e.g., Backman, 1986; Berggren et al., 1995; Raffi et al., 2005; Agnini et al., 2007 and references herein), the Cicogna section provides several new bioevents in the NP9–NP10 (CP8–CP9a) interval within Chron C24r that were not previously recognized (hence included) in the BKSA95 reference time scale; several of these new biohorizons have been

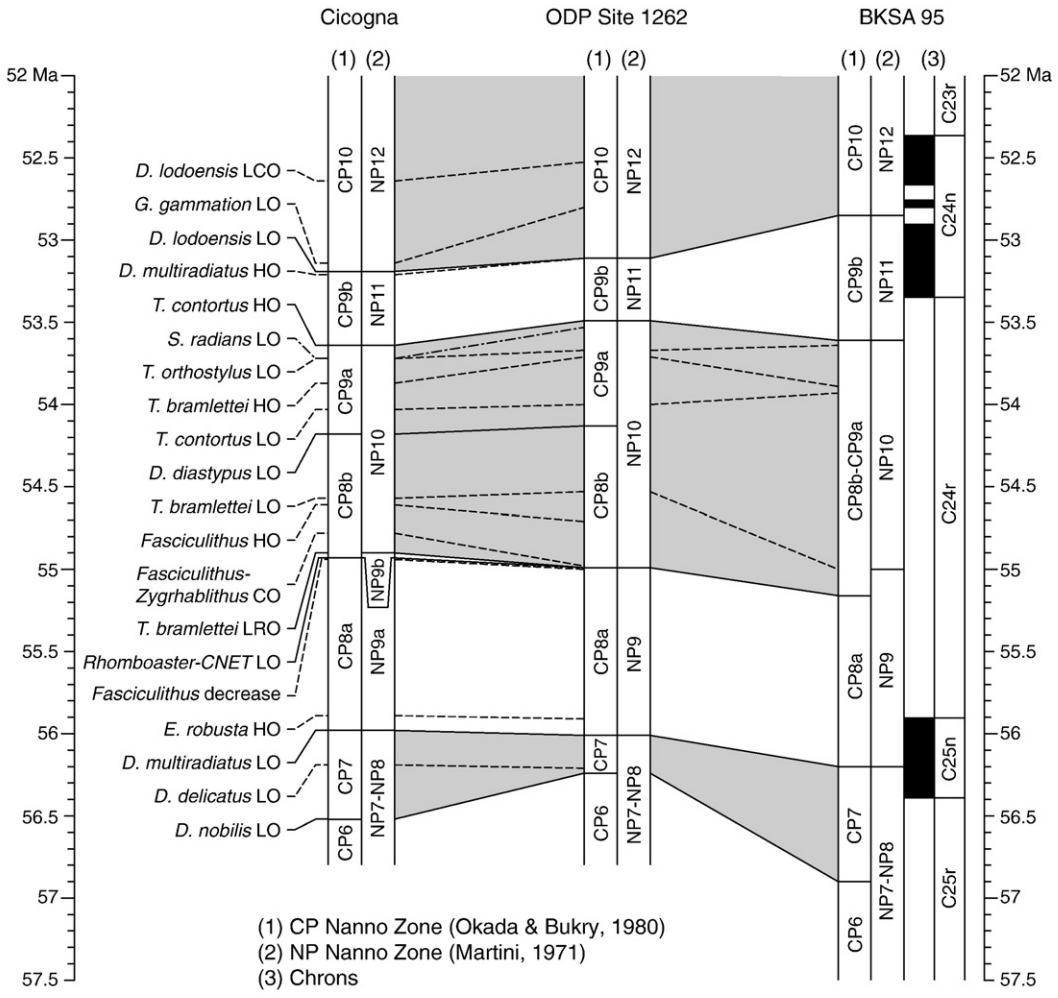

Fig. 9. Biochronologic correlation between the Cicogna section, ODP Site 1262, and the BKSA95 time scale (Berggren et al., 1995); see text for details.

recently observed also at ODP Site 1262 (Fig. 9; Table A1). In particular, useful bioevents were found in the mid part of Chron C24r across the P–E boundary, calibrated to ~54.94 Ma according to our age model; these include:

- The decrease in diversity of the genus *Fasciculithus* at ~54.93 Ma.
- The LOs of the Calcareous Nannofossils Excursion Taxa at ~54.94 Ma, virtually coinciding with the base of Zone CP8b, used to approximate the P–E boundary.
- The crossover in abundance between *Fasciculithus* and *Z. bijugatus* at ~54.8 Ma.
- The HO of the *Fascichulitus* at ~54.6 Ma.

These bioevents are constrained to a very short time interval and are likely related to environmental perturbations associated with the PETM (e.g., Gibbs et al., 2006, Agnini et al., 2007). Above the PETM, three additional bioevents have been identified in the upper part of Chron C24r at ~53.7 Ma (Zone NP11), namely the LO of *S. radians*, the LO of *Tribrachiatus orthostylus*, and the HCO of *D. multiradiatus*. Finally, useful bioevents have been also found within Chron C24n, namely the HO of *D. multiradiatus* at ~53.21 Ma, the LO of *G. gammation* at ~53.1 Ma, and the LO and LCO of *D. lodoensis* at ~53.19 Ma and ~52.6 Ma, respectively (Fig. 9; Table A1).

These new magneto-biostratigraphic data from the expanded and continuously exposed Cicogna section represent an improvement of the late Paleocene–early Eocene chronology, which is not well defined in current time scales (e.g., BKSA95) essentially because of the presence of unconformities in several deep-sea and shallow water sections from the literature (Aubry et al., 1996) and the substantial lack of reference sections provided with a complete and expanded Chron C24r interval (Fig. 7).

In regards to the rock-magnetic properties of the sediments, we observed high $IRM_{1.0/0.1\ T}$ values interpreted as due to high relative amounts of hematite–maghemite in levels attributed to the PETM as well as in levels dated from ~54 Ma to ~52.5 Ma (Fig. 8A). These variations are likely primary in origin; in fact, the Cicogna sediments contain a magnetic remanence carried by hematite and affected by inclination shallowing, which is typical for detrital (i.e., primary) hematite, albeit secondary hematite, possibly associated with normal polarity overprinting, has been also recognized in discrete levels within Chron C24r (Fig. 4, gray bands). We speculate that this (largely) primary rock-magnetic variability may be associated with (global) climate variability. In particular, warm and humid climate conditions typical of the PETM and the early Eocene (e.g., Wolfe, 1980; Estes and Hutchison, 1980; Axelrod, 1984; Zachos et al., 2001), characterized by enhanced continental weathering and runoff (e.g., Sloan and Rea, 1995), may have promoted the formation (and consequent transport and accumulation) of oxidized mineral phases such as maghemite and hematite (e.g., Singer et al., 1996; Barron and Torrent, 2002; Wilson, 2004). In this respect, high relative amounts of detrital hematite–maghemite in the ~55–54.5 Ma interval across the PETM, as well as from ~54 Ma to ~52.5 Ma, seem to correlate to warm global climate conditions as revealed by the benthic $\delta^{18}O$ climate-proxy record of Miller et al. (2005) (Fig. 8A). Several mechanisms able to explain (or reject) this apparent coupling between rock-magnetic variability and global climate, including the weathering of silicate rocks as a buffer to long-term climate change as first described by Walker and Hays (1981), are presently under scrutiny by the authors and will be discussed in a parallel paper.

Acknowledgements

We thank Lisa Tauxe, Dennis V. Kent, and two anonymous reviewers for useful comments that improved this manuscript. E. Dallanave, C. Agnini and D. Rio were supported by MIUR-PRIN Grant # 2007W9B2WE_004.

Appendix A. Supplementary data

Supplementary data associated with this article can be found, in the online version, at doi:10.1016/j.epsl.2009.05.033.

References

Agnini, C., Muttoni, G., Kent, D.V., Rio, D., 2006. Eocene biostratigraphy and magnetic stratigraphy from Possagno, Italy: the calcareous nannofossils response to climate variability. Earth Planet. Sci. Lett. 241, 815–830.
Agnini, C., Fornaciari, E., Raffi, I., Rio, D., Röhl, U., Westerhold, T., 2007. High-resolution nannofossil biochronology of middle Paleocene to early Eocene at ODP Site 1262: implications for calcareous nannoplankton evolution. Mar. Micropaleontol. 64, 215–248.
Aubry, M.-P., Berggren, W.A., Stott, L., Sinha, A., 1996. The upper Paleocene–lower Eocene stratigraphic record and the Paleocene–Eocene boundary carbon isotopes excursion: implications for geochronology. Special Publications, vol. 101. Geological Society, London, pp. 353–380. doi:10.1144/GSL.SP.1996.101.01.18.
Aubry, M.-P., Cramer, B.S., Miller, K.G., Wright, J.D., Kent, D.V., Olsson, R.K., 2000. Late Paleocene event chronology: unconformities, not diachrony. Bull. Soc. Géol. Fr. 171 (3), 367–378.
Axelrod, D.I., 1984. An interpretation of Cretaceous and Tertiary biota in polar regions. Palaeogeogr. Palaeoclimatol. Palaeoecol. 45, 105–147.
Backman, J., 1986. Late Paleocene to Middle Eocene calcareous nannofossil biochronology from the Shatsky Rise, Walvis Ridge and Italy. Palaeogeogr. Palaeoclimatol. Palaeoecol. 57, 43–59.
Backman, J., Shackleton, N.J., 1983. Quantitative biochronology of Pliocene and early Pleistocene calcareous nannoplankton from theAtlantic, Indian and PacificOceans. Mar. Micropaleontol. 8, 141–170.
Barron, V., Torrent, J., 2002. Evidence for a simple pathway to maghemite in Earth and Mars soils. Geochim. Cosmochim. Acta 66, 2801–2806.
Berggren, W.A., Kent, D.V., Swisher III, C.C., Aubry, M.-P., 1995. A revised Cenozoic geochronology and chronostratigraphy. In: Berggren, W.A., et al. (Ed.), Geochronology, Time Scales and Global Stratigraphy Correlation. In: Spec. Publ., vol. 54. Soc. for Sediment. Geol., Tulsa, Okla, pp. 129–212.
Besse, J., Courtillot, V., 2002. Apparent and true polar wander and the geometry of the geomagnetic field over the last 200 Myr. J. Geophys. Res. 107 (B11), 2300. doi:10.1029/2000JB000050.
Besse, J., Courtillot, V., 2003. Correction to "Apparent and true polar wander and the geometry of the geomagnetic field over the last 200 Myr". J. Geophys. Res. 108 (B10), 2469. doi:10.1029/2003JB002684.
Bukry, D., 1973. Low-latitude coccolith biotratigraphic zonation. Proc. Ocean Drill. Prog. Sci. Results 15, 685–703.
Cande, S.C., Kent, D.V., 1992. A new geomagnetic polarity time scale for the Late Cretaceous and Cenozoic. J. Geophys. Res. 97, 13917–13951.
Cande, S.C., Kent, D.V., 1995. Revised calibration of the geomagnetic polarity time scale for the Late Cretaceous and Cenozoic. J. Geophys. Res. 100 (B4), 6093–6096. doi:10.1029/94JB03098.
Castellarin, A., Cantelli, L., 2000. Neo-Alpine evolution of the Southern Eastern Alps. J. Geodyn. 30, 251–274.
Cogné, J.P., 2003. PaleoMac: a Macintosh™ application for treating paleomagnetic data and making plate reconstructions. Geochem. Geophys. Geosyst. 4 (1), 1007. doi:10.1029/2001GC000227.
Costa, V., Doglioni, C., Grandesso, P., Masetti, D., Pellegrini, G.B., Tracanella, E., 1996. Carta Geologica d'Italia, Foglio 063, Belluno. Roma, Servizio Geologico d'Italia, scale 1:50,000, 1 sheet + 74 p.
Cramer, B.S., Wright, J.D., Kent, D.V., Aubry, M.-P., 2003. Orbital climate forcing of d13C excursions in the late Paleocene–early Eocene (chrons C24n–C25n). Paleoceanography 18 (4), 1097. doi:10.1029/2003PA000909.
Di Napoli Alliata, E., Proto Decima, F., Pellegrini, G.B., 1970. Studio Geologico, Stratigrafico e Micropaleontologico dei Dintorni di Belluno. Mem. Soc. Geol. Ital. 9, 1–28.
Dinarès-Turell, J., Baceta, J.I., Pujalte, V., Orue-Etxebarria, X., Bernaola, G., 2002. Magnetostratigraphic and cyclostratigraphic calibration of a prospective Paleocene/Eocene stratotype at Zumaia (Basque Basin, northern Spain). Terra Nova 14, 371–378.
Dinarès-Turell, J., Baceta, J.I., Pujalte, V., Orue-Etxebarria, X., Bernaola, G., Lorito, S., 2003. Untantling the Paleocene climatic rhythm: an astronomically calibrated Early Paleocene magnetostratigraphy and biostratigraphy at Zumaia (Basque Basin, northern Spain). Earth Planet. Sci. Lett. 216, 483–500.
Dinarès-Turell, J., Baceta, J.I., Bernaola, G., Orue-Etxebarria, X., Pujalte, V., 2007. Closing the Mid-Paleocene gap: toward a complete astronomically tuned Paleocene Epoch and Selandian and Thanetian GSSPs at Zumaia (Basque Basin, W Pyrenees). Earth Planet. Sci. Lett. 262, 450–467.
Doglioni, C., Bosellini, A., 1987. Eoalpine and meso-alpine tectonics in the Southern Alps. Geol. Rundsch. 77, 734–754.
Estes, R., Hutchison, J.H., 1980. Eocene lower vertebrates from Ellesmere Island, Canadian Arctic Archipelago. Palaeogeogr. Palaeoclimatol. Palaeoecol. 30, 325–347.
Gaetani, M., Jadoul, F., 1979. The structure of Bergamasc Alps. Rend. Azz. Naz. Lincei, 8, 66, 5, 411–416.
Gibbs, S.J., Bown, P.R., Sessa, J.A., Bralower, T.J., Wilson, P.A., 2006. Nannoplankton extinction and origination across the Paleocene–Eocene Thermal Maximum. Science 314, 1770–1773.
Giusberti, L., Rio, D., Agnini, C., Backman, J., Fornaciari, E., Tateo, F., Oddone, M., 2007. Mode and tempo of the Paleocene–Eocene thermal maximum in an expanded section from the Venetian pre-Alps. Geol. Soc. Amer. Bull. 119, 391–412. doi:10.1130/B25994.1.

Kennett, J.P., Stott, L.D., 1991. Abrupt deep-see warming, paleoceanographic changes and benthic extinctions at the end of the Paleocene. Nature 353, 225–229.
Kent, D.V., Olsen, P.E., Witte, W.K., 1995. Late Triassic–earliest Jurassic geomagnetic polarity sequence and paleolatitudes from drill cores in the Newark rift basin, eastern North America. J. Geo-phys. Res. 100, 14965–14998.
Kirschvink, J.L., 1980. The least-squares line and plane and analysis of paleomagnetic data. Geophys. J. R. Astron. Soc. 62, 699–718.
Lowrie, W., 1990. Identification of ferromagnetic minerals in a rock by coercivity and unblocking temperature properties. Geophys. Res. Lett. 17, 150–162.
Lowrie, W., Alvarez, W., 1977. Upper Cretaceous–Paleocene magnetic stratigraphy at Gubbio, Italy: III. Upper Cretaceous magnetic stratigraphy. Geol. Soc. Amer. Bull. 88, 374–377.
Lowrie, W., Alvarez, W., Napoleone, G., Perch-Nielsen, K., Premoli Silva, I., Toumarkine, M., 1982. Paleogene magnetic stratigraphy in Umbrian pelagic carbonate rocks: The Contessa sections, Gubbio. Geol. Soc. Amer. Bull. 93, 414–432.
Martini, E., 1971. Standard Tertiary and Quaternary calcareous nannoplankton zonation, In: Farinacci, A. (Ed.), Proceedings of the 2nd Planktonic Conference, 2, ed. Tecnoscienza, Roma, pp. 739–785.
McFadden, P.L., McElhinny, M.W., 1990. Classification of the reversal test in palaeomagnetism. Geophys. J. Int. 103, 725–729.
McKenna, M.C., 1980. Eocene paleolatitude, climate, and mammals of Ellesmere Island. Palaeogeogr. Palaeoclimatol. Palaeoecol. 30, 349–362.
Miller, K.G., Wright, J.D., Browning, J.V., 2005. Visions of ice sheets in a greenhouse world. Mar. Geol. 217, 215–231.
Monechi, S., Thierstein, H.R., 1985. Late Cretaceous–Eocene nannofossil and magnetostratigraphic correlations near Gubbio, Italy. Mar. Micropaleontol. 9, 419–440.
Moran, K., Backman, J., Brinkhuis, H., Clemens, S.C., Cronin, T., Dickens, G.R., Eynaud, F., Gattacceca, J., Jakobsson, M., Jordan, R.W., Kaminski, M., King, J., Koc, N., Krylov, A., Martinez, N., Matthiessen, J., McInroy, D., Moore, T.C., Onodera, J., O'Regan, M., Pälike, H., Rea, B., Rio, D., Sakamoto, T., Smith, D., Stein, R., St John, K., Suto, I., Suzuki, N., Takahashi, K., Watanabe, N., Yamamoto, M., Farrell, J., Frank, M., Kubik, P., Jokat, W., Kristoffersen, Y., 2006. The Cenozoic palaeoenvironment of the Arctic Ocean. Nature 441, 601–605.
Muttoni, G., Garzanti, E., Alfonsi, L., Cirilli, S., Germani, D., Lowrie, W., 2001. Motion of Africa and Adria since the Permian: paleomagnetic and paleoclimatic constraints form northern Libya. Earth Planet. Sci. Lett. 192, 159–174.
Muttoni, G., Kent, D.V., Garzanti, E., Brack, P., Abrahamsen, N., Gaetani, M., 2003. Early Permian Pangea "B" to Late Permian Pangea "A". Earth Planet. Sci. Lett. 215, 379–394.
Muttoni, G., Kent, D.V., Garzanti, E., Brack, P., Abrahamsen, N., Gaetani, M., 2004. Erratum to Early Permian Pangea "B" to Late Permian Pangea "A": [Earth Planet Sci. Lett. 215, 2003, 379–394]. Earth Planet. Sci. Lett. 218, 539–540.
Napoleone, G., Premoli, Silva, I., Heller, F., Cheli, P., Corezzi, S., Fischer, A.G., 1983. Eocene magnetic stratigraphy at Gubbio, Italy, and its implications for Paleogene geochronology. Geol. Soc. Amer. Bull. 94, 181–191.
Okada, H., Bukry, D., 1980. Supplementary modification and introduction of code numbers to the low-latitude coccolith biostratigraphic zonation (Bukry, 1973; 1975). Mar. Micropaleontol. 5, 321–325.
Perch-Nielsen, K., 1985. Cenozoic calcareous nannofossils. In: Bolli, H.M., et al. (Ed.), Plankton Stratigraphy. Cambridge University Press, New York, pp. 427–554.
Raffi, I., Backman, J., Pälike, H., 2005. Changes in calcareous nannofossil assemblage across the Paleocene/Eocene transition from the paleo-equatorial Pacific Ocean. Palaeogeogr. Palaeoclimatol. Palaeoecol. 226, 93–126.
Raffi, I., Backman, J., Fornaciari, E., Pälike, H., Rio, D., Lourens, L.J., Hilgen, F.J., 2006. A review of calcareous nannofossil astrobiochronology encompassing the past 25 Million years. Quat. Sci. Rev. 25, 3113–3137.
Rio, D., Raffi, I., Villa, G., 1990. Pliocene–Pleistocene calcareous nannofossil distribution patterns in the western Mediterranean. Proc. Ocean Drill. Prog. Sci. Results 107, 513–533.
Rosenbaum, G., Lister, G.S., Duboz, C., 2004. The Mesozoic and Cenozoic motion of Adria (central Mediterranean): a review of constraints and limitations. Geodin. Acta 17 (2), 125–139.
Singer, M.J., Verosub, K.L., Fine, P., TenPas, J., 1996. A conceptual model for the enhancement of magnetic susceptibility in soils. Quat. Int. 34–36, 243–248.
Sloan, L.C., Rea, D.K., 1995. Atmospheric carbon dioxide and early Eocene climate: a general circulation modeling sensitivity study. Palaeogeogr. Palaeoclimatol. Palaeoecol. 119 (3–4), 275–292.
Stefani, C., Grandesso, P., 1991. Studio preliminare di due sezioni del Flysch Bellunese. Rend. Soc. Geol. Ital. 14, 157–162.
Tauxe, L., Kent, D.V., 1984. Properties of detrital remanence carried by hematite from study of modern river deposits and laboratory redeposition experiments. Geophys. J. R. Astron. Soc. 76, 543–561.
Tauxe, L., Kodama, K.P., Kent, D.V., 2008. Testing corrections for paleomagnetic inclination error in sedimentary rocks: a comparative approach. Phys. Earth Planet. Int. 169, 152–165.
Walker, J.C.G., Hays, P.B., 1981. A negative feedback mechanism for the long-term stabilization of the Earth's surfaces temperature. J. Geophys. 86, 9776–9782.
Watson, G., 1983. Large sample theory of the Langevin distributions. J. Stat. Plan. Inference 8, 245–256.
Wilson, M.J., 2004. Weathering of the primary rock-forming minerals: processes, products and rates. Clay Miner. 39, 233–266.
Winterer, E.L., Bosellini, A., 1981. Subsidence and sedimentation on Jurassic passive continental margin, Southern Alps, Italy. Am. Assoc. Pet. Geol. Bull. 65, 394–421.
Wise, S.W., Breza, J.R., Harwood, D.M., Wei, W., 1991. Palaeogene glacial history of Antarctica. In: Mã œ llerIII III, D.W., McKenzie, J.A., Weissert, H. (Eds.), Controversies in Modern Geology: Evolution of Geological Theories in Sedimentology, Earth History and Tectonics. Academic Press, London, pp. 133–171.
Wolfe, J.A., 1980. Tertiary climates and floristic relationships at High latitudes in the northern hemisphere. Palaeogeogr. Palaeoclimatol. Palaeoecol. 30, 313–323.
Zachos, J.C., Stott, L.D., Lohmann, K.C., 1994. Evolution of marine temperatures during the Paleogene. Paleoceanography 9, 353–387.
Zachos, J., Pagani, M., Sloan, L., Thomas, E., Billups, K., 2001. Trends, rhythms and aberrations in global climate 65 Ma to present. Science 292, 686–693.
Zijderveld, J.D.A., 1967. A.C. demagnetization of rocks: analysis of results. In: Collinson, D.W., et al. (Ed.), Methods in Paleomagnetism. Elsevier, Amsterdam, pp. 254–286.

Appendix 4

Cicogna section							Site 1262 (Agnini et al., 2007)	BKSA95 (Berggren et al., 1995)
Event	Nanno Zones		Stratigraphic position		Chron % from top	CK95		
	NP	CP	Position (m)	Err (m)		Age (Ma)	Age (Ma)	Age (Ma)
C23r base			**77,94**	-	-	-	-	-
Discoaster lodoensis LCO			71,10	0,10	0,936	52,64	52,26	-
Chiprhagmalithus LCO			71,10	0,10	0,936	52,64	-	-
C24n.1n base			**70,64**	-	-	-	-	-
C24n.1r base			**68,80**	-	-	-	-	-
C24n.2n base			**68,21**	-	-	-	-	-
Chiprhagmalithus LO			66,50	0,50	0,473	52,85	-	-
C24n.2r base			**64,60**	0,55	-	-	-	-
Girgisia gammation LO			61,20	0,10	0,526	53,14	52,80	-
Discoaster lodoensis LO	NP12	CP10	60,40	0,10	0,650	53,19	53,11	52,85
Discoaster multiradiatus HO			60,20	0,10	0,681	53,21	53,11	-
C24n.3n base			**58,14**	-	-	-	-	-
Discoaster multiradiatus HCO			51,50	0,10	0,141	53,71	-	-
Sphenolithus radians LO			51,30	0,10	0,145	53,72	53,53	-
Tribrachiatus orthostylus LO			51,30	0,10	0,145	53,72	53,67	53,64
Tribrachiatus contortus HO	NP11	CP9b	52,70	0,10	0,115	53,64	53,49	53,61
Tribrachiatus bramlettei HO			48,50	0,50	0,204	53,87	53,71	53,89
Tribrachiatus contortus LO		CP9a	45,50	0,50	0,268	54,03	54,00	53,93
Discoaster diastypus LO		CP9a	42,70	0,10	0,327	54,18	54,13	-
Tribrachiatus bramlettei LO			35,58	0,55	0,478	54,57	54,53	55,00
Fasciculithus HO			34,73	0,13	0,496	54,61	54,71	-
Rhomboaster HO /CNET HO			32,52	0,48	0,54	54,73	-	-
Fasciculithus / Zygrhablithus CO			31,60	0,10	0,562	54,78	54,98	-
Tribrachiatus bramlettei LRO	NP10		29,43	0,18	0,608	54,90	54,99	-
Rhomboaster LO / CNET LO	NP9b	CP8b	28,88	0,03	0,620	54,93	54,99	55,16
P/E boundary			28,73	0,03	0,623	54,94	-	-
Fasciculithus decrease in diversity			28,73	0,03	0,623	54,94	55,00	-
Ericsonia robusta HO			11,2	0,2	0,994	55,89	55,91	-
C24r base			**10,93**	-	-	-	-	-
Discoaster multiradiatus LO	NP9a		9,90	0,10	0,147	55,98	56,01	56,20
Discoaster delicatus LO			6,86	0,12	0,583	56,19	56,21	-
Zygrhablithus bijugatus LCO			5,63	0,52	0,760	56,27	-	-
Ericsonia robusta LO			3,97	0,07	0,998	56,39	56,29	-
C25n base			**3,96**	-	-	-	-	-
Discoaster nobilis gr. LO		CP7	2,14	0,05	C25r	56,52	56,24	56,90
Zygrhablithus bijugatus LO			1,58	0,51	C25r	-	-	-

Table A1. List of late Paleocene–early Eocene biostratigraphic and magnetostratigraphic events from the Cicogna section (this work), ODP Site 1262 (Agnini et al., 2007), and the BKSA95 time scale (Berggren et al., 1995). NP and CP columns indicate biohorizons used to define the base of nannofossil zones in the standard zonations of Martini (1971) (modified after Aubry et al., 2000) and Okada and Bukry (1980). The position of the biohorizons at Cicogna are expressed in meters from the section base. Chron % notation indicates the position of biohorizons relative to the magnetochron they were found in, expressed as decimals from 0 (magnetochron top) to 1 (magnetochron base). CK95: Age of biostratigraphic and magnetostratigraphic events expressed in millions of years based on the Cande and Kent (1995) time scale.

Table A2. List of the magnetic characteristic components derived by the analyses of the samples

Least square analysis of the samples from Cicogna
LAT: 46.06 LON: 12.24
Comp= component (Ch)
Samp.= sample
Pos= stratigraphic position (cm)
N= number of used vector-end points (A= anchored; F= free)
MAD= mean angular deviation
CDECL= declination in sample coordinates
CINCL= inclination in sample coordinates
GDECL= declination in "in situ" coordinates
GINCL= inclination in "in situ" coordinates
BDECL= declination in "tilt corrected" coordinates
BINCL= inclination in "tilt corrected" coordinates
TREATS= minimum and maximum temperature range of the C component
J = 10e-2 A/m
All samples are ~10 cc in volume

Samp.	Pos.	comp	N	MAD	CDECL	CINCL	GDECL	GINCL	BDECL	BINCL	TREATS		Jcomp
cic1	5.0	C	9 A	8.0	277.4	-59.0	197.7	-57.7	167.9	-25.3	250.0	500.0	00.0197
cic2	20.0	C	9 F	16.8	15.2	-73.5	216.1	-42.8	188.5	-23.2	250.0	500.0	00.0147
cic3	62.5	C	9 F	17.0	125.0	-72.1	175.7	-60.8	156.0	-21.4	200.0	475.0	00.0132
cic4	105.5	C	10 A	5.4	314.4	-65.4	185.7	-62.9	159.3	-25.6	250.0	525.0	00.0298
cic5	116.0	C	11 F	15.6	307.3	-48.6	213.4	-54.1	177.7	-29.2	300.0	570.0	00.0186
cic6	121.5	C	13 F	18.7	10.0	-39.0	229.7	-64.5	172.1	-41.6	300.0	600.0	00.0228
cic7	140.0	C	7 A	14.1	8.6	-55.7	216.4	-62.6	170.7	-35.5	250.0	475.0	00.0106
cic8	155.0	C	8 A	14.0	20.3	-64.0	219.0	-58.5	175.7	-34.3	250.0	475.0	00.0183
cic10	200.0	C	9 A	10.9	306.5	-38.8	234.7	-50.0	190.5	-37.7	300.0	550.0	00.0165
cic12	236.0	C	8 A	15.9	46.5	-66.1	176.7	-66.1	153.7	-26.1	300.0	550.0	00.0137
cic13	273.0	C	9 A	11.4	28.9	-49.2	144.2	-70.7	139.6	-26.8	250.0	500.0	00.0102
cic16	358.0	C	7 F	17.7	300.9	-63.6	250.5	-54.9	189.5	-48.6	250.0	475.0	00.0089
cic20	433.0	C	7 A	12.2	240.4	80.9	15.4	53.8	349.6	21.5	200.0	450.0	00.0069
cic21	455.0	C	10 A	7.1	241.2	63.0	338.4	59.4	328.2	16.9	300.0	550.0	00.0187
cic22	472.0	C	5 A	3.2	289.5	75.3	13.8	39.5	357.8	9.5	320.0	450.0	00.0082
cic24	499.0	C	6 A	7.9	146.6	66.7	49.5	58.4	359.2	39.0	250.0	425.0	00.0067
cic26	521.0	C	4 A	7.2	230.6	73.7	22.2	44.2	359.9	17.0	300.0	400.0	00.0061
cic27	526.0	C	5 A	17.2	104.5	65.2	50.8	47.3	11.6	34.1	300.0	450.0	00.0111
cic34	615.0	C	7 A	5.5	48.0	73.4	12.5	37.6	358.1	7.4	400.0	550.0	00.0105
cic36	652.0	C	6 A	8.7	239.2	69.9	326.8	53.8	322.9	10.2	250.0	450.0	00.0130
cic37	657.0	C	13 A	6.2	98.4	81.3	41.0	44.6	9.5	27.0	300.0	600.0	00.0222
cic39	698.0	C	5 F	17.0	45.4	59.9	43.2	20.4	30.0	12.0	200.0	400.0	00.0061
cic41	731.0	C	5 A	12.4	272.2	2.7	276.3	1.1	267.6	-30.8	250.0	400.0	00.0093
cic42	743.0	C	5 A	7.6	257.6	-63.7	230.6	-52.0	186.7	-36.5	320.0	450.0	00.0104
cic43	747.0	C	9 A	11.5	285.6	-31.1	260.1	-34.4	221.4	-46.1	250.0	525.0	00.0176
cic46	788.0	C	6 F	11.0	315.9	-28.4	266.6	-49.1	202.9	-56.6	300.0	450.0	00.0108
cic48	825.0	C	6 F	8.6	316.5	-5.5	271.6	-38.0	224.0	-55.8	250.0	425.0	00.0225
cic49	850.0	C	6 A	7.2	142.3	50.8	34.3	62.4	350.2	34.5	400.0	525.0	00.0119
cic50	864.0	C	9 A	5.6	65.7	67.0	10.2	50.9	348.9	17.3	250.0	475.0	00.0233
cic52	897.0	C	7 A	11.8	73.1	54.1	7.0	44.7	350.6	10.9	325.0	525.0	00.0063
cic53	921.0	C	5 A	13.2	118.3	48.5	35.2	53.3	359.2	29.6	450.0	550.0	00.0113
cic56	958.0	C	11 A	9.3	321.1	-58.1	214.0	-66.7	165.7	-36.8	300.0	550.0	00.0195
cic59	1008.0	C	12 A	5.3	134.6	48.2	23.5	58.3	350.0	27.8	325.0	600.0	00.0193
cic60	1023.0	C	4 A	8.5	118.7	48.5	56.4	54.4	6.1	40.7	300.0	450.0	00.0138
cic61	1056.0	C	10 A	5.8	91.9	76.8	345.0	56.1	332.7	14.8	250.0	500.0	00.0166
cic62	1064.0	C	10 A	8.3	186.5	66.9	321.6	69.8	318.7	25.9	200.0	575.0	00.0327
cic63	1084.0	C	5 A	6.0	116.5	44.7	40.9	44.9	9.2	27.1	325.0	425.0	00.0088
cic65	1101.0	C	6 A	9.4	302.8	-26.7	251.7	-38.3	211.6	-42.5	325.0	450.0	00.0094
cic67	1171.0	C	13 A	11.1	342.2	-31.1	252.0	-73.0	161.6	-50.7	300.0	600.0	00.0190
cic68	1181.0	C	8 A	7.6	320.6	-30.9	230.3	-56.9	181.2	-38.7	400.0	600.0	00.0187
cic69	1226.0	C	10 A	10.4	336.8	-50.5	170.7	-63.2	152.6	-22.4	325.0	575.0	00.0131
cic70	1235.0	C	9 A	6.7	305.6	-35.6	207.8	-48.2	179.9	-22.6	250.0	525.0	00.0336
cic71	1279.0	C	12 A	7.4	264.2	-54.0	206.4	-43.4	182.8	-18.5	300.0	575.0	00.0205
cic72	1286.0	C	9 A	7.9	260.6	-53.7	218.1	-40.5	191.4	-22.7	425.0	650.0	00.0162
cic73	1308.0	C	9 A	11.8	262.5	-52.7	211.7	-43.4	185.7	-21.2	325.0	550.0	00.0092
cic74	1325.0	C	4 F	9.0	286.4	-19.1	216.6	-24.4	202.7	-10.7	425.0	500.0	00.0064
cic75	1355.0	C	9 F	14.5	275.1	-39.0	223.9	-37.9	196.8	-24.4	325.0	575.0	00.0158
cic76	1381.0	C	6 A	8.1	266.9	-57.9	184.4	-44.0	169.4	-9.3	250.0	500.0	00.0190
cic77	1391.0	C	9 A	9.3	297.7	-65.8	216.5	-66.5	166.5	-37.6	300.0	500.0	00.0184
cic78	1421.0	C	15 F	10.6	320.5	-14.6	217.9	-48.1	185.0	-27.6	200.0	670.0	00.0435

cic79	1428.0	C	13 A	5.4	280.8	-51.5	203.9	-45.0	180.2	-18.5	300.0	600.0	00.0253
cic80	1455.0	C	14 A	2.6	275.5	-46.9	225.9	-40.9	195.4	-27.5	200.0	625.0	00.1246
cic81	1496.0	C	14 A	5.5	322.6	-46.5	220.5	-60.3	174.4	-35.9	300.0	650.0	00.0358
cic82	1531.0	C	5 A	3.6	311.3	-55.4	233.7	-64.8	172.5	-43.3	200.0	400.0	00.0262
cic83	1561.0	C	14 A	5.4	281.2	-67.5	187.9	-44.9	171.0	-11.4	300.0	625.0	00.0450
cic84	1581.0	C	7 A	5.6	293.8	-51.4	203.6	-43.4	181.2	-17.2	350.0	550.0	00.0219
cic85	1627.0	C	10 A	5.2	284.4	-65.4	207.9	-52.1	176.9	-25.4	350.0	600.0	00.0338
cic86	1635.0	C	10 A	6.5	295.6	-49.1	210.5	-53.0	177.4	-27.1	400.0	670.0	00.0317
cic87	1666.0	C	9 A	14.1	288.5	-41.8	214.3	-37.1	191.9	-18.3	300.0	500.0	00.0133
cic91b	1784.0	C	4 A	11.9	324.8	-27.3	266.6	-58.3	186.0	-57.7	350.0	450.0	00.0056
cic92	1808.0	C	8 A	4.8	285.2	-60.0	206.1	-51.1	176.9	-23.8	200.0	425.0	00.0217
cic94	1881.0	C	8 F	9.3	279.0	-31.1	215.2	-30.7	197.2	-14.2	250.0	525.0	00.0145
cic95	1901.0	C	9 A	8.7	298.0	-54.1	232.2	-58.8	179.5	-40.4	400.0	600.0	00.0246
cic96	1951.0	C	12 A	7.5	285.7	-41.3	221.5	-35.5	197.4	-21.4	250.0	600.0	00.0220
cic97	1989.0	C	14 A	2.2	306.4	-56.6	221.6	-63.6	171.1	-38.0	300.0	625.0	00.3248
cic98	2001.0	C	8 A	3.7	322.0	-32.1	255.1	-50.9	196.5	-49.9	475.0	650.0	00.0645
cic99	2021.0	C	10 A	4.1	121.7	49.3	27.5	56.3	353.3	28.0	425.0	650.0	00.0847
cic100	2086.0	C	5 A	4.4	125.4	73.8	33.4	72.0	339.8	39.3	525.0	625.0	00.1277
cic101	2171.0	C	12 A	8.8	127.3	78.5	11.4	74.2	332.7	35.6	300.0	575.0	00.0624
cic102	2191.0	C	5 A	3.9	48.6	74.8	0.2	45.6	346.0	9.3	525.0	625.0	00.0974
cic103	2228.0	C	7 A	3.2	311.9	-26.5	217.9	-48.2	184.9	-27.6	475.0	625.0	00.2007
cic104	2251.0	C	7 A	2.0	314.8	-29.2	225.9	-50.7	186.1	-33.3	500.0	650.0	00.2407
cic105	2281.0	C	4 A	8.1	62.3	57.4	42.5	50.5	4.9	31.4	525.0	600.0	00.0357
cic106	2303.0	C	7 A	2.4	218.9	-73.0	155.4	-59.8	146.5	-16.9	500.0	650.0	00.1159
cic108	2376.0	C	9 A	5.6	305.4	-43.9	205.2	-51.1	176.4	-23.4	500.0	680.0	00.0470
cic109	2391.0	C	8 A	8.5	303.3	-57.3	200.7	-57.7	169.2	-26.4	475.0	650.0	00.0225
cic111	2471.0	C	6 A	2.5	245.0	-68.0	198.3	-50.7	173.3	-20.3	500.0	625.0	00.1060
cic112	2556.0	C	8 A	7.2	280.2	-80.4	160.8	-55.6	150.5	-13.5	500.0	670.0	00.0363
cic113	2561.0	C	6 A	1.6	278.6	-80.3	186.3	-60.0	161.3	-23.4	500.0	625.0	00.1278
cic114	2581.0	C	12 A	2.8	280.4	-75.3	195.0	-62.0	163.6	-27.6	400.0	670.0	00.0782
cic115	2582.0	C	7 A	2.1	298.6	-67.6	199.3	-59.5	167.2	-27.2	500.0	650.0	00.1668
cic117	2633.0	C	12 A	3.0	158.3	51.9	100.0	74.0	334.9	57.6	250.0	600.0	00.2756
cic118	2661.0	C	6 A	3.4	275.8	-49.4	213.9	-45.7	185.0	-23.9	500.0	625.0	00.0794
cic119	2696.0	C	16 A	3.6	244.3	-65.5	227.3	-32.9	202.9	-23.3	200.0	670.0	00.0984
cic120	2736.0	C	6 A	11.8	289.8	-45.9	197.0	-41.0	178.9	-12.2	425.0	550.0	00.0184
cic121	2743.0	C	14 A	3.9	285.6	-48.6	218.4	-49.2	184.2	-28.5	250.0	670.0	00.0477
cic122	2783.0	C	9 A	7.3	280.8	-56.6	195.1	-52.7	170.3	-20.5	300.0	500.0	00.0213
cic123	2791.0	C	11 A	5.9	306.6	-46.6	215.0	-56.3	176.3	-31.2	400.0	650.0	00.0405
cic124	2816.0	C	8 A	7.8	275.0	-34.7	234.8	-33.1	207.2	-28.2	350.0	620.0	00.0262
cic125	2831.0	C	11 F	14.6	285.1	-17.9	227.7	-23.0	211.0	-16.9	400.0	670.0	00.0216
cic127	2871.0	C	5 F	6.3	301.4	-42.8	236.3	-50.2	190.9	-38.7	250.0	425.0	00.0065
cic129	3156.0	C	14 A	3.3	307.6	-24.3	220.8	-41.0	192.5	-24.6	200.0	670.0	00.0434
cic130	3165.0	C	8 F	6.7	338.5	-28.4	270.6	-60.7	181.2	-59.5	300.0	640.0	00.0312
cic131	3196.0	C	6 A	6.0	334.5	-9.1	279.0	-31.3	240.2	-57.4	400.0	525.0	00.0128
cic132	3206.0	C	7 F	9.2	357.5	-47.3	318.6	-78.3	136.4	-57.7	250.0	500.0	00.0171
cic133	3214.0	C	13 A	7.5	319.8	-7.3	250.6	-29.3	220.7	-36.6	300.0	650.0	00.0426
cic134	3243.0	C	10 F	8.3	336.0	-24.8	252.1	-51.8	194.4	-48.5	300.0	600.0	00.0318
cic135	3261.0	C	10 F	10.6	348.7	-18.4	271.0	-59.9	182.7	-59.9	200.0	525.0	00.0125
cic139	3291.0	C	13 A	3.8	291.3	-27.4	207.1	-32.4	190.8	-10.8	250.0	670.0	00.0460
cic140	3306.0	C	9 F	10.2	293.0	-44.4	169.4	-47.6	158.4	-7.8	250.0	550.0	00.0347
cic141	3313.0	C	15 A	4.3	330.3	-3.5	244.7	-28.2	217.7	-31.8	200.0	650.0	00.0602
cic142	3331.0	C	9 A	6.8	341.2	-34.2	244.0	-65.4	173.1	-47.7	400.0	620.0	00.0314
cic145	3411.0	C	7 A	8.3	345.1	-10.3	273.8	-42.9	217.0	-59.4	400.0	575.0	00.0167
cic147	3451.0	C	11 A	4.5	291.0	-44.1	207.4	-47.9	180.0	-22.2	350.0	640.0	00.0941
cic148	3487.0	C	5 A	11.0	314.6	0.9	216.0	-23.6	202.8	-9.6	525.0	650.0	00.0121
cic149	3514.0	C	6 A	4.2	280.8	-47.8	168.5	-41.4	160.1	-1.8	525.0	640.0	00.0470
cic152	3541.0	C	6 A	5.1	146.5	13.4	15.3	51.9	350.9	20.0	500.0	620.0	00.0590
cic153	3617.0	C	6 A	9.0	255.2	-65.0	180.5	-45.3	165.3	-7.2	525.0	650.0	00.0429
cic155	3649.0	C	6 A	5.9	330.1	-89.3	156.5	-55.6	147.1	-10.3	500.0	625.0	00.0438
cic156	3670.0	C	6 A	5.9	155.7	41.6	67.1	57.3	1.3	46.3	475.0	600.0	00.0811
cic157	3680.0	C	8 A	2.2	81.5	16.7	42.1	11.5	34.5	5.8	425.0	600.0	00.0771
cic158	3695.0	C	6 A	15.7	312.6	-5.3	235.6	-24.0	213.4	-23.6	525.0	640.0	00.0229
cic159	3702.0	C	5 A	2.1	315.1	-27.0	209.1	-46.8	179.9	-21.1	550.0	650.0	00.1375
cic160	3713.0	C	6 A	4.3	348.3	-54.9	208.7	-82.8	143.9	-40.6	525.0	640.0	00.0627
cic162	3759.0	C	7 A	3.7	143.7	47.6	50.2	65.4	347.8	40.4	500.0	640.0	00.1482
cic165	3780.0	A	6 A	4.8	287.9	-26.9	220.8	-32.0	198.0	-18.4	525.0	640.0	00.1018
cic166	3815.0	C	6 A	2.0	300.9	-38.3	195.7	-47.6	172.5	-15.3	525.0	650.0	00.1629
cic167	3831.0	C	5 A	3.1	314.9	-25.1	216.9	-49.3	181.2	-26.8	525.0	620.0	00.1642
cic168	3841.0	C	6 A	3.6	286.2	-31.0	208.0	-34.0	189.1	-11.9	500.0	625.0	00.0649
cic173	3927.0	C	8 A	3.2	319.4	-9.2	252.5	-32.2	215.6	-40.6	300.0	550.0	00.1117
cic174	3934.0	C	5 A	6.1	298.8	-28.2	226.8	-38.6	195.6	-26.4	525.0	625.0	00.0348
cic175	3944.0	C	4 A	11.0	5.0	22.8	256.7	-18.1	232.9	-35.3	475.0	550.0	00.0153
cic176	3959.0	C	5 A	11.3	322.8	-39.3	186.7	-52.5	164.6	-15.4	550.0	650.0	00.0389
cic177	3983.0	C	7 A	3.4	151.5	58.4	54.2	71.6	340.2	43.2	450.0	600.0	00.1306

cic178	3986.0	C	6 A	4.5	259.6	-68.9	155.2	-62.2	144.6	-16.4	525.0	650.0	00.1041
cic179	4005.0	C	5 A	8.1	41.7	-74.5	44.0	-78.0	118.6	-42.0	550.0	640.0	00.0267
cic180	4044.0	C	10 A	3.2	159.3	55.8	70.8	63.2	353.0	48.9	400.0	670.0	00.2091
cic181	4046.0	C	7 A	4.2	147.0	55.9	92.7	64.5	348.0	58.1	400.0	600.0	00.1643
cic182	4075.0	C	4 A	3.0	262.1	-43.9	200.0	-30.7	186.4	-4.8	550.0	625.0	00.1235
cic183	4100.0	C	6 F	2.0	318.2	-36.5	185.2	-57.5	160.8	-18.9	525.0	640.0	00.2507
cic184	4113.0	C	6 A	2.1	320.9	-24.3	214.0	-52.2	177.3	-27.0	500.0	625.0	00.2266
cic185	4187.0	C	12 A	6.6	348.8	-6.6	250.9	-45.6	198.4	-45.3	300.0	640.0	00.0795
cic186	4232.0	C	8 A	8.0	115.1	59.4	346.0	59.5	330.8	15.6	425.0	600.0	00.1598
cic187	4245.0	C	7 A	2.1	325.9	-16.7	210.4	-48.7	178.9	-23.0	500.0	640.0	00.1651
cic188	4260.0	C	8 F	4.4	346.3	-10.4	260.1	-36.6	214.5	-48.2	300.0	525.0	00.1498
cic190	4288.0	C	7 A	6.4	296.7	-69.3	155.3	-68.5	142.9	-22.5	475.0	620.0	00.0741
cic191	4313.0	C	13 A	2.8	309.3	-36.4	213.2	-51.0	178.1	-25.9	250.0	625.0	00.4335
cic192	4347.0	C	12 A	2.3	313.3	-37.4	181.8	-54.4	161.1	-15.2	250.0	620.0	00.6433
cic193	4389.0	C	9 A	1.7	338.7	-27.9	219.7	-62.5	169.0	-35.1	475.0	670.0	00.2911
cic194	4424.0	C	5 A	2.9	326.6	-42.2	214.1	-58.6	171.4	-30.7	525.0	620.0	00.1611
cic195	4483.0	C	4 A	1.7	326.2	-41.2	199.6	-57.1	167.3	-23.7	550.0	625.0	00.2942
cic196	4513.0	C	5 A	2.0	270.0	-56.0	212.8	-48.7	180.0	-24.3	525.0	640.0	00.2576
cic197	4612.0	C	6 A	1.5	313.5	-52.3	171.8	-63.0	151.7	-20.0	525.0	650.0	00.4000
cic199	4733.0	C	7 A	5.9	179.1	55.3	86.4	77.3	330.0	50.5	475.0	625.0	00.0931
cic202	4812.0	C	4 A	5.3	251.5	63.1	284.2	60.8	299.9	16.8	550.0	620.0	00.0471
cic203	4944.0	C	6 A	1.7	330.1	-30.2	183.3	-63.2	156.3	-23.0	525.0	650.0	00.2105
cic204	5000.0	C	7 A	3.7	269.5	-45.5	199.9	-42.8	178.1	-13.7	500.0	640.0	00.1173
cic205	5040.0	C	4 A	12.9	318.0	-19.9	207.1	-49.7	176.5	-22.1	550.0	625.0	00.0206
cic206	5087.0	C	6 A	3.2	318.2	-49.1	174.4	-61.6	153.6	-19.3	525.0	640.0	00.0861
cic210	5343.0	C	7 A	4.5	250.2	-54.3	218.2	-45.4	185.4	-25.2	500.0	640.0	00.0502
cic211	5560.0	C	7 A	2.8	301.1	-33.3	204.8	-43.9	180.0	-17.0	500.0	650.0	00.0596
cic212	5586.0	C	6 A	7.3	323.4	-38.8	224.6	-50.8	182.9	-31.8	525.0	640.0	00.0240
cic213	5597.0	C	7 A	2.9	304.9	-15.4	202.8	-37.0	183.8	-11.0	500.0	650.0	00.0711
cic214	5690.0	C	9 A	7.6	292.7	-25.8	220.6	-33.7	196.5	-19.4	450.0	670.0	00.0190
cic215	5710.0	C	4 A	7.9	296.9	-6.2	231.9	-21.2	213.5	-19.3	525.0	600.0	00.0131
cic216	5774.0	C	9 A	11.1	281.9	-46.7	206.1	-44.5	180.2	-18.1	300.0	575.0	00.0141
cic218	5810.0	C	9 A	4.5	215.6	36.4	187.7	56.7	266.3	54.4	250.0	550.0	00.0187
cic219	5853.0	C	9 A	6.3	134.3	49.9	49.4	60.1	354.2	38.3	450.0	650.0	00.0266
cic220	5877.0	C	7 F	17.8	64.5	61.4	351.3	48.2	338.4	6.7	425.0	600.0	00.0122
cic221	5911.0	C	8 F	19.1	105.6	49.1	7.3	47.9	347.8	11.9	400.0	575.0	00.0089
cic222	5930.0	C	8 F	12.6	106.6	63.8	6.7	60.1	339.8	21.4	450.0	625.0	00.0216
cic223	5933.0	C	7 F	14.6	102.1	47.3	15.0	48.4	351.5	15.5	400.0	575.0	00.0159
cic224	5969.0	C	10 A	3.4	113.9	49.9	346.9	53.6	333.5	10.4	400.0	650.0	00.0329
cic225	5988.0	C	11 A	3.0	127.5	62.8	28.7	68.4	340.1	34.0	250.0	600.0	00.0518
cic226	6012.0	C	7 A	10.6	137.0	66.8	333.3	67.4	322.4	21.3	450.0	625.0	00.0201
cic227	6028.0	C	6 F	23.5	110.3	58.0	13.7	56.6	345.2	21.1	425.0	550.0	00.0080
cic228	6037.0	C	7 A	10.7	140.7	71.3	26.6	53.0	353.6	24.0	450.0	650.0	00.0123
cic229	6070.0	C	10 F	9.8	190.2	79.4	347.0	61.4	330.4	17.5	400.0	625.0	00.0237
cic230	6103.0	C	8 F	12.6	207.0	53.6	333.8	67.3	322.6	21.2	425.0	600.0	00.0202
cic231	6111.0	C	11 A	2.1	201.0	82.6	7.5	52.8	344.8	16.0	425.0	670.0	00.0690
cic232	6130.0	C	9 A	3.3	221.1	75.3	5.3	61.6	338.2	22.3	425.0	625.0	00.0590
cic233	6144.0	C	10 F	6.4	237.8	60.7	322.1	53.2	319.2	6.4	400.0	625.0	00.0463
cic234	6152.0	C	10 A	5.4	132.0	64.0	19.2	42.9	357.7	13.4	425.0	650.0	00.0496
cic235	6155.0	C	9 A	4.6	137.4	55.8	44.1	52.9	0.6	32.5	300.0	550.0	00.0235
cic237	6190.0	C	9 A	3.0	133.4	51.0	44.0	49.0	4.5	30.5	300.0	550.0	00.0336
cic238	6210.0	C	8 F	8.1	146.8	49.1	18.7	52.2	350.7	20.0	450.0	625.0	00.0296
cic240	6234.0	C	9 A	7.3	163.8	40.4	39.2	69.6	341.0	37.8	425.0	625.0	00.0199
cic242	6250.0	C	8 A	5.9	110.0	64.1	7.1	61.4	339.1	22.7	425.0	600.0	00.0392
cic243	6276.0	C	7 F	11.2	122.1	57.5	42.6	62.6	349.6	36.3	450.0	600.0	00.0165
cic245	6303.0	C	10 A	4.8	132.1	63.3	1.2	61.5	336.6	20.9	450.0	670.0	00.0411
cic246	6323.0	C	9 A	5.0	121.1	53.5	27.5	56.6	350.9	26.7	450.0	650.0	00.0418
cic247	6336.0	C	6 A	6.5	162.3	78.0	328.9	66.2	320.9	19.7	475.0	600.0	00.0161
cic249	6368.0	C	8 A	6.4	130.3	54.7	356.5	58.9	336.0	17.6	400.0	575.0	00.0159
cic250	6393.0	C	9 F	4.6	95.2	55.1	4.4	46.3	347.0	9.6	425.0	625.0	00.0540
cic251	6410.0	C	6 A	14.0	227.1	18.5	200.0	44.0	249.8	44.0	400.0	525.0	00.0087
cic252	6432.0	C	6 A	7.2	289.4	-16.4	224.2	-25.2	205.5	-16.4	500.0	625.0	00.0453
cic254	6470.0	C	8 A	9.4	196.1	61.8	297.1	66.1	307.3	20.0	400.0	575.0	00.0210
cic255	6499.0	C	8 A	5.9	267.6	-14.2	215.3	-8.8	212.0	0.9	450.0	650.0	00.0215
cic256	6514.0	C	5 A	4.0	141.2	80.4	345.2	62.9	328.9	18.6	525.0	650.0	00.0222
cic257	6527.0	C	9 A	5.6	288.6	-47.9	201.5	-42.5	179.1	-14.3	425.0	625.0	00.0188
cic258	6547.0	C	8 A	4.5	296.2	-17.0	232.5	-30.4	206.0	-25.3	450.0	670.0	00.0267
cic259	6566.0	C	10 A	5.0	288.0	-42.9	197.9	-40.3	178.7	-10.8	425.0	650.0	00.0442
cic260	6585.0	C	8 A	6.5	287.9	-45.2	197.9	-42.2	177.3	-12.2	475.0	650.0	00.0308
cic261	6600.0	C	8 A	5.6	286.0	-51.2	189.8	-41.7	172.9	-8.0	525.0	680.0	00.0308
cic262	6639.0	C	13 A	1.9	315.2	-47.2	196.8	-54.6	168.0	-20.9	300.0	650.0	00.1088
cic263	6657.0	C	6 A	10.0	305.8	-37.4	209.2	-47.1	179.6	-21.4	500.0	625.0	00.0152
cic265	6697.0	C	10 A	6.0	305.9	-10.2	254.1	-35.1	213.2	-43.2	425.0	650.0	00.0259
cic266	6724.0	C	6 A	9.1	300.9	-32.7	215.6	-43.6	185.6	-22.6	525.0	650.0	00.0222

cic267	6749.0	C	11 A	11.0	272.9	-31.4	219.9	-25.7	202.5	-13.7	425.0	670.0	00.0099
cic268	6770.0	C	9 A	7.9	284.0	-27.7	218.7	-28.0	199.9	-14.5	450.0	680.0	00.0210
cic269	6797.0	C	10 A	4.6	319.6	-41.1	236.0	-60.5	175.1	-41.6	450.0	670.0	00.0248
cic272	6844.0	C	7 A	4.9	183.3	69.5	349.9	73.4	325.7	28.9	450.0	600.0	00.0166
cic273	6860.0	C	5 A	7.0	133.7	44.5	7.8	55.9	343.0	18.5	425.0	525.0	00.0097
cic275	6899.0	C	10 A	8.8	310.0	-2.4	251.4	-28.5	219.0	-37.7	400.0	650.0	00.0176
cic276	6928.0	C	10 A	6.7	322.2	-49.4	219.5	-66.4	164.7	-36.7	425.0	650.0	00.0300
cic278	6980.0	C	10 A	4.8	314.9	-34.0	233.5	-48.5	188.7	-35.7	400.0	625.0	00.0351
cic279	7000.0	C	14 A	5.0	334.4	-42.3	231.1	-59.4	175.4	-38.8	300.0	670.0	00.0581
cic280	7022.0	C	11 A	7.2	334.5	-31.5	234.7	-56.9	179.3	-39.8	400.0	670.0	00.0205
cic281	7047.0	C	15 A	4.3	314.9	-33.7	203.3	-50.8	173.9	-21.0	300.0	680.0	00.0563
cic282	7080.0	C	9 A	8.3	173.4	72.1	322.7	69.6	317.8	22.8	400.0	600.0	00.0214
cic283	7122.0	C	7 F	9.1	159.0	49.1	8.4	75.1	329.2	33.2	400.0	575.0	00.0252
cic284	7146.0	C	8 A	6.3	98.2	57.9	20.1	53.1	350.7	21.2	425.0	625.0	00.0172
cic285	7185.0	C	8 F	7.4	138.4	39.8	57.1	56.5	0.3	40.8	400.0	575.0	00.0184
cic288	7257.0	C	5 F	11.1	111.6	25.1	42.8	32.0	19.0	19.9	475.0	575.0	00.0111
cic290	7320.0	C	7 F	11.9	150.4	41.8	358.4	58.2	337.2	17.5	475.0	625.0	00.0165
cic292	7366.0	C	6 A	8.0	122.6	49.1	12.8	52.1	348.0	17.4	425.0	575.0	00.0118
cic293	7382.0	C	7 F	15.7	139.8	35.4	21.9	56.0	349.2	23.9	425.0	575.0	00.0149
cic294	7410.0	C	7 F	16.8	132.5	47.8	355.3	54.4	337.7	13.4	425.0	600.0	00.0151
cic304	7687.0	C	11 A	5.1	130.7	59.1	352.3	53.9	336.4	12.0	400.0	650.0	00.0763
cic306	7757.0	C	7 A	2.4	182.1	82.6	337.5	50.3	329.1	5.4	400.0	600.0	00.0274
cic309	7830.0	C	12 A	6.6	322.4	-2.5	271.7	-47.8	200.6	-59.7	350.0	650.0	00.0827
cic310	7852.0	C	6 A	10.8	290.5	-57.3	222.9	-45.5	187.5	-28.0	400.0	525.0	00.0207
cic311	7880.0	C	14 A	4.6	282.3	-38.6	246.4	-29.7	214.8	-34.8	250.0	650.0	00.0973
cic312	7905.0	C	11 A	7.4	322.8	-3.8	236.3	-40.7	198.2	-33.7	425.0	680.0	00.0463
cic313	7912.0	C	11 A	4.6	317.7	-31.7	205.4	-54.2	172.1	-24.3	300.0	600.0	00.0425
cic315	7957.0	C	5 A	2.6	309.8	-17.4	221.1	-40.9	190.7	-24.2	525.0	625.0	00.1345
cic316	7972.0	C	7 A	4.3	302.2	-28.9	200.9	-42.2	179.1	-13.7	500.0	670.0	00.0909
cic317	7995.0	C	8 A	2.9	337.4	-16.3	226.3	-51.6	182.7	-33.1	500.0	670.0	00.0442
cic318	8020.0	C	6 A	6.0	310.8	-23.7	229.2	-45.7	189.9	-31.8	550.0	650.0	00.0911

Table A3. List of the magnetic susceptibility and magnetization values of the unoriented samples discussed in the paper.

Pos= position
Weight= weight of sample expressed in g
j= intensity of magnetization imparted with fields of 0.1 T and 1.0 T, expressed in E-7 Am^2
IRM 1.0/0.1= ratio of j 1.0T / j 0.1 T
Susc.= magnetic susceptibility, expressed in E-11 m^3

Samp.	pos	weight	j 0.1T	j 1.0T	IRM 1.0/0.1	susc.
cc210	210	3.7903	7.79241	20.8245	2.672408151	23.7
cc230	230	4.3823	8.0994	22.2332	2.745042843	24.64
cc250	250	8.0767	18.0448	43.0601	2.386288571	53.36
cc270	270	5.3543	3.18437	4.41706	1.387106398	22.65
cc290	290	4.2148	4.80215	8.6411	1.799423175	22.11
cc310	310	6.3174	7.95487	17.6946	2.224373246	34.04
cc329	329	2.4262	4.2843	8.5081	1.985878673	14.65
cc350	350	4.3018	6.58478	13.6732	2.076485471	24.27
cc370	370	2.8053	4.31261	8.55531	1.983789399	15.75
cc390	390	6.3486	10.2048	22.2174	2.177151929	36.39
cc410	410	4.8559	7.37309	14.5455	1.972782104	27.61
cc430	430	4.2610	2.44449	3.84167	1.571562985	19.1
cc450	450	5.2068	4.96037	9.46146	1.907410133	26.94
cc470	470	4.4466	5.59025	11.0484	1.976369572	27.48
cc510	510	5.1676	4.0438	7.78107	1.924197537	26.33
cc530	530	2.9151	1.78413	2.40937	1.350445315	13.44
cc550	550	4.6213	7.09824	17.9937	2.534952326	27.19
cc570	570	5.0950	13.2222	30.3479	2.295223185	36.69
cc590	590	5.9653	16.6216	50.926	3.063844636	46.03
cc610	610	4.4804	9.38378	21.2343	2.262872744	31.1
cc630	630	6.1515	7.6096	22.7024	2.983389403	33.67
cc650	650	4.1355	9.42385	23.3866	2.48163967	24.98
cc670	670	5.1065	15.9019	45.5449	2.864116867	36.36
cc690	690	7.2134	6.00804	11.1494	1.855746633	31.05
cc710	710	4.8025	10.0926	19.9436	1.976061669	27.24
cc730	730	6.1100	7.09872	18.2464	2.570378885	27.93
cc750	750	5.1803	6.12468	15.7123	2.565407499	25.92
cc770	770	1.8117	1.42657	1.84084	1.290395845	11.41
cc790	790	6.3337	8.30199	24.7015	2.975370965	30.45
cc810	810	2.9408	5.61776	13.533	2.408967275	19.08
cc830	830	3.0393	14.1861	38.4828	2.712711739	29.43
cc850	850	8.4441	4.96495	10.7801	2.171240395	33.18
cc870	870	2.0164	4.10352	9.15357	2.230662943	12.62
cc890	890	4.9147	2.97137	6.38698	2.149506793	19.21
cc910	910	4.1766	8.53161	24.2313	2.840179052	25.78
cc930	930	3.8376	2.55607	5.08267	1.988470582	15.75
cc950	950	2.9889	7.53275	19.007	2.523248482	22.33
cc970	970	5.4812	6.67543	17.4182	2.609300075	26.67
cc990	990	4.3927	2.62607	4.96089	1.889092827	18.12
cc1020	1020	8.8658	7.79509	22.8793	2.935091192	43.44
cc1040	1040	3.2951	1.87044	3.19464	1.707961763	13.58
cc1060	1060	3.8013	2.53308	4.6096	1.819760923	17.25
cc1080	1080	5.4404	4.61881	7.92791	1.716439949	25.46
cc1100	1100	5.1796	5.02418	14.5041	2.886859149	25.28
cc1120	1120	5.5811	6.30334	12.1801	1.932324768	29.06
cc1140	1140	6.5348	3.68557	5.73707	1.556630318	28.34
cc1160	1160	6.3633	5.92527	9.08226	1.532801037	31.6
cc1180	1180	3.8673	3.46255	5.79683	1.674150554	20.63
cc1200	1200	6.161	5.17208	11.9371	2.307988276	30.09
cc1220	1220	3.9416	2.91903	4.90646	1.680852886	17.79
cc1240	1240	3.7877	4.90719	9.49008	1.933913299	22.04
cc1260	1260	5.1081	6.0905	16.5453	2.716574994	27.94
cc1280	1280	3.6975	6.33705	13.0146	2.053731626	21.93
cc1300	1300	5.2789	4.92853	10.0887	2.046999815	25.84
cc1320	1320	7.5519	4.61934	10.8342	2.345399992	33.04
cc1340	1340	8.1699	7.38714	13.5843	1.838911947	39.71
cc1360	1360	6.9331	9.23465	23.2346	2.516023888	34.92
cc1380	1380	5.0735	5.78016	11.8297	2.046604246	23.45
cc1400	1400	4.8485	9.49564	31.8206	3.351074809	29.35
cc1420	1420	4.4132	6.79781	18.3571	2.700443231	20.96
cc1440	1440	6.381	18.7133	58.9927	3.152447724	39.79

cc1460	1460	3.9051	13.0758	39.4777	3.019142232	23.34
cc1480	1480	4.4597	19.8359	47.0769	2.373318075	32.66
cc1500	1500	4.9228	5.44315	14.8614	2.730294039	22.33
cc1520	1520	4.3063	7.31815	13.7575	1.879915006	23.4
cc1540	1540	6.0614	7.42057	17.674	2.381757736	28.06
cc1560	1560	2.6426	3.13064	6.02935	1.925916107	12.1
cc1580	1580	3.6283	17.1527	34.2272	1.995440951	25.56
cc1600	1600	4.6939	13.3574	33.534	2.510518514	28.1
cc1620	1620	3.0637	7.76398	17.1497	2.208879982	23.03
cc1640	1640	5.4700	9.89552	21.9672	2.219913658	32.37
cc1660	1660	7.3744	5.53915	10.5666	1.907621205	33.93
cc1680	1680	5.459	1.41464	1.68336	1.189956455	20.86
cc1700	1700	2.6873	0.43494	0.51877	1.192739228	9.152
cc1720	1720	4.8464	0.80888	0.9553	1.181015725	17.19
cc1740	1740	4.8145	0.7686	0.9078	1.181108509	15.6
cc1760	1760	4.5983	0.8526	1.0332	1.21182266	16.22
cc1780	1780	4.3694	1.3836	1.81093	1.308853715	16.8
cc1800	1800	4.9141	4.44211	10.1013	2.273986912	22.59
cc1820	1820	4.7277	6.39671	14.5858	2.280203417	24.69
cc1840	1840	3.8226	4.46129	10.0801	2.259458587	19.12
cc1860	1860	3.8949	2.79336	5.04103	1.80464745	18.93
cc1880	1880	5.6332	16.4203	30.1347	1.835210075	35.55
cc1900	1900	4.5856	2.39546	4.09471	1.709362711	20.62
cc1920	1920	4.1727	10.6038	17.6133	1.66103661	24.79
cc1940	1940	2.689	3.81678	6.71564	1.759504085	13.26
cc1960	1960	3.3816	4.28694	8.46943	1.975635302	16.4
cc1980	1980	2.6064	1.05601	1.52124	1.44055454	9.752
cc2000	2000	3.5981	20.4602	28.3942	1.387777246	22.94
cc2020	2020	3.6302	37.1881	60.75	1.633587088	27.27
cc2040	2040	4.3293	61.8433	79.2365	1.281246311	38.5
cc2060	2060	4.3834	43.0803	63.4904	1.473768753	29.65
cc2080	2080	4.2214	82.5473	113.697	1.377355771	43.56
cc2100	2100	2.7143	43.5203	59.9749	1.378090225	26.16
cc2120	2120	3.6228	45.4697	60.7207	1.335410174	28.86
cc2140	2140	2.4997	40.5994	51.8401	1.276868624	23.63
cc2160	2160	3.3736	56.3985	72.9723	1.293869518	31.87
cc2180	2180	3.4043	60.7274	77.0983	1.269580124	33.14
cc2200	2200	4.7589	24.7427	42.3923	1.713325547	31.78
cc2220	2220	1.4877	20.7215	28.9536	1.397273363	11.62
cc2240	2240	2.9898	22.4658	32.0939	1.428566977	18.26
cc2260	2260	4.4019	30.7216	48.9097	1.592029712	29.64
cc2280	2280	5.351	13.4486	30.3335	2.255513585	27.58
cc2300	2300	1.7647	4.60853	8.61501	1.869361814	9.538
cc2320	2320	2.7112	24.1006	34.2766	1.422230152	21.1
cc2340	2340	5.6897	15.6226	27.8386	1.781944107	32.81
cc2360	2360	4.6148	8.96235	18.796	2.097217806	25.92
cc2380	2380	4.2559	39.1906	49.1883	1.25510454	32.2
cc2400	2400	6.425	65.2909	83.956	1.28587598	49.83
cc2420	2420	1.8949	20.2683	27.0532	1.334754271	15.95
cc2440	2440	1.5487	8.43405	12.9516	1.535632347	11.09
cc2460	2460	3.6998	32.0273	42.5314	1.327973323	30.48
cc2480	2480	2.6422	11.9342	23.0929	1.935018686	17.9
cc2500	2500	3.582	43.5494	56.0634	1.287351835	30.03
cc2520	2520	3.0966	33.9796	46.572	1.370587058	28.07
cc2540	2540	4.8332	52.1152	76.699	1.471720343	39.71
cc2560	2560	4.6092	22.3903	36.2385	1.618491043	29.72
cc2580	2580	6.0175	17.2978	37.1528	2.147833829	33.63
cc2600	2600	5.4746	9.32076	18.3419	1.967854553	27.48
cc2620	2620	5.5082	55.7759	86.2975	1.547218422	43.58
cc2640	2640	2.5991	15.1425	31.0576	2.051021958	18.24
cc2660	2660	4.1677	12.3686	30.5627	2.470991058	27.04
cc2680	2680	4.8395	7.63889	22.2082	2.90725485	27.12
cc2700	2700	2.356	16.5071	35.7727	2.16710991	18.32
cc2720	2720	3.7533	3.40004	6.98498	2.054381713	20.86
cc2740	2740	5.8387	20.2486	52.7118	2.603231828	40.36
cc2760	2760	4.1748	10.2529	19.0367	1.85671371	27.66
cc2780	2780	6.0749	20.7046	48.6692	2.350646716	40.67
cc2800	2800	3.4781	6.1156	11.9501	1.954035581	22.31
cc2820	2820	3.7272	7.12039	17.9834	2.525620085	23.21
cc2840	2840	3.5727	4.29956	11.5642	2.689624055	25.46
cc2860	2860	3.2626	2.19116	3.3500	1.528870553	16.17
cc2870	2870	8.3127	13.1935	28.0194	2.123727593	68.6
cc2875	2875	1.8056	24.3743	67.9153	2.786348736	30.36
cc2880	2880	7.364	120.922	331.045	2.737673872	130

cc2885	2885	6.1538	153.773	138.514	0.900769316	136.9
cc2890	2890	2.1944	73.8464	157.471	2.132412684	51.85
cc2895	2895	5.6286	123.445	263.545	2.134918385	107.9
cc2900	2900	7.2959	62.2593	159.111	2.555618197	111
cc2905	2905	4.6853	5.01216	8.78518	1.752773255	38.64
cc2910	2910	2.2631	21.7525	53.1006	2.441126307	29.36
cc2915	2915	4.6421	75.4801	188.427	2.496379841	74.06
cc2920	2920	3.4919	57.9936	142.616	2.459167908	52.65
cc2925	2925	2.6783	38.2485	96.1554	2.513965254	37.96
cc2930	2930	4.0181	51.4659	131.523	2.555536773	51.11
cc2935	2935	3.6815	31.5798	93.569	2.962938334	41.99
cc2940	2940	2.4821	18.0822	63.1476	3.492252049	27.77
cc2945	2945	1.5958	13.7087	39.4113	2.874911553	17.18
cc2950	2950	4.0758	42.2113	112.658	2.668906193	56.59
cc2955	2955	6.3128	52.2629	168.864	3.231049176	77.07
cc2960	2960	3.9015	51.637	142.441	2.758506497	55.63
cc2965	2965	5.1329	44.9931	133.766	2.973033643	63.83
cc2970	2970	6.8416	66.582	216.492	3.251509417	90.9
cc2975	2975	4.8859	46.1057	138.972	3.014204317	58.62
cc2980	2980	3.614	40.1316	109.234	2.721894966	47.77
cc2985	2985	3.2199	39.8543	123.221	3.091786834	46.05
cc2990	2990	6.1666	43.7742	162.172	3.704739321	67.45
cc2995	2995	4.3200	32.5802	114.759	3.522354068	47.92
cc3000	3000	2.4994	24.0966	74.2445	3.081119328	31.34
cc3005	3005	4.288	41.6314	129.027	3.099271223	53.34
cc3010	3010	2.8561	20.491	69.0513	3.369835538	29.64
cc3015	3015	3.6909	9.24293	59.4387	6.430720562	32.09
cc3020	3020	4.5869	29.742	115.452	3.881783337	47.36
cc3025	3025	2.8173	16.6839	60.3476	3.617115902	27.6
cc3030	3030	5.2425	15.191	74.9306	4.932565335	36.2
cc3035	3035	3.5164	18.6222	72.2645	3.88055654	31.12
cc3040	3040	4.381	11.4058	52.8792	4.636167564	31.19
cc3050	3050	2.6404	14.0359	67.2684	4.792596128	29
cc3060	3060	2.0652	12.9879	47.7891	3.67950939	23.24
cc3065	3065	3.8966	17.2555	67.458	3.909362232	36.88
cc3070	3070	5.034	9.39404	30.0998	3.204137943	37.11
cc3075	3075	3.3189	2.64185	5.03617	1.906304294	19.43
cc3080	3080	3.2097	4.44632	19.2358	4.326229331	21.28
cc3085	3085	4.3602	2.80894	4.71231	1.677611483	25.48
cc3090	3090	5.7043	12.5815	66.8213	5.311075786	41.88
cc3095	3095	3.4525	14.2247	63.188	4.442132347	27.05
cc3100	3100	4.3086	14.9266	78.6862	5.271542079	36.1
cc3105	3105	1.9182	7.97609	33.3229	4.177849046	15.68
cc3110	3110	3.0634	10.3085	45.9871	4.461085512	24.36
cc3115	3115	3.8603	17.6818	72.2143	4.084103428	34.82
cc3120	3120	4.4497	18.6898	78.3864	4.194073773	38.48
cc3125	3125	1.7905	5.09166	19.7531	3.879500988	13.96
cc3130	3130	2.1997	10.6294	41.3909	3.894001543	20.27
cc3135	3135	3.7700	12.2759	50.4254	4.107674386	31.71
cc3140	3140	3.1457	12.8832	52.9881	4.112961066	27.98
cc3145	3145	6.5915	15.3791	75.0564	4.880415629	42.24
cc3150	3150	5.093	14.0671	61.9679	4.405165244	31.44
cc3155	3155	4.4631	10.1723	48.256	4.743863236	25.17
cc3160	3160	6.0286	9.56116	41.5686	4.347652377	28.27
cc3165	3165	5.5304	6.65522	30.3272	4.556904205	25.07
cc3170	3170	2.9938	2.01809	4.60065	2.279705068	13.39
cc3180	3180	2.9637	3.881	16.0326	4.131048699	15.44
cc3200	3200	1.6831	1.62659	5.61737	3.453463995	9.261
cc3220	3220	3.6246	3.6704	16.2152	4.417829119	14.43
cc3240	3240	4.0816	2.79224	9.88194	3.539072573	14.75
cc3260	3260	3.7388	4.85763	20.1132	4.14053767	17.24
cc3280	3280	4.4628	1.97551	10.7019	5.417284651	13.94
cc3300	3300	5.7432	2.99741	14.449	4.820495027	18.44
cc3320	3320	4.541	2.82205	11.2668	3.99241686	14.43
cc3340	3340	3.8851	5.67497	20.8366	3.671666987	17.06
cc3360	3360	2.5333	4.25457	16.9918	3.993776104	10.81
cc3380	3380	2.9693	5.50369	20.4814	3.721394192	12.63
cc3400	3400	1.7389	1.12706	1.44326	1.280552943	6.386
cc3420	3420	1.8889	9.63311	18.3091	1.900642679	12.44
cc3440	3440	5.8599	9.43763	30.5441	3.236416346	25.36
cc3460	3460	4.1761	2.52738	8.55463	3.384781869	14.7
cc3480	3480	3.1091	13.3837	32.5905	2.435088951	19.36
cc3500	3500	3.2562	2.69848	10.604	3.929619638	12.01
cc3520	3520	4.0567	20.3835	39.8374	1.954394486	21.13

cc3540	3540	3.9098	21.0498	39.9094	1.895951505	23.17
cc3560	3560	3.7652	18.3412	37.2429	2.030559614	20.89
cc3580	3580	3.8723	25.3779	44.1018	1.737803364	21.79
cc3600	3600	6.178	51.4785	83.6506	1.624961877	37.43
cc3620	3620	3.4259	53.1379	83.3655	1.568851987	33.18
cc3640	3640	4.1948	57.1514	91.3908	1.599099935	32.41
cc3660	3660	2.3393	28.8208	46.6605	1.618986982	17.78
cc3680	3680	4.8155	39.7873	67.3967	1.693924946	28.97
cc3700	3700	5.754	49.7734	93.1163	1.870804486	37.96
cc3720	3720	3.7587	41.2954	71.8835	1.740714462	27.5
cc3740	3740	3.038	46.091	73.0097	1.584033759	26.72
cc3760	3760	5.1889	40.1543	62.5469	1.557663812	31.47
cc3780	3780	3.7926	50.5974	81.7377	1.615452573	31.83
cc3800	3800	3.2671	53.8742	81.5709	1.514099513	29.88
cc3820	3820	4.7667	78.0143	123.476	1.582735473	44.55
cc3840	3840	4.5151	85.7547	137.647	1.60512485	50.95
cc3860	3860	4.5997	127.753	175.723	1.375490204	64.16
cc3880	3880	6.979	145.19	213.259	1.468827054	74.88
cc3900	3900	4.2577	114.25	163.216	1.428586433	59.68
cc3920	3920	5.5745	81.9734	133.723	1.63129747	51.73
cc3940	3940	4.0298	9.34897	11.7232	1.253956318	18.91
cc3960	3960	3.9766	73.777	118.441	1.605391924	42.88
cc3980	3980	2.3897	62.5273	111.303	1.780070465	32.72
cc4000	4000	3.0024	58.5826	106.864	1.824159392	34.3
cc4020	4020	4.1429	93.8349	154.777	1.649460915	51.41
cc4040	4040	3.8785	66.7441	155.914	2.33599674	42.93
cc4060	4060	2.8634	25.1759	46.5887	1.850527687	22.01
cc4080	4080	3.1084	131.876	200.581	1.520981831	57.8
cc4100	4100	4.5332	202.44	277.96	1.373048805	88.24
cc4120	4120	3.9918	79.0753	127.021	1.606329663	43.82
cc4145	4145	3.0418	263.577	364.736	1.383792971	104.6
cc4160	4160	1.6628	244.989	305.46	1.24683149	80.14
cc4180	4180	2.9704	51.8906	87.1817	1.680105838	31.38
cc4200	4200	3.2592	70.75	114.841	1.623194346	39.42
cc4220	4220	2.627	44.0718	77.5488	1.759601378	28.62
cc4240	4240	2.9135	40.6957	87.5831	2.152146296	33.1
cc4260	4260	3.7003	56.0815	80.0669	1.427688275	35.25
cc4280	4280	3.7213	46.0719	51.8776	1.126013904	31.49
cc4300	4300	3.9041	71.5023	124.773	1.74502079	44.28
cc4320	4320	3.9387	155.914	201.874	1.29477789	65.21
cc4340	4340	5.6995	124.173	169.411	1.364314303	69.54
cc4360	4360	6.7652	98.127	189.344	1.929581053	70.66
cc4380	4380	2.963	51.9306	92.127	1.774040739	32.58
cc4400	4400	3.0782	51.9003	85.6503	1.650285258	33.2
cc4420	4420	5.1353	75.1329	110.785	1.474520483	49.95
cc4440	4440	5.1133	65.2699	102.334	1.567858998	43.29
cc4460	4460	3.0935	52.6746	83.0191	1.576074617	33.43
cc4480	4480	5.4563	32.0497	72.1175	2.250177069	36.65
cc4500	4500	4.103	64.5718	101.615	1.573674576	41.11
cc4520	4520	4.7508	64.7088	90.0797	1.392078048	39.22
cc4540	4540	3.3095	47.6953	78.1023	1.637526129	30.69
cc4560	4560	4.208	63.2627	101.112	1.598287775	42.22
cc4580	4580	4.3905	63.6305	85.6646	1.34628205	41.06
cc4600	4600	4.5456	81.1034	125.246	1.544275579	47.49
cc4620	4620	5.126	80.8073	120.793	1.494827819	55.33
cc4640	4640	6.196	96.7136	151.555	1.567049515	57.99
cc4660	4660	5.845	54.3574	90.0208	1.656090983	38.61
cc4680	4680	1.8765	17.4817	31.7689	1.817266055	12.67
cc4700	4700	4.0537	38.4807	76.6339	1.99148924	29.11
cc4720	4720	4.4776	30.2892	62.41	2.060470399	28.98
cc4740	4740	3.8541	36.9225	65.7908	1.781862008	27.15
cc4760	4760	3.2141	26.7131	45.6319	1.708221809	19.45
cc4780	4780	4.8115	15.1616	34.8902	2.301221507	19.95
cc4800	4800	2.4525	3.85514	7.20091	1.867872503	12.85
cc4820	4820	3.7527	42.0698	66.833	1.588621767	27.85
cc4840	4840	4.8446	57.992	101.766	1.754828252	37.44
cc4860	4860	2.1931	24.5096	42.2789	1.724993472	15.54
cc4880	4880	4.5605	34.6078	86.0403	2.486153411	37.81
cc4900	4900	4.1521	17.5701	43.16	2.456445894	22.89
cc4920	4920	2.8685	27.201	57.2108	2.10326091	22.38
cc4940	4940	4.9214	41.5349	81.2826	1.956971125	30.81
cc4960	4960	2.4977	24.3122	51.4921	2.117953126	19.05
cc4980	4980	1.455	10.524	21.7738	2.068966173	10.34
cc5000	5000	3.3281	21.1868	46.4906	2.194319104	21.42

cc5020	5020	4.6928	46.4079	86.3817	1.861357657	38.22
cc5040	5040	2.6512	29.9219	54.0325	1.805784392	20.5
cc5060	5060	4.2043	28.6183	72.5384	2.534685848	30.5
cc5080	5080	1.5734	8.87704	20.2896	2.28562674	9.357
cc5100	5100	4.5478	12.5857	22.5713	1.793408392	22.93
cc5120	5120	3.9098	40.9722	78.9652	1.927287283	31.28
cc5140	5140	4.4543	14.3869	45.7501	3.179983179	25.06
cc5160	5160	2.9636	24.4027	49.839	2.042355969	20.35
cc5180	5180	2.7111	17.2242	43.0989	2.502229421	18.47
cc5200	5200	5.7788	10.9582	35.5794	3.246828859	26.45
cc5220	5220	2.3106	12.8043	29.0811	2.271197957	15.47
cc5240	5240	4.4166	29.6825	78.684	2.650854881	31.46
cc5260	5260	4.6863	8.7235	36.0586	4.133501462	23.2
cc5280	5280	3.9347	10.5809	40.876	3.863187442	26.67
cc5300	5300	4.2797	14.6538	44.4734	3.034939743	25.13
cc5320	5320	3.6563	3.97862	16.2753	4.090689737	15.52
cc5330	5330	4.3585	18.6408	61.1669	3.281345221	27.29
cc5340	5340	2.6124	5.60529	21.1791	3.778412892	12.94
cc5360	5360	2.3542	9.71883	29.9111	3.07764412	15.8
cc5380	5380	4.0277	23.8727	63.18	2.646537677	27.42
cc5390	5390	3.3411	20.4798	53.7141	2.622784402	25.96
cc5400	5400	4.2795	20.5395	55.5575	2.704910051	29.79
cc5410	5410	2.9168	10.3256	30.2567	2.930260711	16.37
cc5420	5420	2.0655	1.15408	1.45589	1.261515666	11.25
cc5430	5430	5.2612	40.669	75.4067	1.854156729	58.17
cc5440	5440	2.4726	15.1978	48.0815	3.163714485	26.69
cc5450	5450	3.9188	19.6939	65.1849	3.309903066	32.05
cc5460	5460	2.8242	28.5076	71.4471	2.506247457	25.96
cc5470	5470	3.8304	44.4335	101.191	2.277358299	40.66
cc5480	5480	2.9233	38.6816	91.8905	2.37556099	33.61
cc5490	5490	2.7341	9.65644	38.0229	3.937569125	17.66
cc5500	5500	4.0221	19.4845	59.2081	3.03872822	25.75
cc5510	5510	2.0249	10.6157	35.1877	3.314684854	15.34
cc5520	5520	4.6541	20.5996	65.316	3.170741179	28.5
cc5550	5550	6.2352	24.7149	70.8652	2.867306766	32.81
cc5570	5570	6.3502	25.1121	67.7972	2.699782177	34.71
cc5590	5590	2.3774	6.10688	18.729	3.066868843	11.77
cc5610	5610	3.8076	25.9008	67.2038	2.594661169	27.59
cc5630	5630	6.4283	38.5701	101.871	2.641190974	39.94
cc5650	5650	3.6485	31.8246	83.675	2.629255356	32.38
cc5670	5670	4.8858	19.3778	60.9535	3.145532517	27.45
cc5690	5690	4.0851	8.84516	33.9224	3.835136956	21.18
cc5710	5710	2.5765	2.21043	9.65241	4.366756694	10.47
cc5730	5730	5.422	10.5031	41.5084	3.952014167	24.11
cc5750	5750	3.1697	10.1368	33.0162	3.257063373	15.51
cc5770	5770	5.142	7.76588	32.4458	4.177993994	20.96
cc5790	5790	6.1325	11.908	47.3208	3.973866308	26.29
cc5810	5810	5.4334	6.31768	30.2902	4.794513176	20.99
cc5830	5830	6.3676	10.4391	46.004	4.406893315	27.59
cc5850	5850	3.0708	3.33128	13.9117	4.176082467	12.24
cc5870	5870	2.976	5.9257	25.7855	4.351469025	13.75
cc5890	5890	2.5199	0.90291	1.24079	1.374212269	6.546
cc5910	5910	2.797	2.14817	11.8016	5.493792391	8.966
cc5930	5930	3.6121	4.85782	21.8875	4.505621863	13.98
cc5950	5950	3.324	6.46043	27.0383	4.185216773	15.08
cc5970	5970	2.7903	3.23311	16.4774	5.096455116	10.12
cc5990	5990	3.6354	6.90753	28.8991	4.183709662	14.99
cc6010	6010	3.0826	4.72476	19.7426	4.178540286	11.09
cc6030	6030	3.4133	3.25479	16.48	5.063306696	11.07
cc6050	6050	1.8742	1.73158	10.8129	6.244528119	8.547
cc6070	6070	2.9161	5.56645	25.7627	4.62821008	14.42
cc6090	6090	3.9943	7.49587	35.1851	4.693931458	19.74
cc6110	6110	4.4044	11.7426	47.3903	4.035758691	24.52
cc6130	6130	3.7623	14.8225	59.7063	4.028085681	27.24
cc6150	6150	2.3403	5.10727	20.634	4.040123197	14.62
cc6170	6170	2.6147	2.09241	10.2273	4.887808795	10.81
cc6190	6190	4.3204	5.9128	28.3566	4.795798945	16.47
cc6210	6210	4.0578	7.41247	42.4225	5.72312603	19.37
cc6230	6230	4.2539	2.36926	8.46492	3.572811764	12.67
cc6250	6250	5.0638	6.91778	33.3344	4.818655696	19.67
cc6270	6270	2.2301	3.48794	16.2822	4.668142227	9.592
cc6290	6290	2.5235	2.94616	15.2592	5.179352106	9.353
cc6310	6310	2.6719	4.81754	22.1073	4.588918826	12.22
cc6330	6330	2.2017	1.53975	7.21214	4.683968177	7.707

cc6340	6340	2.9791	2.47137	18.1213	7.332491695	10.46
cc6360	6360	3.7296	7.95678	35.8917	4.510832271	19.73
cc6380	6380	2.2345	0.87041	1.07946	1.240174171	9.194
cc6400	6400	3.0095	5.36381	25.6271	4.777779228	14.11
cc6420	6420	2.6718	5.23539	24.6239	4.703355433	13.44
cc6440	6440	2.9251	3.91226	19.9372	5.096082571	13.28
cc6460	6460	3.4275	6.57704	31.2989	4.758812475	17.56
cc6480	6480	2.1263	2.72505	12.7492	4.67851966	7.815
cc6500	6500	4.2296	10.0518	41.914	4.169800434	21.03
cc6520	6520	1.9373	2.99816	15.3845	5.131313873	11.22
cc6540	6540	1.5427	3.60914	16.3878	4.54063849	8.913
cc6560	6560	3.1589	6.22856	28.6622	4.601737801	16.16
cc6580	6580	2.8242	8.10473	33.4174	4.123197195	16.64
cc6600	6600	4.4207	8.42405	36.6395	4.349392513	24.25
cc6620	6620	3.0924	7.65559	37.9073	4.951584398	17.97
cc6640	6640	2.6549	3.45201	18.8809	5.469538037	13.67
cc6660	6660	4.3752	3.10544	17.1861	5.534191612	16.02
cc6680	6680	3.828	8.70444	46.7528	5.371143922	21.69
cc6700	6700	3.2053	5.20272	31.1275	5.982928161	15.82
cc6720	6720	3.7378	4.22151	21.0262	4.980729644	15.82
cc6740	6740	3.427	4.65796	24.7365	5.310586609	15.97
cc6760	6760	3.3252	4.58768	28.8107	6.280015171	17.28
cc6780	6780	2.2149	3.95741	25.136	6.351628969	11.94
cc6800	6800	4.3083	8.32572	50.9296	6.11714062	23.55
cc6820	6820	2.6322	1.23058	2.52817	2.054453997	11.58
cc6840	6840	2.7966	2.76285	19.9274	7.212624645	10.14
cc6860	6860	3.952	3.51545	20.4113	5.806169907	14.68
cc6880	6880	3.3349	3.7678	27.0255	7.172753331	15.26
cc6900	6900	3.6676	2.871	18.6962	6.512086381	12.83
cc6920	6920	3.5335	3.46358	21.116	6.096582149	13.95
cc6940	6940	2.6788	6.202	36.169	5.831828442	17.06
cc6960	6960	2.521	4.16308	23.1423	5.558937133	13.39
cc6980	6980	4.2532	6.13351	38.7112	6.311426899	21.57
cc7000	7000	5.9457	6.05863	42.8241	7.068281113	24.27
cc7020	7020	4.2914	4.76847	27.8254	5.835288887	19.84
cc7040	7040	3.1972	2.71352	18.2066	6.709587547	11.57
cc7060	7060	5.7143	4.83868	34.2802	7.084618119	24.2
cc7080	7080	2.338	7.43458	41.9898	5.647904791	18.08
cc7100	7100	2.6723	3.37569	21.5925	6.396470055	12.66
cc7120	7120	2.6566	5.85737	36.4685	6.226087818	18.58
cc7140	7140	2.8432	3.27677	20.0392	6.115534505	12.56
cc7160	7160	3.0741	2.12876	11.5584	5.42963979	10.36
cc7180	7180	2.7084	3.16137	20.1683	6.379607575	13.79
cc7200	7200	1.9307	2.63389	13.8951	5.275505051	10.24
cc7220	7220	3.1738	3.20445	16.5745	5.172338467	10.68
cc7240	7240	2.2543	9.38339	40.5203	4.318300742	18.3
cc7260	7260	2.2500	10.1157	41.6756	4.11989284	19.19
cc7280	7280	1.7718	15.6657	48.0612	3.067925468	20.83
cc7300	7300	2.9771	7.19255	33.963	4.72196926	17.9
cc7320	7320	6.6097	9.69736	51.1532	5.274961433	28.48
cc7340	7340	4.0919	3.35862	23.5044	6.998231416	19.93
cc7360	7360	6.5692	3.42917	19.2627	5.617306812	22.58
cc7380	7380	4.3544	4.07145	28.6271	7.031180538	16.56
cc7400	7400	3.7000	2.33565	14.2333	6.093935307	10.83
cc7420	7420	6.0996	2.27689	16.1414	7.089231364	18.64
cc7440	7440	2.9541	0.75661	0.91394	1.207940683	8.042
cc7460	7460	1.9696	0.50035	0.57329	1.145777955	5.764
cc7480	7480	4.529	0.85633	0.96969	1.132378873	11.27
cc7500	7500	5.666	0.80792	0.94889	1.174485098	14.03
cc7520	7520	6.8075	0.97641	1.14293	1.170543112	14.12
cc7540	7540	6.0887	0.77217	0.9482	1.227967935	12.27
cc7560	7560	6.9622	1.0457	1.16441	1.113522043	13.97
cc7580	7580	5.4911	0.82391	0.94366	1.145343545	11.59
cc7600	7600	4.5751	0.80121	0.90229	1.126159184	11.74
cc7620	7620	3.6398	0.7164	0.82723	1.154704076	11.36
cc7640	7640	3.7858	0.99496	1.14357	1.149362788	13.75
cc7660	7660	4.0863	1.3481	2.93014	2.173533121	16.8
cc7680	7680	5.2819	9.78467	49.2662	5.035039506	24.19
cc7700	7700	3.9711	11.3286	42.2316	3.727874583	22.14
cc7720	7720	6.636	9.33205	41.6426	4.462320712	19.88
cc7740	7740	3.3473	20.0559	55.2354	2.754072368	22.98
cc7760	7760	5.4586	2.54779	8.15938	3.202532391	19.71
cc7780	7780	4.0839	0.91501	1.10202	1.20438028	11.95
cc7800	7800	2.495	0.77359	0.91205	1.178983699	10.76

cc7820	7820	6.4213	7.24885	47.1922	6.510301634	23.54
cc7840	7840	4.4266	26.8932	73.2727	2.724580935	26.6
cc7860	7860	5.2396	3.64449	4.54842	1.248026473	15.96
cc7880	7880	5.6545	16.5634	60.7939	3.670375648	28.27
cc7900	7900	4.1014	13.0307	40.2955	3.09235114	20.15
cc7920	7920	2.5791	0.68705	0.85258	1.240928608	7.925
cc7940	7940	4.2158	15.1646	46.9481	3.09590098	21.51
cc7960	7960	3.9297	46.338	101.813	2.197181579	34.87
cc7980	7980	4.0851	52.2128	105.576	2.022032911	36.03
cc8000	8000	4.5978	39.9592	64.2793	1.608623296	28.63
cc8020	8020	6.1366	66.5626	138.011	2.07340158	47.73
cc8040	8040	7.1427	77.7392	167.387	2.153186552	56.5
cc8060	8060	4.7271	29.94	68.7298	2.295584502	28.63
cc8080	8080	3.1833	7.85515	15.8872	2.022520257	26.23
cc8100	8100	2.2754	1.29255	1.52936	1.183211481	16.31

Part 2

Understanding the late Paleocene–early Eocene climate evolution

Chapter 5

The carbon cycle

5.1 The long-term carbon cycle

The cycle of carbon is essential to the maintenance of life, to climate, and to the composition of the atmosphere and ocean. What is normally thought of as the "carbon cycle" is the transfer of carbon between the atmosphere, the oceans, and life (fig. 5.1). The characteristic time for transferring carbon between these reservoirs range from days to tens of thousands of years, and is thus referred to as the short-term carbon cycle.

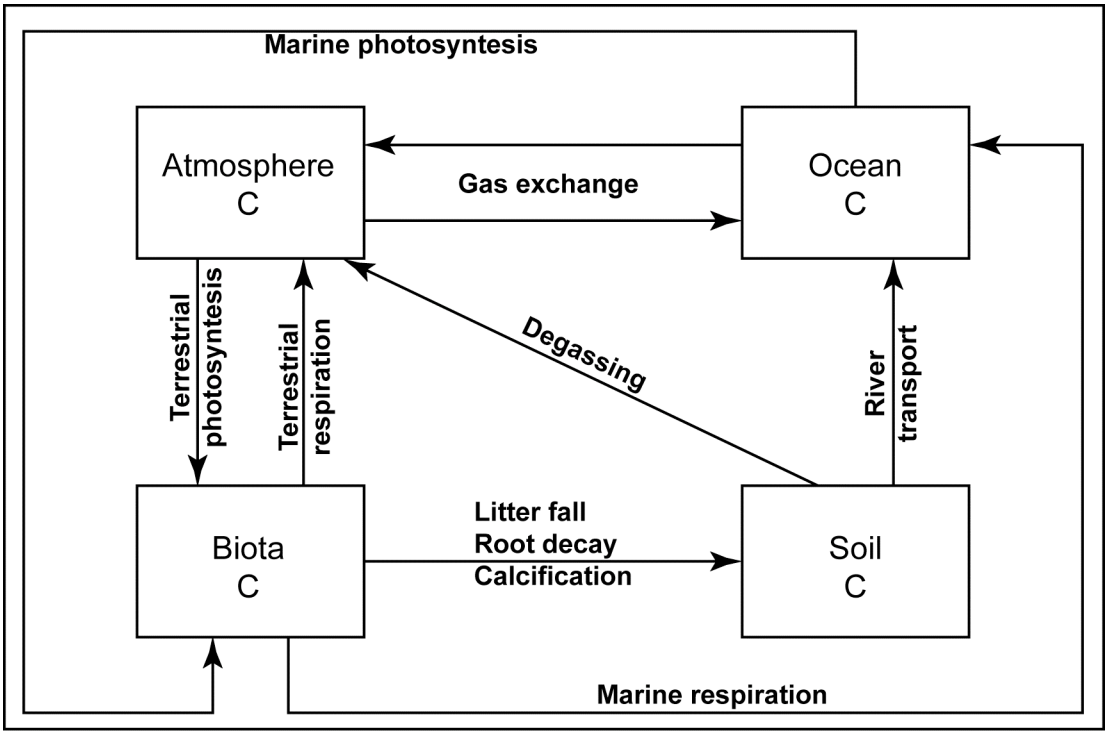

Figure 5.1. Scheme of the short-term carbon cycle representing the transport processes between the reservoirs involved in this mechanism; modified after Berner (2004).

Over millions of years carbon still undergoes constant cycling and recycling via short-term cycle, but added to this is the transfer of carbon to rocks and from rocks; this

exchange is the distinctive characteristic of the long-term carbon cycle, and is schematized in figure 5.2.

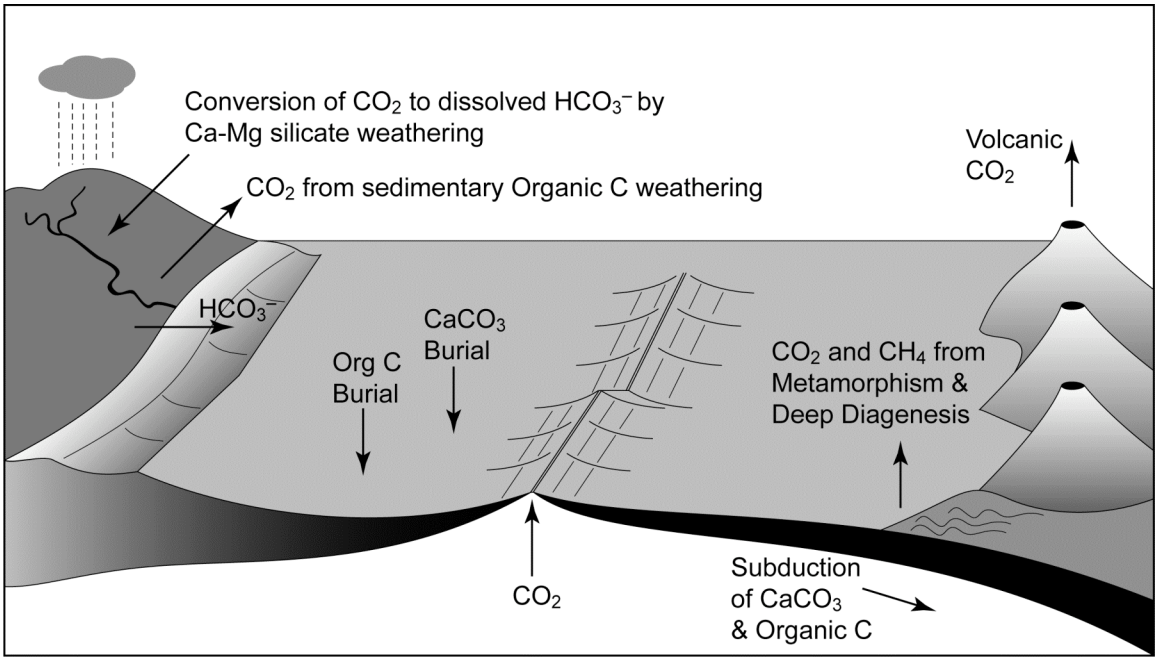

Figure 5.2. The long-term carbon cycle; modified after Berner (2004).

Over millions of years carbon transfers to and from rocks can result in changes in atmospheric CO_2 that cannot be attained via the short-term carbon cycle; this is due to the higher amount of carbon stored in rocks (~6250 x 10^{18} mol) than all the other reservoirs combined (~3.2 x 10^{18} mol; see Berner, 2004 for details). The maximum change in atmospheric CO_2 that could be obtained, for example by burning all terrestrial life and equilibrating the resulting CO_2 with the oceans, would be less than a 25% increase from the present level (Berner, 1989). In contrast, changes in the long-term carbon cycle have likely resulted in past increases in atmospheric CO_2 to levels more than 10 times the present level, resulting in intense global warming (Crowley and Berner, 2001).

Atmospheric carbon dioxide is taken up by plant photosynthesis, and organic matter builds up in soils. Microbial decomposition in the soil leads to a buildup of organic acids and CO_2 in soils. The organic acids and the carbonic acid formed from CO_2 react with minerals in rocks to liberate cations and acid anions to solution, and the organic acid anions are oxidized to bicarbonate. In particular, the reaction with Ca- and Mg- bearing silicate minerals plays a fundamental role in the long-term carbon cycle. A representative overall reaction for a generalized calcium silicate is

$$2CO_2 + 3H_2O + CaSiO_3 \rightarrow Ca^{++} + 2HCO_3^- + H_4SiO_4 \qquad (1.1)$$

The dissolved species are carried by groundwater to rivers and by rivers to the oceans, where the Ca^{++} and the HCO_3^- are precipitated, mostly biogenically, as calcium carbonate:

$$Ca^{++} + 2HCO_3^- \rightarrow CaCO_3 + CO_2 + H_2O \qquad (1.2)$$

and the silicic acid as biogenic silica:

$$H_4SiO_4 \rightarrow SiO_2 + 2H_2O \qquad (1.3)$$

The calcium carbonate and biogenic silica are then buried in marine sediments and eventually in the geological record. Combining the described reactions we obtain:

$CO_2 + CaSiO_3 \rightarrow CaCO_3 + SiO_2$ (1.4)

This is a key reaction of the long-term carbon cycle and represents the transfer of carbon from the atmosphere to the rock record by means of weathering of silicates followed by marine carbonate sedimentation. It can as well be written in terms of Mg and Ca-Mg silicates and carbonates. While the weathering of Ca and Mg silicates plays a major role in the long-term cycle, weathering of Na and K silicates does not lead to loss of CO_2 because these elements do not form common carbonate minerals in sediments. The CO_2 consumed during Na and K silicate weathering is returned to the atmosphere during the formation of new Na and K silicates in the sediments (see Mackenzie and Garrels, 1966). Also, weathering of Mg silicates does not necessitate the formation of Mg-containing carbonates. The dissolved Mg from silicate weathering, when delivered to the oceans, is well known to undergo a series of different reactions with submarine basalts that results in the liberation of Ca that is precipitated as $CaCO_3$ (Berner and Berner, 1996).

If the (1.4) reaction were to continue alone, all atmospheric CO_2 would be removed in only about 10,000 years or, with resupply of CO_2 from the oceans, in about 300,000 years (Sundquist, 1991). Over millions of years there must be a restoring process, and the principal one is the degassing of CO_2 to the atmosphere and oceans via the opposite of the reaction (1.4), i.e., for a reference Ca silicate,

$CaCO_3 + SiO_2 \rightarrow CO_2 + CaSiO_3$ (1.5)

Reaction (1.5) represents decarbonation via volcanism, metamorphism, and diagenesis, and together reactions (1.4) and (1.5) and their Mg silicate and carbonate analogues constitute the silicate-carbonate subcycle. Reactions (1.4) and (1.5) are used to simplify representation of the silicate-carbonate subcycles. In reality weathering involves Ca and Mg aluminosilicates, such as calcium plagioclase, with aluminum precipitated as clay minerals. The clay minerals are then involved in reactions with calcium carbonate or dolomite to form igneous and metamorphic (and even diagenetic) silicates. But the overall principal CO_2 uptake and release is the same as represented by reactions (1.1)–(1.5).

So far the weathering of carbonates has not been mentioned. This is because, on a million-years time scale, it has little direct effect on atmospheric CO_2. This can be seen by the weathering reaction for calcium carbonate:

$$CO_2 + H_2O + CaCO_3 \rightarrow Ca^{++} + 2HCO_3^- \qquad (1.6)$$

This is the reverse of reaction (1.2) for the precipitation of $CaCO_3$ in the oceans. Thus, the weathering of $CaCO_3$, followed by transport of Ca^{++} and HCO_3^- to the oceans and the precipitation of new $CaCO_3$, results in no net change in atmospheric CO_2. On shorter time scale (e.g., stages of the Pleistocene epoch), weathering of carbonates can be greater than, or less than, their precipitation from the oceans, with the excess carbon stored in or lost from seawater. However, over millions of years the necessary storage or loss become so

excessive (the mean residence time for bicarbonate in the oceans is about 100,000 years; see Holland, 1978) that purely inorganic precipitation will occur or carbonate sediments cannot form. There are evidence that such extreme conditions have been occurred, for example, during the Paleocene-Eocene thermal maximum (PETM), when a rapid release of ~2000 x 10^9 metric tons of carbon in the ocean-atmosphere reservoir caused a massive sea-floor carbonate dissolution (Zachos et al., 2005).

The long-term carbon cycle has another component, the organic subcycle. This is represented by the reactions

$$CO_2 + H_2O \rightarrow CH_2O + O_2 \qquad (1.7)$$

$$CH_2O + O_2 \rightarrow CO_2 + H_2O \qquad (1.8)$$

Reaction (1.7) is normally though to represent photosynthesis (short-term carbon cycle). In the long-term cycle it represent *net* photosynthesis, i.e. resulting from the burial of organic matter into sediments. It is the principal process of atmospheric O_2 production (Ebelmen, 1845). Reaction (1.8) represents the oxidation of old organic carbon in rocks, called "georespiration". This georespiration occurs either by oxidative weathering of organic matter in shales and other sedimentary rocks uplifted onto the continents, or by the microbial or thermal decomposition of organic matter to reduced carbon containing gases, followed by oxidation of the gases upon emission to the atmosphere. An example of the latter is

$2CH_2O \rightarrow CO_2 + CH_4$ (1.9a)

$CH_4 + 2O_2 \rightarrow CO_2 + 2H_2O$ (1.9b)

which together sum to reaction (1.8).

A special example of reaction (1.8) is the burning of fossil fuels by humans. Coal and oil are concentrated forms of sedimentary organic matter. Under natural processes the coal and oil is slowly oxidized by weathering and thermal degassing of hydrocarbon as mentioned above. However, humans have extracted these substance from the ground so quickly, from a geological perspective, the oxidation of the carbon occurs at a rate about 100 times faster than would occur naturally. As a result the long-term carbon cycle impinges on the short-term cycle, and this has led to an extremely fast historic rise in atmospheric CO_2 (IPCC, 2001) (Berner, 2004).

5.2 Atmospheric CO_2, climate, and chemical weathering of silicates

As described above, on geologic time scale the amount of CO_2 in the atmosphere is determined by processes such as organic-carbon and carbonate-carbon sedimentation and burial, silicates and organic carbon weathering on land, and volcanic and metamorphic release of CO_2 (Garrels et al., 1975; Kump et al., 2000; figure 5.2). In particular, the chemical weathering of silicates provide a mechanism to transfer the carbon from the atmospheric-oceanic reservoir to the lithosphere (reaction 1.4). Generally, a rise in atmospheric CO_2 partial pressure (pCO_2) causes an increase in annual mean temperatures by the greenhouse effect. The rise of the mean temperatures increase ocean evaporation

rates and generates a more vigorous hydrologic cycle (Gibbs et al., 1999). Even though other factors (such as lithology, topography, and vegetation) can influence the chemical weathering rates, these climatic conditions enhance chemical weathering of Ca- and Mg-silicates (among the other minerals), followed by the carbonate sedimentation in the oceans; this process lead to a decrease of the pCO_2. Thus, changes in weathering rates induced by variation in pCO_2 serve as negative feedback for stabilization of the global temperature. This long-term negative feedback control of pCO_2 variations by the weathering of silicates (schematized in figure 5.3) has been the climate stabilizing mechanism over Earth's history during the Phanerozoic (Walker et al., 1981; Gibbs et al., 1999; Kump et al., 2000).

The climate temperature dependence of the chemical weathering is supported by studies conducted on present-day watersheds. Velbel (1993) considered two lithologically analogous watersheds placed at different mean elevation (i.e. different annual mean temperatures) in the eastern United States (Blue Ridge Mountains); the lower elevation watershed (i.e. with higher annual mean temperature) had a larger chemical yield (see also Kump et al., 2000). The rate of precipitation and runoff could also depend by paleogeographic factors; for example Gibbs et al. (1999) pointed out that mid-Cretaceous to early Tertiary Tethyan geographies yielded the wettest continental climates and the highest runoff rates, because the continents were smaller and widely dispersed making numerous oceans and seaways available as moisture sources.

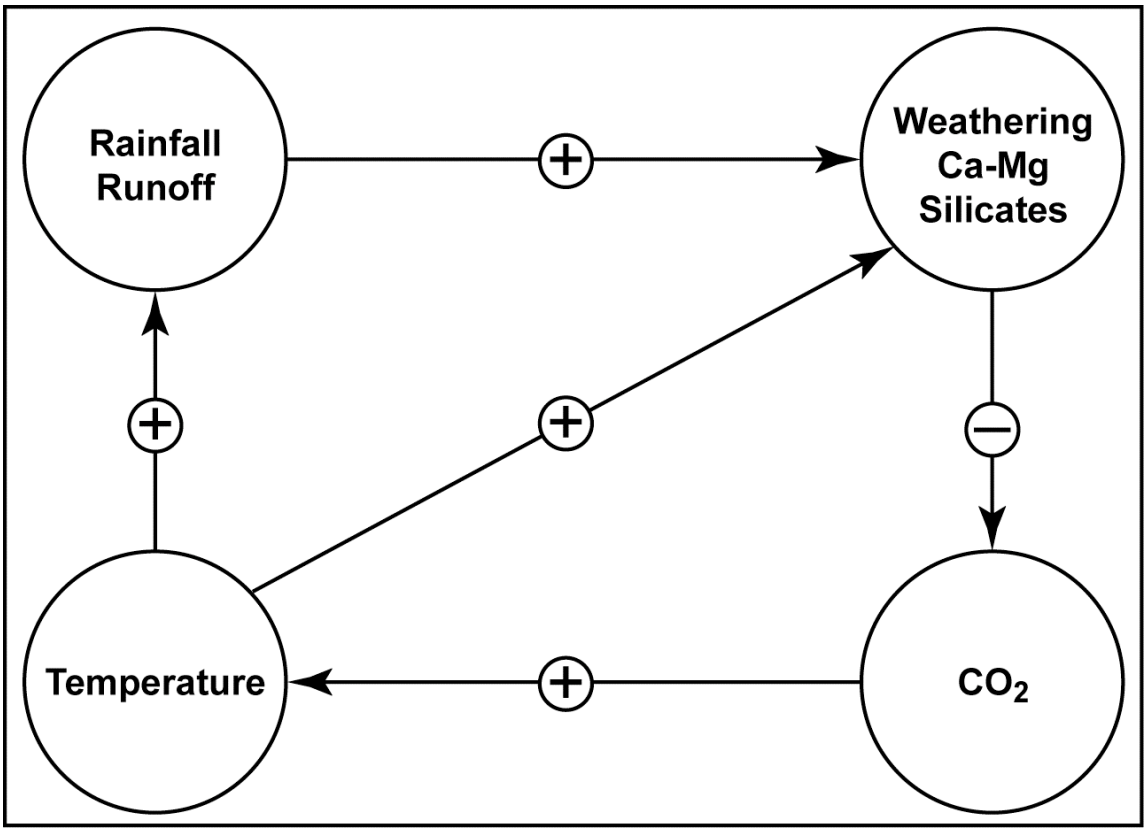

Figure 5.3. Systematic analysis diagram for the greenhouse-silicate weathering feedback. In such diagram arrows with the plus (minus) sign represent positive (negative) response; modified after Berner (2004).

The observation of natural systems allowed determining a generally reproducible weathering series which predicts that the dissolution rates of minerals decrease in the order olivine > Ca-plagioclase > pyroxene > Na-plagioclase > K-feldspar > muscovite > quartz (e.g. Krauskopf, 1979; Berner and Berner, 1996; Kump et al., 2000). Among Ca, Mg, K, and Na, iron (Fe) is a very common constituent of rock minerals; with mass-%, Fe is the fourth most abundant element of the Earth's crust. It exists predominantly in the divalent state and is located in silicates such as olivine, biotite, pyroxene, and amphibole as well as in sulfides (e.g., pyrite) and carbonates (e.g., siderite). Once exposed to aerobic

weathering, Fe^{2+} will be readily oxidized to Fe^{3+} that, in the common pH range of soils, will immediately hydrolyze and form sparingly soluble Fe^{III} oxides. The proportion of the iron in the parent rock "weathered" into Fe^{III} oxides through this reaction can ranges between a few percent to almost 100% for highly weathered bedrocks (Schwertmann, 2008). Consequently, an intense chemical weathering leads to a high Fe^{III} oxides production, followed by transport via continental runoff to the oceans.

5.3 Proxies of continental weathering

Most of the possible geochemical proxy indicators of continental weathering intensity are monitors of ocean chemistry changes ultimately registered in the sedimentary record. These include variations in radiogenic isotope ratios ($^{87}Sr/^{86}Sr$, $^{143}Nd/^{144}Nd$, $^{187}Os/^{186}Os$) recorded by carbonate and phosphate minerals precipitated from seawater, elemental ratios such as Ge/Si, global carbonate burial rate variations, and variations in global opal/chert deposition. All of these reflect either changes in fluxes of dissolved species delivered by rivers or changes in mean composition of riverine dissolved components (see Kump et al., 2000 for a review). However, all the listed proxies of chemical weathering are not infallible indicators of changing weathering fluxes; this is because of the assumptions that must be made when interpreting them, not to mention the difficulty in locating pristine, unaltered samples for analysis. Thus, the best approach would be to use multiple proxy parameters.

In the next chapter we explore the possibility to use the iron oxides contained in the sediments as proxy of the chemical weathering on land; in particular, we detected a relative increase of the hematite content of the Cicogna section sediments across the

PETM and generally during the early Eocene. We associated these relative enrichments in the Fe^{3+}-bearing minerals to the enhanced continental weathering rates during the global warm climate conditions that characterized the Earth during the early Paleogene. Hematite is a common product of silicate weathering, formed by the chemical weathering of Fe-bearing primary minerals (Schwertmann, 2008). Once formed, hematite is then transported and eventually accumulated in the sedimentation basin by the continental run-off. Our results confirm the presence, at least during the early Paleogene, of the silicate weathering negative feedback mechanism for the long-term stabilization of the Earth's surfaces temperature described above.

Chapter 6

The silicate weathering machine at work: rock-magnetic data from the late Paleocene–early Eocene Cicogna section (Italy)

Edoardo Dallanave[1,2], Lisa Tauxe[3], Giovanni Muttoni[2,4], Domenico Rio[1]

[1] Department of Geosciences, University of Padova, Via Giotto 1, I-35137 Padova, Italy.

[2] ALP - Alpine Laboratory of Paleomagnetism, Via Madonna dei Boschi 76, I-12016 Peveragno (CN), Italy.

[3]Scripps Institution of Oceanography, La Jolla, CA 92093-0220, USA.

[4] Department of Earth Sciences, University of Milan, Via Mangiagalli, 34 I-20133 Milano, Italy.

Abstract

We present the rock-magnetic stratigraphy of the late Paleocene–early Eocene Tethyan marine Cicogna section (Venetian Southern Alps, NE Italy). The ~81 m Cicogna section extends from Chron C25r to Chron C23r spanning the NP7/NP8-NP12 nannofossil Zones (~52.2–56.6 Ma) with a relatively constant sedimentation rate of ~18 m/Myr. In this and a previous study, a total of 450 unoriented samples were studied for rock-magnetic properties by means of isothermal remanent magnetization (IRM) acquisition in 0.1 T and 1.0 T inducing fields, $IRM_{1.0/0.1T}$ ratio, thermal and AF demagnetization of a three component IRM, and hysteresis experiments. We found a pronounced increase in the relative proportion of the high coercivity hematitic component of the sediments (associated with maghemite) between ~54.9 and 54.6 Ma immediately above the Paleocene–Eocene boundary interval followed by a second, long-term

increasing trend from ~54 Ma up to ~52.2 Ma in the early Eocene. The hematitic component is of detrital origin and is interpreted to have formed on land by the weathering of Fe-bearing silicates and other primary minerals under warm and humid conditions. We speculate that the warm and humid climate typical of the Paleocene–Eocene thermal maximum (PETM, ~54.9 Ma) as well as of the early Eocene warming trend leading to the Early Eocene climatic optimum (EECO; ~52–50 Ma) enhanced continental weathering of silicate rocks with the consequent production, transport, and sedimentation of hematite-maghemite grains. This hypothesis is confirmed by a clear correlation between the rock-magnetic properties and global climate as revealed by a standard benthic oxygen isotope record from the literature. Our temporal coupling between oxidation state of sedimentary magnetic phases and global climate therefore is consistent with the existence in the Paleocene–Eocene of the silicate weathering negative feedback mechanism for the long-term stabilization of the Earth's surfaces temperature as proposed by various authors.

Keywords: Paleocene; Eocene; global warming; continental weathering; magnetic properties; magnetostratigraphy.

6.1 Introduction

During the Cenozoic, Earth's climate experienced a significant long-term evolution, evolving from non-glacial states, with virtually no ice at sea level, to polar-glacial conditions (e.g., Zachos et al., 2001, Miller et al. 2005). The late Paleocene–early Eocene was characterized by a global warming trend that eventually culminated with the early

Eocene climatic optimum (EECO, ~52–50 Ma). The EECO was characterized by warm climatic conditions even at extremely high latitudes (McKenna, 1980; Moran et al., 2006); Atlantic bottom waters reached temperatures of 14 °C, as indicated by oxygen stable isotope data (Zachos et al., 2001, Miller et al., 2005), and promoted the widespread deposition of silica (Muttoni and Kent, 2007). The late Paleocene–early Eocene warming trend was punctuated by several short-lived hyperthermal events (Cramer et al., 2003), the most prominent of which was the Paleocene–Eocene thermal maximum (PETM; e.g. Kennett and Stott, 1991). This transient global warming event is marked by a 2‰–4‰ global negative carbon isotope excursion (CIE; Kennett and Stott, 1991; Koch et al., 1992; Zachos et al., 2003) and extensive carbonate dissolution of deep-sea sediments (Zachos et al., 2005). The CIE was interpreted as an event of massive injection of light carbon into the ocean/atmosphere reservoir, the origin and triggering mechanisms of which are still a matter of debate (e.g., Dickens et al., 1995; Kent et al., 2003; Svensen et al., 2004; Cramer and Kent, 2005; Pagani et al., 2006). Existing records reveal that during the PETM, deep-sea temperatures increased by 5–6 °C in less than 10 Kyr (Kennett and Stott, 1991; Bralower et al., 1995; Thomas and Shackleton, 1996), whereas sea-surface temperatures increased by 8 °C at high latitudes (Kelly et al., 1996; Dingle et al., 1998; Thomas and Bralower, 1999; Pearson et al., 2001; Zachos et al., 2001). Both marine and continental PETM records registered an increase in climate humidity (Bolle and Adatte, 2001; Bowen et al., 2004), even at extreme high latitudes (Robert and Kennett, 1994), and a marked increase in seasonal precipitation (Schmitz and Pujalte, 2007). The PETM recovery was gradual and the total duration of the stable isotopic excursion is estimated

to be on the order of ~200 Kyr, although different authors proposed somewhat different timings (Giusberti et al., 2007; Röhl et al., 2007).

EECO and PETM warm and humid climates were probably related to high greenhouse gas concentrations. This is supported by the occurrence of high (albeit highly scattered) pCO_2 estimated values on the order of >1000 ppm at around the EECO (e.g., Yapp, 2004; Lowenstein and Demicco, 2006). The EECO long-term warmth ended at ~50 Ma in the early Eocene with the onset of a long-term cooling trend that continued over the ensuing middle–late Eocene and culminated with the inception of major Antarctic ice sheets at Oi-1 near the Eocene–Oligocene boundary at ~34 Ma (Miller et al., 1991; Zachos et al., 2001). This long-term cooling trend was probably due to a progressive decrease of greenhouse gas concentrations, as broadly indicated by generally low (<500 ppm) pCO_2 estimates after Oi-1 that followed a decline which more or less parallels the long-term temperature record (Pagani et al., 2005; Thomas, 2008). The long-term cooling was possibly caused by a perturbation of the long-term CO_2 input-output balance triggered by the collision of India with Asia at ~50 Ma (Kent and Muttoni, 2008).

EECO and PETM warm and humid climates should be characterized by enhanced land weathering rates, which would promote the sequestration of excess CO_2 by chemical weathering of silicates followed by the deposition of carbonates, in accordance with the negative feedback mechanism for the long-term stabilization of the Earth's surfaces temperature; this mechanism was originally proposed by Walker et al. (1981; see also Kump et al., 2000). Enhanced land weathering rates of Fe-bearing silicates should be accompanied by the production of Fe-oxides with high oxidation states as residuals of the weathering reactions. These Fe-oxides may be mobilized, transported, and deposited in

adjacent sedimentary basins by the accelerated hydrological cycle and enhanced runoff typical of the EECO and PETM warm and humid climates (Robert and Kennett, 1994; Sloan and Rea, 1995; Bolle and Adatte, 2001; Bowen et al., 2004).

In this paper, we present the rock-magnetic properties of upper Paleocene–lower Eocene marine pelagic sediments of the Cicogna section (Belluno Basin, Northern Italy). The magnetic properties of the sediments generally indicate an increase in abundance of detrital hematite during times of enhanced warming (i.e. PETM and early Eocene warming leading to EECO), as revealed by a statistical correlation with the benthic oxygen isotopes record of Zachos et al. (2001). The results seem to confirm the existence of the silicate-weathering machine (Walker et al. (1981) as a buffer of climate warming on both short (PETM) and long (EECO) time scale.

6.2 Geological setting

The Belluno Basin (Venetian Southern Alps, NE Italy) is a paleogeographic domain developed since the Early Jurassic, bounded to the West by the Trento Plateau and to the East by the Friuli Platform (Winterer and Bosellini, 1981; Castellarin and Cantelli, 2000; Zattin et al., 2006) (Fig. 6.1). The area of the Belluno Basin that is the object of this study is located in Valbelluna, where a succession of Cretaceous–early Eocene hemipelagic sediments up to 200–250 m in thickness crops out. These are mainly represented by well-bedded, pink to red limestones and marly limestones (Scaglia Rossa *sensu lato,* which includes local informal lithostratigraphic units; Di Napoli Alliata et al., 1970; Costa et al., 1996). The Paleocene–Eocene transition, described in several localities of the Belluno Basin domain (Arenillas et al., 1999; Agnini et al., 2006; Giusberti et al.,

2007), is well exposed in the Cicogna section; it coincides with the base of a ~3 m-thick package of mainly red marly clays and marls of lower Eocene age hereafter referred to as the clay marl unit (CMU). Giusberti et al. (2007) proposed that the CMU is likely related to the widespread acidification of the ocean waters (Zachos et al., 2005) and the associated dissolution of deep-sea carbonates that occurred during the PETM.

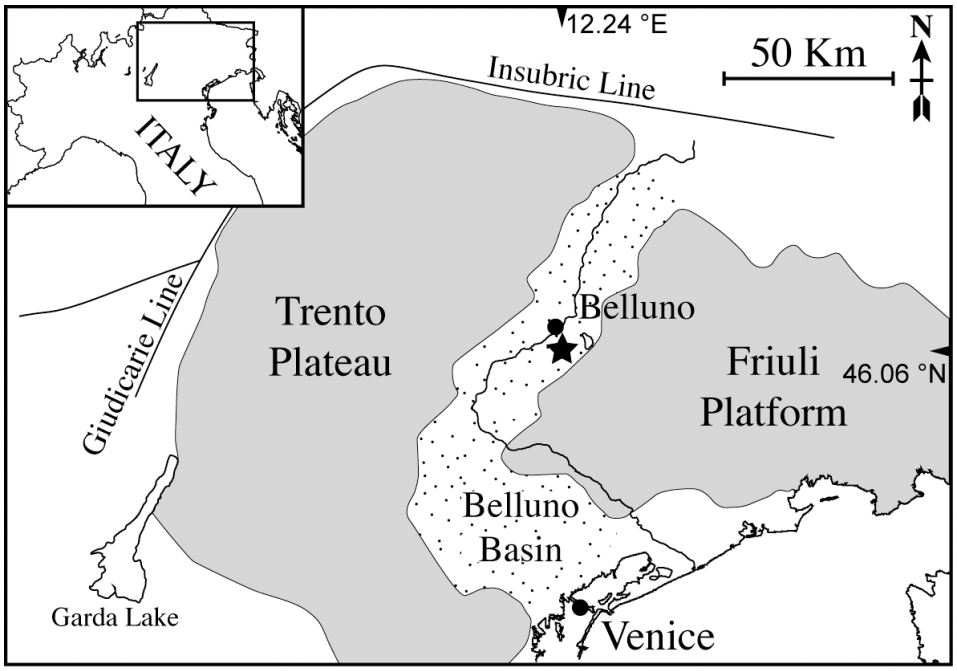

Figure 6.1. Main paleogeographic domains of the Venetian Southern Alps. The Cicogna section (indicated by the black star; Lat.= 46.06 °N; Long.= 12.24 °E) is located in the Belluno Basin, ~8 km to the south of the town of Belluno along the Cicogna riverbed.

6.2.1 The Cicogna section

The upper Paleocene–lower Eocene Cicogna section consists of ~81 m of marly limestones referred to as the Scaglia Rossa (*s.l.)* Formation (locally named *Marna della Vena d'Oro*) and is overlain by the siliciclastic deposits of the Belluno Flysch. The section extends in stratigraphic continuity from Chron C25r to Chron C23r and from

nannofossil Zone NP7/NP8 to NP12 (=CP6–CP10), thus covering an interval of time between ~56.6 and ~52.2 Ma according to the time scale of Berggren et al. (1995); inferred sediment accumulation rates were relatively constant, on the order of ~18 m/Myr (Dallanave et al., 2009) (Fig. 6.2). The basal ~15 m of the section are made of a rhythmic alternation of gray-greenish marly limestone-marl couplets; from ~15 to 20 m, the rhythmicity becomes progressively less apparent and the sediments are composed by pink-reddish marly limestones. The marly limestone sedimentation is abruptly interrupted at 28.7 m by the 3 m-thick CMU (Fig. 6.2A, B); the presence of the calcareous nannofossil excursion taxa indicates that the CMU at Cicogna is the lithological expression of the PETM (Dallanave et al., 2009). The base of the CMU is characterized by a ~2.5 cm-thick mottled gray-greenish and red clay level, overlain up to ~31.7 m by red marls flecked by rare greenish patches; two gray-greenish levels, ~0.1 and ~0.15 m-thick, respectively, were observed at the ~29.05 m and ~30.8 m levels (Fig. 6.2B). From the top of the CMU at 31.7 m upward, the Cicogna section is characterized by the re-occurrence of pink-reddish marly limestone-marl couplets persisting up to 39.2 m (Fig. 6.2A, B). From 39.2 m up to ~75.0 m (Fig. 6.2A) at the first significant occurrence of the siliciclastic material characterizing the overlying Belluno Flysch, the succession is dominated by red marls with no apparent rhythmicity and is characterized by the rare presence of gray-greenish levels or spots. From ~75 m to ~81 m, the Cicogna section is characterized by red marls alternating with siliciclastic layers, which become dominant from 81 m (formal base of the Belluno Flysch) upwards (Fig. 6.2A).

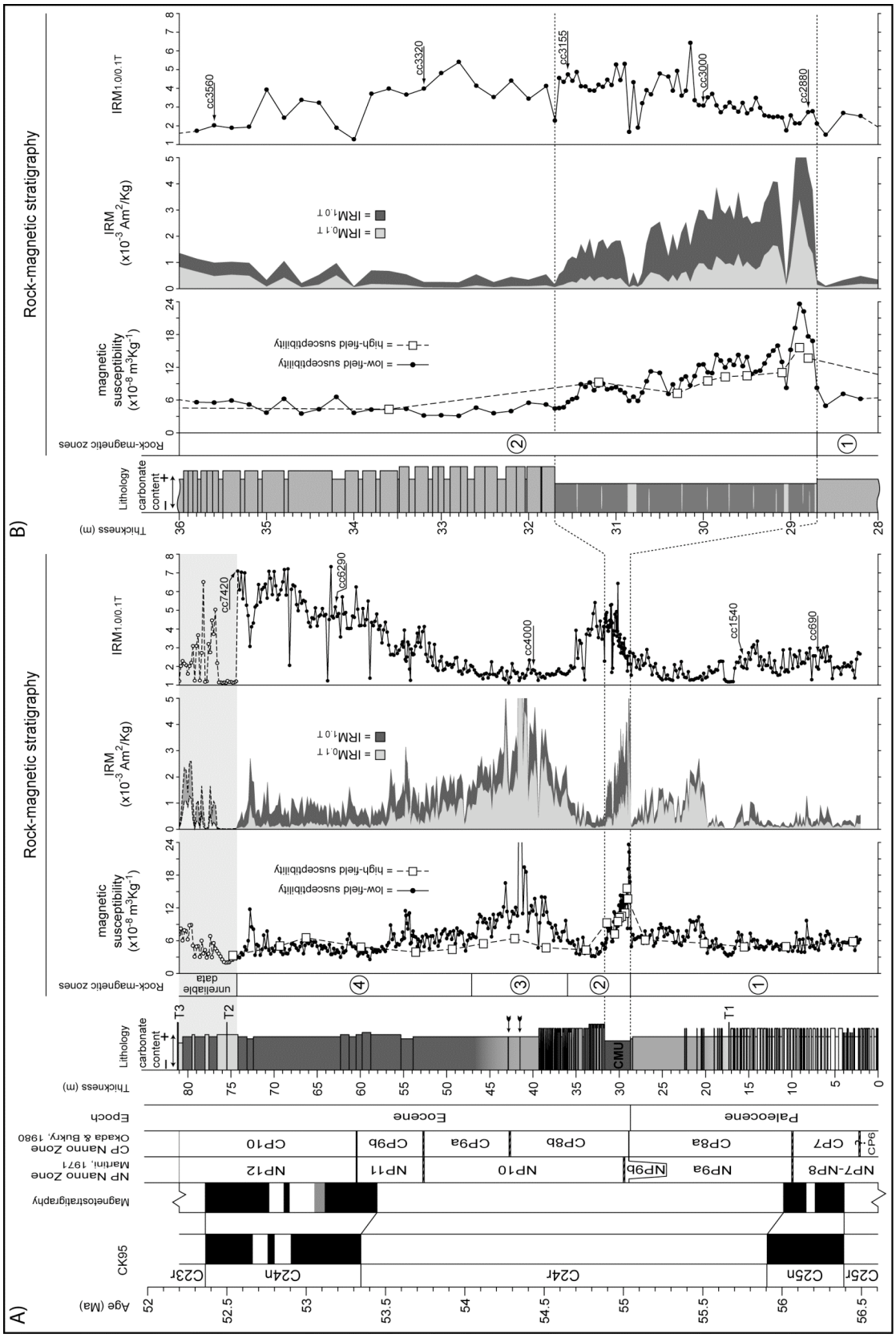
A)
B)
Rock-magnetic stratigraphy
Age (Ma)
CK95
Magnetostratigraphy
NP Nanno Zone
Martini, 1971
CP Nanno Zone
Okada & Bukry, 1980
Epoch
Paleocene
Eocene
C25r
C25n
C24r
C24n
C23r
NP7-NP8
NP9a
NP9b
NP10
NP11
NP12
CP7
CP8a
CP8b
CP9a
CP9b
CP10
CP6
Thickness (m)
Lithology
carbonate content
T1
T2
T3
CMU
Rock-magnetic zones
unreliable data
IRM
(x10-3 Am2/Kg)
= IRM0.1T
= IRM1.0T
magnetic susceptibility
(x10-8 m3Kg-1)
= low-field susceptibility
= high-field susceptibility
IRM1.0/0.1T
cc7420
cc6290
cc4000
cc1540
cc690
cc3560
cc3320
cc3155
cc3000
cc2880

Figure 6.2. A) The late Paleocene–early Eocene Cicogna section. Form left to right: chronological and magneto-biostratigraphical framework (for details see Dallanave et al., 2009); lithostratigraphic log of the section [T1 = Carbonate turbidite level; T2, T3= Sandy turbidite level; black arrows= calcite veins; CMU = clay marl unit]; rock-magnetic stratigraphy across the section, namely represented by the rock magnetic zones, the low- and high-field susceptibility, the IRMs at 0.1 T and 1.0 T ($IRM_{0.1\ T}$ and $IRM_{1.0\ T}$, respectively) and the ratio of these ($IRM_{1.0/0.1\ T}$). B) Detail of the magnetic properties of the Cicogna section between 28–36 m (i.e. from the top of rock-magnetic zone 1 to the top of the zone 2); see text for details.

6.3 Material and Methods

To define the magnetic properties of the sediments, Dallanave et al. (2009) collected a total of 450 samples every ~20 cm along the ~81 m of the Cicogna section, save for the ~300 cm-thick CMU, where 60 samples were collected every 5 cm. All the samples were weighed and the bulk susceptibility was measured with an AGICO KLY-3 Kappabridge. Samples were successively magnetized in 0.1 T and 1.0 T fields with an ASC Pulse Magnetizer and the values of the isothermal remanence magnetization ($IRM_{0.1\ T}$ and $IRM_{1.0\ T}$, respectively) were measured on a 2G DC-SQUID cryogenic magnetometer placed in a magnetic–shielded room at the Alpine Laboratory of Paleomagnetism (Cuneo, Italy) (Dallanave et al., 2009). To augment the definition of the magnetic properties of the sediments, a new set of 47 representative samples were magnetized in 2.5 T, 1.0 T, and 0.1 T along three orthogonal axes, and were successively subjected to alternating field (AF) demagnetization in 13 steps from 5 to 180 mT using a SI-4 specimen demagnetizer, with the resulting magnetization measured after each demagnetization step. After this procedure, the same samples plus 15 additional fresh samples were magnetized in the same orthogonal fields (2.5 T, 1.0 T, and 0.1 T), and subjected to thermal

demagnetization adopting 18 demagnetization steps from room temperature to 670 °C (Lowrie, 1990). Hysteresis parameters were also obtained with a MICROMAG alternating gradient force magnetometer on a selected suite of 23 ~0.02–0.03 gr samples. Values of saturation magnetization (Ms), saturation remanence (Mr) and coercivity (Bc) were determined from the hysteresis loops after correction for a paramagnetic component observed in all samples. The values of the high-field magnetic susceptibility were estimated by calculating the slope of the linear (post-closure) portion of the hysteresis loops. The values of the coercivity of remanence (Bcr) were estimated by calculating the parameter ΔM obtained by subtracting the ascending (0–1 T) branch of the hysteresis loop from the descending (1 T–0) branch of the loop, with Bcr approximated by the field value at ΔM = 50% (Tauxe, 2010). The AF and thermal demagnetization of the three orthogonal IRMs, and the hysteresis experiments were conducted at the paleomagnetic laboratory of the Scripps Institution of Oceanography (La Jolla, California).

6.4 Rock-magnetic data

We subdivided the Cicogna section into four main rock-magnetic zones (Figure 6.2; Table 6.1).

6.4.1 Rock-magnetic Zone 1 (0–28.7 m). The low-field and high-field magnetic susceptibility are characterized by relatively low and constant values (average of 5.9 and 5.5 $x10^{-8}$ m^3Kg^{-1}, respectively), reflecting the general control of paramagnetic minerals on bulk susceptibility (Fig. 6.2A; Tab. 6.1). The values of the low-field magnetic susceptibility show a marked negative swing in correspondence of the carbonate turbidite

layer at ~17 m and are slightly higher than average from ~20 m upwards, where the sediments turn from gray-greenish to pink-reddish in color.

Thermal demagnetization of the three component-IRM reveals that the gray-greenish sediments from the section base up to ~15 m are dominated by the soft 0.1 T magnetic coercivity phase that gradually decreases with temperature, approaching zero (or very low values) at 575 °C; we interpret this fraction as magnetite. Subsidiary 1.0 T and a minor 2.5 T coercivity phases that persist up to 670 °C are also present and are interpreted as hematite (Fig. 6.3A, e.g. sample cc690). From ~15 m up to the CMU base, where the sediments become pink-reddish in color, the thermal demagnetization of the three component-IRM shows a switch in the relative contributions to the IRM, whereby the 1.0 T becomes the dominant fraction and the 0.1 T fraction becomes of secondary importance. The 0.1 T fraction shows a smooth intensity decline up to ~670 °C consistent with the presence of maghemite, which typically possesses low coercivity and Curie temperatures between 590 and 675 °C (Tauxe, 2009). The 1.0 T curve shows instead an intensity reduction between 300 and 400 °C followed by a gentle but persistent further reduction up to 600 °C and by an abrupt final decrease to zero values up to ~670 °C (Fig. 6.3A, e.g. sample cc1540). We interpret this 1.0 T coercivity phase as hematite. The smooth decrease observed in the 1.0 T curve between 300 and 400 °C probably reflects the presence of minor amounts of maghemite that breaks down during heating in nearly zero magnetic field (e.g., Kodama, 1982; Wang et al., 2003). This maghemite, picked up by the 1.0 T curve, possibly represents the surface coating of magnetite grains because these mixed grains can possess much higher coercivities than those of pure magnetite or

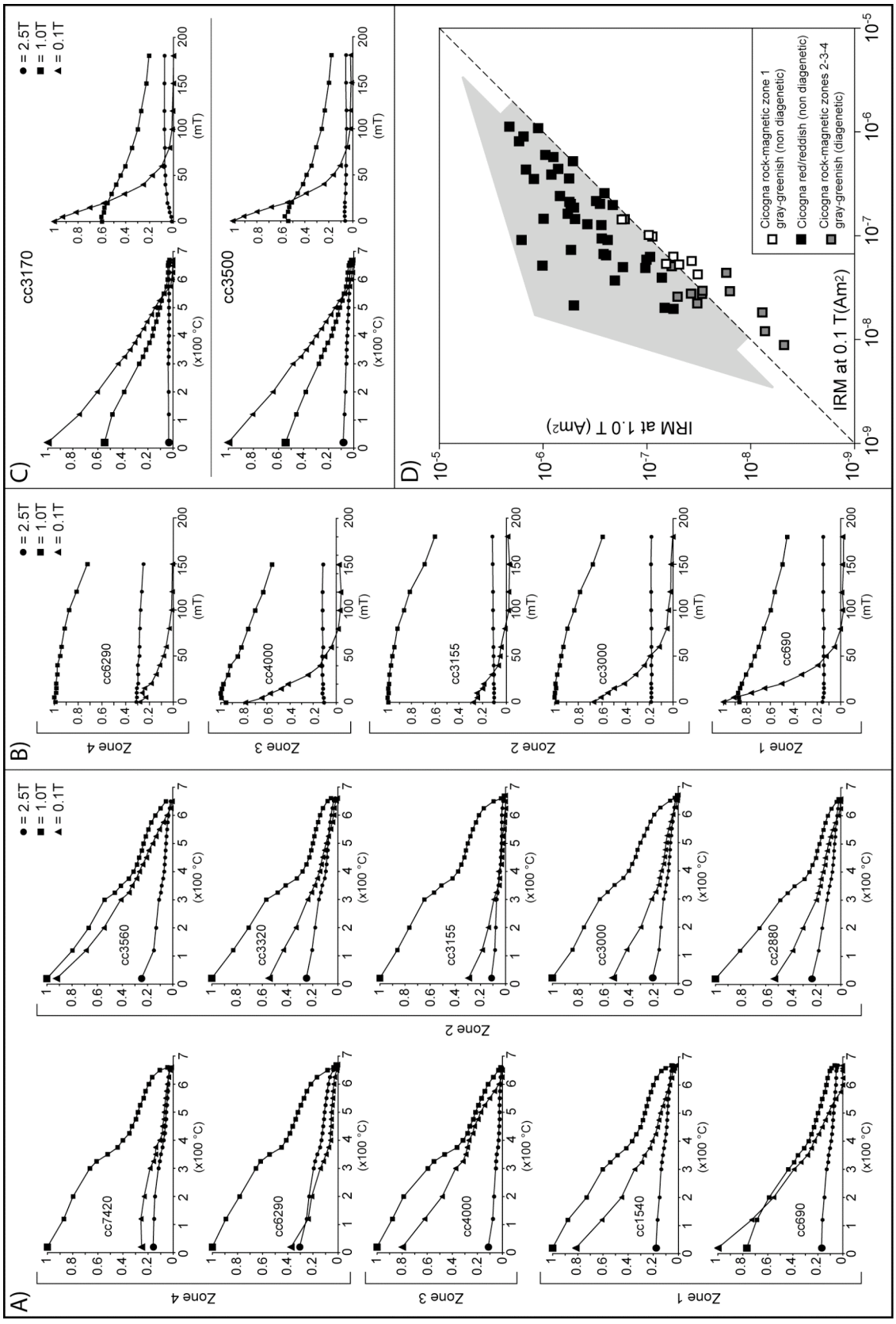
A)
B)
C)
D)
Zone 4
Zone 3
Zone 2
Zone 1
cc7420
cc6290
cc4000
cc1540
cc690
cc3560
cc3320
cc3155
cc3000
cc2880
cc6290
cc4000
cc3155
cc3000
cc690
cc3170
cc3500
● = 2.5T
■ = 1.0T
▲ = 0.1T
(x100 °C)
(mT)
IRM at 1.0 T (Am²)
IRM at 0.1 T(Am²)
Cicogna rock-magnetic zone 1 gray-greenish (non diagenetic)
Cicogna red/reddish (non diagenetic)
Cicogna rock-magnetic zones 2-3-4 gray-greenish (diagenetic)

Figure 6.3. A) Representative thermal demagnetization data of a three component IRM of samples from the Cicogna section; the stratigraphic position of the illustrated samples is indicated in Fig. 6.2A and B. B) Representative alternating field (AF) demagnetization data of three component IRM of samples from each rock-magnetic zone of the Cicogna section; the correlative thermal demagnetization diagrams are shown in Fig. 6.3A; the stratigraphic position is indicated in Fig. 6.2A and B. C) Thermal (right) and AF (left) demagnetization of three orthogonal IRMs of two representative samples collected from the gray-greenish spots in rock-magnetic zone 2 at 31.7 m (cc31700) and 35.0 m (cc3500), respectively. D) Logarithmic plot of IRMs at 1.0 T and 0.1 T of the thermally demagnetized representative samples; the gray–greenish samples collected from the levels and spots of rock-magnetic zones 2, 3 and 4 display generally the lowest values; the gray arrow mark the increase in the IRM at 1.0 T of the samples. See text for details.

maghemite (Van Velzen and Dekkers, 1999). Finally, the minor 2.5 T fraction shows maximum unblocking temperature of 670 °C typical of hematite.

AF demagnetization of samples from rock-magnetic zone 1 reveals that the low coercivity (0.1 T) component (i.e. pure magnetite or maghemite) is characterized by a virtually total (100%) drop of intensity by peak fields of 100 mT, while the mid coercivity (1.0 T) component (essentially hematite) drops by ~50% in fields of ~180 mT. AF demagnetization has no appreciable effect on the high coercivity (2.5 T) component (hematite) (Fig. 6.3B, e.g. sample cc690).

We used the $IRM_{0.1\ T}$ and $IRM_{1.0\ T}$ values measured in all the 450 samples to monitor the relative amount of ferromagnetic minerals along the section. In rock-magnetic zone 1, low values (= low relative concentration of ferromagnetic minerals) characterize the basal ~20 m of the section, followed by higher values up to the CMU base at ~28.7 m where the pink-reddish marls enriched in ferromagnetic minerals replace the marly limestone-

marl couplets (Fig. 6.2A). The $IRM_{1.0/0.1T}$ ratio, used to monitor the contrasting coercivity variations along the section, is characterized by low values around 2 reflecting a low contribution of the high coercivity (1.0 T) minerals (essentially hematite) relative to low coercivity (0.1 T) minerals (pure magnetite or maghemite). All parameters show a swing toward lower values within the carbonate turbidite layer at ~17 m (Fig. 6.2A).

Hysteresis loops show that samples from rock-magnetic zone 1 are dominated by a paramagnetic component; after paramagnetic correction, the loops appear very narrow in shape at the section base (Fig. 6.4, e.g. sample cc290). The measured Mr/Ms ratio of the samples collected in the gray-greenish basal ~15 m of the section is markedly lower compared to the overall distribution of the pink-reddish to red samples, as observed for a reference distribution data obtained from magnetite-bearing limestones (Channell and McCabe, 1994) (Fig. 6.5). From ~15 m up to the CMU base, the loops become wasp-waisted in shape, confirming the presence of distinct magnetic coercivity phases (e.g. Channell and McCabe, 1994; Muttoni, 1995; Roberts et al., 1995; Tauxe et al., 1996) (Fig. 6.4, e.g. sample cc1540, cc2680).

In summary, rock-magnetic zone 1 contains magnetite in the first gray-greenish ~15 m, coexisting with subsidiary hematite; from ~15 m up to the zone top, where sediments progressively become pink-reddish in color, the magnetic mineralogy is dominated by hematite coexisting with pure maghemite (and some maghemite-coated grains).

6.4.2 Rock-magnetic Zone 2 (28.7–36 m). At the CMU base (base of rock-magnetic zone 2), the low-field magnetic susceptibility values rise, peaking at 28.9 m, i.e. ~0.2 m above the zone base. The high-field susceptibility rises as well, but is consistently lower than the low-field susceptibility, indicating a main contribution of the ferromagnetic (*s.l.*)

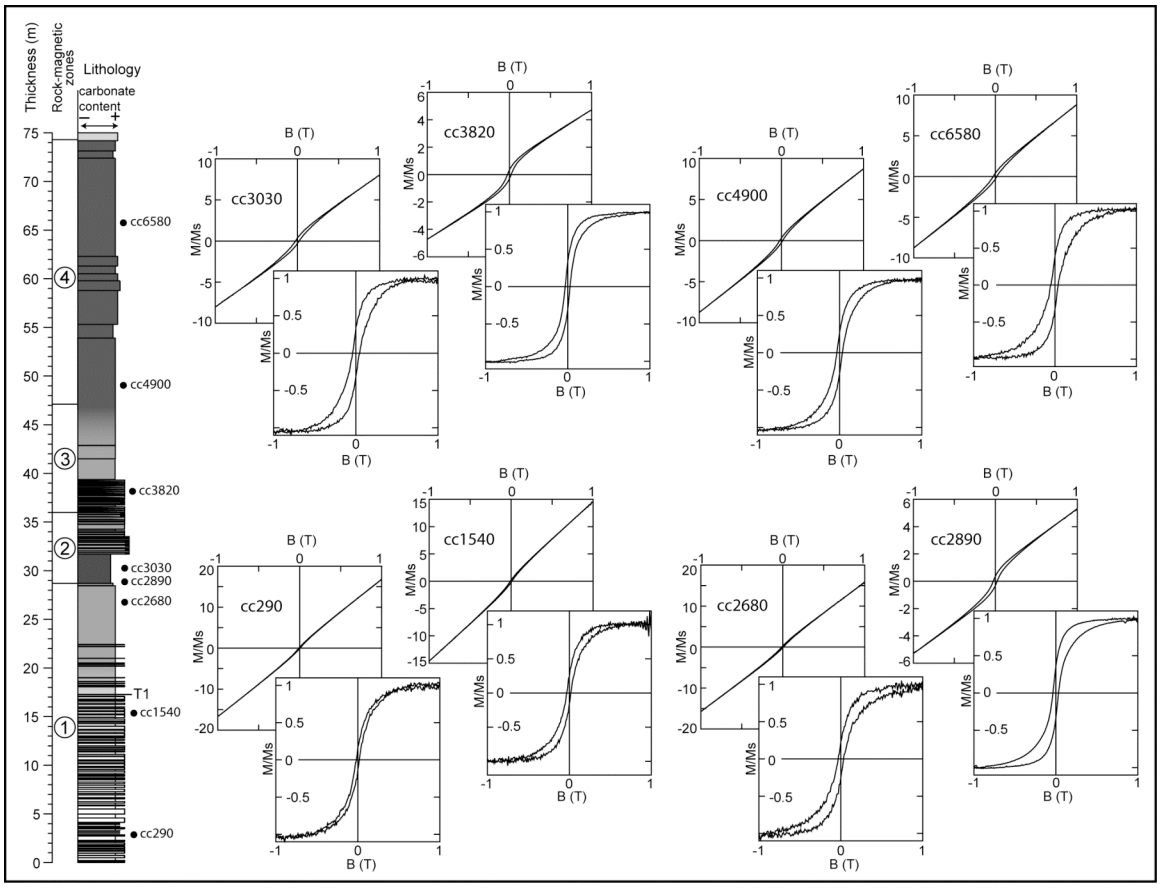

Figure 6.4. Hysteresis loops of representative samples from the Cicogna section with indication of stratigraphic position; the background and the foreground diagrams represent the loops before and after paramagnetic correction, respectively; the vertical axes of the diagrams represent the magnetization/saturation magnetization (M/Ms) ratio, while the horizontal axes the applied field (B) expressed in Tesla (T).

minerals in the lower part of the CMU (Fig. 6.2A, B). Above CMU peak values, low- and high- field susceptibility display a general decreasing trend, with two negative swings correlated with the gray-greenish levels observed at ~29 m and ~30.8 m.

Thermal demagnetization data of the three component-IRMs are generally dominated by the 1.0 T magnetic coercivity phase with maximum unblocking temperatures of ~670

°C, interpreted as hematite (coexisting with maghemite-coated grains as described above and revealed by the intensity loss at 300–400 °C; Fig. 6.3A, zone 2 samples). Samples from rock-magnetic zone 2 contain also a significant contribution from the 0.1 and 2.5 T coercivity fractions. The soft 0.1 T fraction smoothly decreases up to maximum unblocking temperatures of ~650 °C and is interpreted as pure maghemite, whereas the hard 2.5 T fraction has maximum unblocking temperatures of ~670 °C and is interpreted as hematite. From the middle part of rock-magnetic zone 2 up to the CMU top, the contribution of the 1.0 T component rises at the expenses of the 0.1 T component (while the 2.5 T component remains broadly constant) (Fig. 6.3A, Zone 2 samples). This datum is interpreted to indicate a progressive increase of the hematite content of the samples from the middle part of rock-magnetic zone 2 up to the CMU top. In samples from the rare gray-greenish levels and spots (of diagenetic origin, see below) scattered within rock-magnetic zone 2, the low (0.1 T) coercivity phase dominates; this phase approaches zero value at 575 °C and is therefore interpreted as magnetite (Fig. 6.3C, *e.g.* samples cc3170, cc3500).

AF demagnetization shows that the 1.0 T coercivity phase dominating in the red samples experiences a ~30% intensity decrease up to fields of ~180 mT (Fig. 6.3B), whereas the more rare gray-greenish samples show higher relative contributions from the 0.1 T phase that is demagnetized at fields of ~100 mT (Fig. 6.3C).

The $IRM_{0.1\ T}$ and the $IRM_{1.0\ T}$ data generally follow the pattern of the magnetic susceptibility, with peak values at the CMU base and a decreasing trend over the ensuing part of the CMU, interrupted by two marked shifts towards lower values that are associated with the gray-greenish levels at ~29 m and ~30.8 m. Over the top of the CMU,

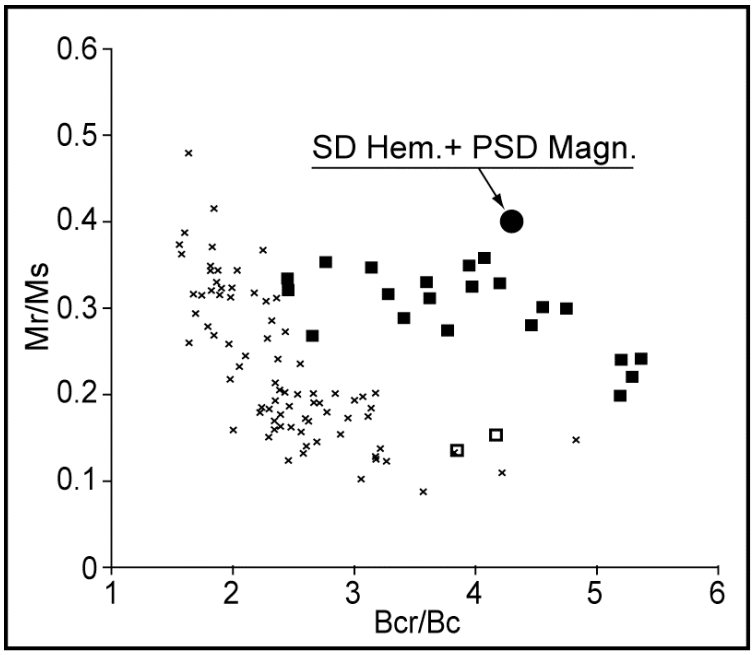

Figure 6.5. Plot of Mr/Ms versus Bcr/Bc (Mr= remanent magnetization; Ms= saturation magnetization; Bcr= coercivity of remanence; Bc= magnetic coercivity) of samples from the Cicogna section; open squares refer to gray-greenish samples collected in the first ~15 m of the rock-magnetic zone 1; black squares refer to pink-reddish to red samples collected from ~15 m upsection. The Cicogna samples distribution is compared to a reference distribution of hysteresis parameters (black crosses) obtained for magnetite-bearing (i.e. low coercivity) limestones from the literature (Channell and McCabe, 1994). The black circle indicates the reference value for a PSD magnetite-SD hematite mixture of Roberts et al. (1995). See text for details.

the IRM values remain relatively low and stable, and start increasing again from ~36 at the top of rock-magnetic zone 2 upward (Fig. 6.2A, B). In contrast, the $IRM_{1.0/0.1T}$ ratio (which can be regarded as a proxy of the hematite fraction concentration relative to pure maghemite) shows a gradual increasing trend starting from the CMU onset, peaking at ~30.2 m and remaining relatively high and stable over the ensuing part of the CMU. Above the CMU, the values gradually decrease, reaching pre-CMU values toward the top

of rock-magnetic zone 2 (Fig. 6.2A, B); this trend allows us to better define the spatial range of the hematite increase (relative to pure maghemite) observed in the thermal and AF demagnetization of the three orthogonal IRMs.

The hysteresis loops display generally wasp-waisted shapes, confirming the coexistence of distinct coercivity magnetic phases, as for the pink-reddish samples already described for rock-magnetic zone 1, but with a paramagnetic contribution significantly lower (Fig. 6.4, samples cc2890, cc3030); the presence of distinct magnetic coercivity phases is also reflected in the hysteresis parameters distribution (Fig. 6.5), which approaches the reference value for a PSD (pseudo-single domain) magnetite-SD (single domain) hematite mixture of Roberts et al. (1995).

In summary, a mixture of hematite and pure maghemite dominates the reddish to red sediments of rock-magnetic zone 2 (with the ubiquitous presence of some maghemite-coated grains). The data reveal an increasing trend of the hematite content from the CMU onset, which peaks at ~30.2 m; this is followed by a decline to pre-CMU values attained at the top of rock-magnetic zone 2, where the hematite and maghemite contributions to the IRM become again broadly equal. In the rare gray-greenish levels and spots observed within rock-magnetic zone 2 (of diagenetic origin, see below), maghemite is replaced by magnetite.

6.4.3 Rock-magnetic Zone 3 (36–47 m). From ~36 m upsection, the low-field susceptibility values rise, peaking at ~42 m where carbonate dissolution surfaces were observed (Fig. 6.2A); the susceptibility then gradually decreases, reaching relatively low and stable values from ~57 m up to the section top. The high-field susceptibility values

are constantly lower than low-field values, which we interpret as due to the presence of dominant ferromagnetic (*s.l.*) particles (Fig. 6.2A).

Thermal demagnetization data of the three component-IRMs show that the samples from rock-magnetic zone 3 contain broadly equal proportions of a 1.0 T phase characterized by maximum unblocking temperatures of ~670 °C (and the usual loss of magnetization at 300–400 °C), and of a 0.1 T phase smoothly decreasing to zero at ~650 °C (Fig. 6.3A, *e.g.* sample cc4000). This association is interpreted as due to the presence of broadly equal amounts of hematite and pure maghemite (with subsidiary amounts of maghemite-coated grains).

AF demagnetization data reveal coercivity spectra similar to those observed for the pink-reddish samples of rock-magnetic zone 1 and 2, whereby the low coercivity (0.1 T) component is removed after AF treatment up to fields of 100 mT and the mid coercivity (1.0 T) component shows a ~40% drop of intensity up to fields of ~150 mT. As expected, the AF demagnetization has no noticeable influence on the high (2.5 T) coercivity component (Fig. 6.3B, e.g. sample cc4000).

The $IRM_{0.1\ T}$ and the $IRM_{1.0\ T}$ data show patterns that tightly follow the low-field susceptibility trend. The $IRM_{1.0/0.1T}$ ratio displays relatively low values across the entire rock-magnetic zone 3, confirming the approximately equal contribution of pure maghemite and hematite phases previously observed in the thermal and AF demagnetization diagrams.

Hysteresis loops are slightly wasp-waisted in shape. This is attributed to the coexistence of hematite and pure maghemite with contrasting coercivities (Fig. 6.4, sample cc3820). Accordingly, the hysteresis parameters distribution approaches the

reference value for a PSD magnetite-SD hematite mixture (Roberts et al., 1995) (Fig. 6.5).

In summary, these data indicate the presence in samples from the reddish sediments of rock-magnetic zone 3 of broadly equal amounts of hematite and pure maghemite (with the ubiquitous presence of some maghemite-coated grains).

6.4.4 Rock-magnetic Zone 4 (47–74 m). In this zone, dominantly red in color, the low-field susceptibility shows a gradual decrease ending at ~57 m, followed by relatively stable values up to the zone top; the high-field susceptibility displays relatively low values across the entire zone, matching the low-field susceptibility data well.

The three component-IRMs thermal demagnetization data reveal that the sediments are dominated by the 1.0 T coercivity phase, which displays the typical decrease to zero values at ~670 °C interpreted as due to hematite (preceded by the usual loss at 300–400 °C possibly due to maghemite-coated grains); minor amounts of pure maghemite are also present as revealed by the 0.1 T curve smoothly approaching zero at ~650–670 °C (Fig 6.3A, *e.g.*, samples cc6290 and cc7420).

The AF demagnetization diagrams show that the 0.1 T coercivity component is removed after AF treatment up to fields of 100 mT, the mid coercivity (1.0 T) component shows a ~25% drop of intensity up to fields of ~150 mT, whereas the AF demagnetization has no effect on the 2.5 T coercivity component (Fig. 6.3B, *e.g.* sample cc6290).

The $IRM_{0.1\ T}$ and the $IRM_{1.0\ T}$ data show the same pattern of the low-field susceptibility, punctuated by discrete swings to higher values related to more marly layers (*e.g.*, at ~55 m, ~57 m, and ~73 m; Fig. 6.2A). The $IRM_{1.0/0.1T}$ ratio starts an increasing

trend from approximately 46 m upward; based on the thermal and AF demagnetization data described above, we interpret this trend as due to a progressive increase of the hematite amount upward. From ~74 m on, the presence of sandy turbidites complicates the magnetic signal, and $IRM_{1.0/0.1T}$ ratio can no longer be taken as representative of the relative hematite content of the sediments.

Hysteresis loops are typically wasp-waisted in shape, and this characteristic is more pronounced moving upsection (Fig. 6.4, *e.g.* samples cc4900, cc6580). The Mr/Ms ratios approach the reference value for a PSD magnetite-SD hematite mixture (Fig. 6.5). This indicates the presence of distinct coercivity phases.

In summary, rock-magnetic zone 4 is characterized by dominant hematite and subsidiary pure maghemite (with the ubiquitous presence of some maghemite-coated grains). The $IRM_{1.0/0.1T}$ ratio shows an increasing trend from ~46 m upsection that is interpreted to reflect a gradual increase of the hematite content in the hematite-maghemite system.

6.4.5 Summary of the rock-magnetic data. The analyses reveal that the magnetic mineralogy of the gray-greenish samples collected in the basal ~15 m of rock-magnetic zone 1 is dominated by magnetite, which coexists with subsidiary hematite. This magnetite is regarded as primary (syndepositional) in origin as it carries a primary paleomagnetic signal bearing polarity reversals (Dallanave et al., 2009) retrieved in sediments devoid of sedimentological evidence of diagenetic reduction, although an origin during early diagenesis cannot be excluded.

The pink-reddish to red sediments observed from ~15 m upward are interpreted to be dominated by a mixture of hematite and pure maghemite in different relative proportion

varying along the section. In particular, as revealed by the $IRM_{1.0/0.1T}$ ratio, increased relative amounts of hematite are observed across the rock-magnetic zone 2 (i.e. between 28.7–36 m) and generally from ~46 m upsection, in rock-magnetic zone 4. The characteristic directions of the pink-reddish to red part of the Cicogna section are carried by detrital hematite (Dallanave et al., 2009). The detrital origin of the hematite particles is well documented by an inclination shallowing of the characteristic directions, which was detected and corrected using the elongation/inclination (E/I) method of Tauxe and Kent (2004; see also Tauxe et al., 2008). The inclination error is expressed by the "*f*" parameter first introduced by King (1955) by the formula $\tan(I_0) = f \bullet \tan(I_f)$, where I_0 is the measured inclination and I_f is the real inclination of the inducing field. For the Cicogna sediments, the value of "f" was found to be 0.4 (Dallanave et al., 2009), same as that measured for naturally deposited river sediments whose remanence was carried by detrital hematite (Tauxe and Kent, 1984). Finally, this variable hematite-pure maghemite mixture of detrital origin seems to coexist with ubiquitous, subsidiary amounts of high coercivity maghemite-coated grains possibly reflecting partial maghemitization of former magnetite grains.

The magnetic mineralogy of the gray-greenish samples from the scattered levels and spots within mainly red-colored zones 2, 3, and 4 is dominated by magnetite, as revealed by the presence of a low (0.1 T) coercivity component with maximum unblocking temperature of 575 °C (Fig. 6.3C). The usual hematite-maghemite mixture described above characterizes instead the red sediments immediately surrounding the magnetite-bearing gray-greenish spots (Fig. 6.3A). Moreover, the overall IRM intensity of the gray-greenish spots is approximately one order of magnitude lower than that of the

surrounding red sediments (Fig. 6.3D). Considering the above, we interpret the magnetite of these gray-greenish levels and spots as derived by the diagenetic conversion of primary maghemite to magnetite under reducing conditions (e.g. Özdemir and Dunlop, 1988). Under such conditions, the newly formed magnetite can be readily dissolved (Fischer et al., 2007), as revealed by the IRM intensity decrease.

6.5 Cicogna age model

To place the magnetic variability onto a reference timescale, we improved the age model of Dallanave et al. (2009), which was constructed by means of magnetostratigraphic correlation with the CK95 geomagnetic polarity time scale of Cande and Kent (1995). We adopted a total of 7 magnetic reversals as chronologic control points, identified between the base of Chron C25n and the top of Chron C24r (Fig. 6.6). In our improved age model, we did not include the younger boundary of subchron C24n.3n as a chronologic tie-point because its position in the Cicogna section is poorly resolved. As an additional tie-point, we use the base of the CMU. Previous studies have indicated that the CMU base coincides with the Paleocene–Eocene boundary in several sections of the Belluno basin (see Agnini et al., 2006, 2007; Giusberti et al., 2007; Dallanave et al., 2009). The CMU base in the Forada section coincides with a $\delta^{13}C$ negative shift of 2.35‰ (Giusberti et al., 2007). Based on these arguments, we attribute an age of 54.95 Ma to the CMU base (Fig. 6.6), which is the age of the base of the correlative global negative $\delta^{13}C$ excursion adopted by Zachos et al. (2001). Furthermore, Giusberti et al. (2007) interpreted the radiolarian, biogenic carbonate, and carbon isotope

records across the Forada CMU as controlled by precessional forcing, and estimated a duration for the CMU of 105 Kyr, which we adopt also for the nearby Cicogna CMU.

The Cicogna age model based on the 9 chronologic tie-points described above implies a relatively constant average sediment accumulation rates of ~18 m/Myr, save for the 3 m-thick CMU where the sedimentation reaches up to ~29 m/Myr (Fig. 6.6).

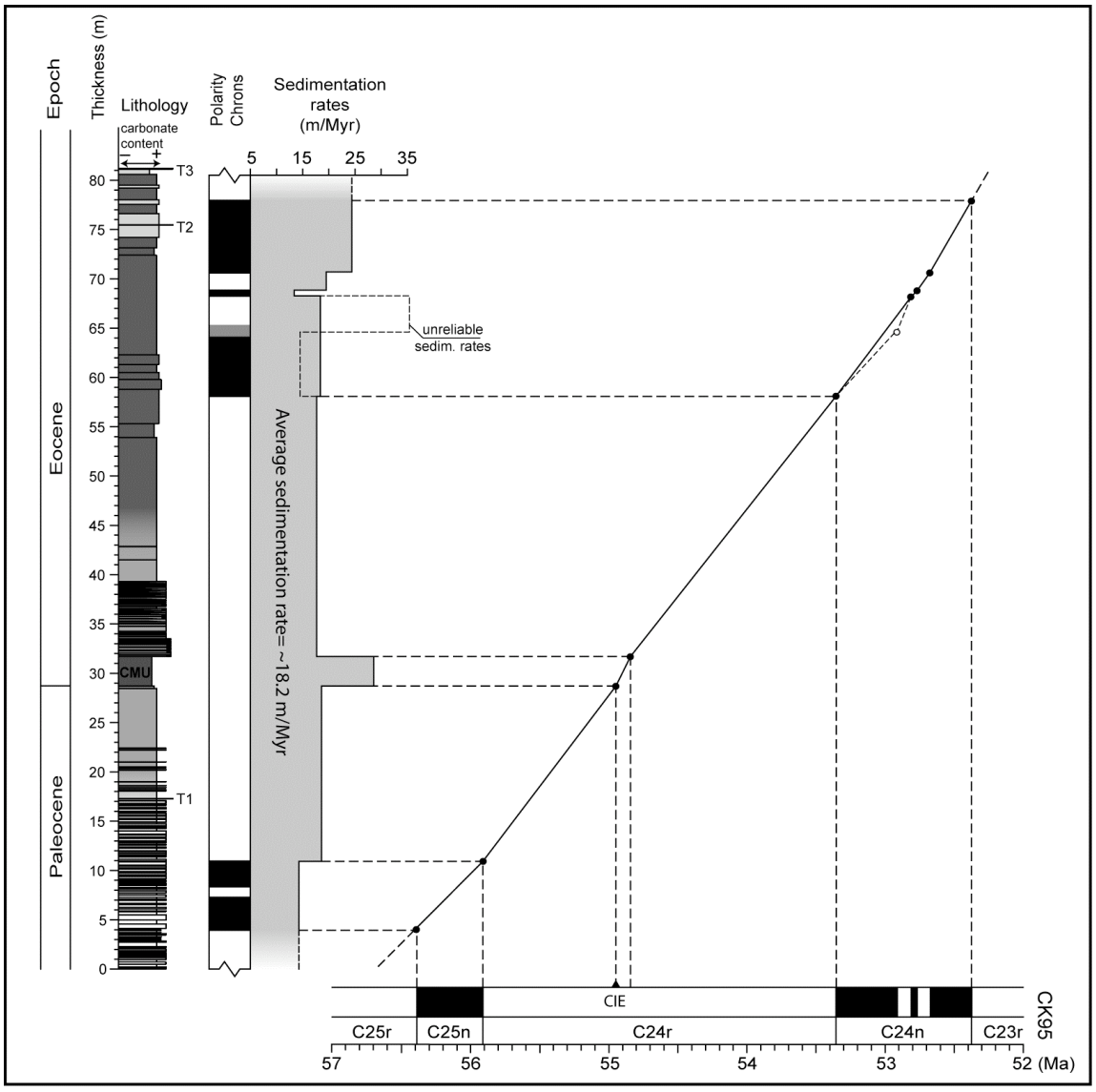

Figure 6.6. Age-depth model and derived sediments accumulation rates for the Cicogna section obtained by magnetostratigraphic correlation to the CK95 geomagnetic polarity time scale of Cande and Kent (1995).

We improved the age model previously published by Dallanave et al. (2009) dating the clay marl unit (CMU) 54.95 Ma by correlation to the global carbon isotopes excursion (CIE); we furthermore attributed the duration of 105 Kyr to the CMU. See text for a details.

6.6 Climate forcing on sedimentation

The most interesting feature of the rock magnetic record from Cicogna is the stratigraphic evolution of the magnetic coercivity spectra of the sediments, in particular the $IRM_{1.0/0.1T}$ ratio. This is close to 1 in strata bearing dominant low coercivity phases (i.e. magnetite and/or pure maghemite), and rises when the relative content of the high coercivity phase (essentially detrital hematite) becomes dominant. In particular, the $IRM_{1.0/0.1T}$ curve shows a positive swing between ~54.9–54.6 Ma and a gradual increasing trend from ~54 Ma up to 52.5 Ma, both due to increased relative amounts of detrital Fe^{3+} bearing minerals (in particular hematite). The rock-magnetic and paleomagnetic properties revealed that this signal is primary in origin, save for those low values linked to sparse and diagenetically reduced gray-greenish spots and levels discussed above. Acknowledging also that the average sedimentation rate of ~18 m/Myr does not show major changes along the section (save for the 3 m-thick CMU), we can argue that these variations are due to changes in the chemical processes at the source of the sediments (i.e. they are not artifacts of variable concentration due to sedimentation rate variations). In particular, we speculate that global climate change over the ~4.2 Myr time span of the Cicogna section played a fundamental role in the formation, transport, and subsequent sedimentation of the observed magnetic iron oxides.

Several climate proxies indicate that the late Paleocene-early Eocene was

characterized by warm and humid climate conditions (Zachos et al., 2001; Miller et al., 2005) that sustained an enhanced hydrological cycle (Robert and Kennett, 1994; Sloan and Rea, 1995; Bolle and Adatte, 2001; Bowen et al., 2004). Schmitz and Pujalte (2007) described geological evidence of increased intra-annual humidity and enhanced seasonality of the hydrological cycle during the PETM in sections from the south-central Pyrenees (Spain); these were located at subtropical paleolatitudes (~35° N) similar to the paleolatitude calculated for the Cicogna section after correction for shallow-bias (~34° N; Dallanave et al., 2009). These climate conditions likely promoted continental weathering whereby runoff and temperature are the main parameters controlling chemical weathering rate (and derived carbon dioxide consumption) of silicate rocks (e.g., Dessert et al., 2003). Hematite (α-Fe_2O_3) and maghemite (γ-Fe_2O_3) are common products of silicate weathering as they are formed by the weathering of Fe-bearing primary minerals such as pyroxene, amphibole, biotite, and olivine (Schwertmann, 2008). Torrent et al. (2006) demonstrated the existence of a ferrihydrite–maghemite–hematite pathway of weathering oxidation in continental environments under aerobic conditions.

To investigate the assumed relationship between rock-magnetic variability and global climate, we correlate the $IRM_{1.0/0.1T}$ curve to the late Paleocene–early Eocene benthic $\delta^{18}O$ record of Zachos et al. (2001), and observe a robust coherence between the two records, whereby the higher the $IRM_{1.0/0.1T}$ values, the lower the correlative $\delta^{18}O$ values (Fig. 6.7). Higher $IRM_{1.0/0.1T}$ ratios typical of red sediments enriched in primary hematite (relative to magnetite or pure maghemite) correspond to the warm climate conditions of the PETM as well as the warming trend leading to the EECO, whereas

lower ratios typical of sediments with lower relative amounts of hematite correlate with relatively cooler climate conditions, for example in the late Paleocene.

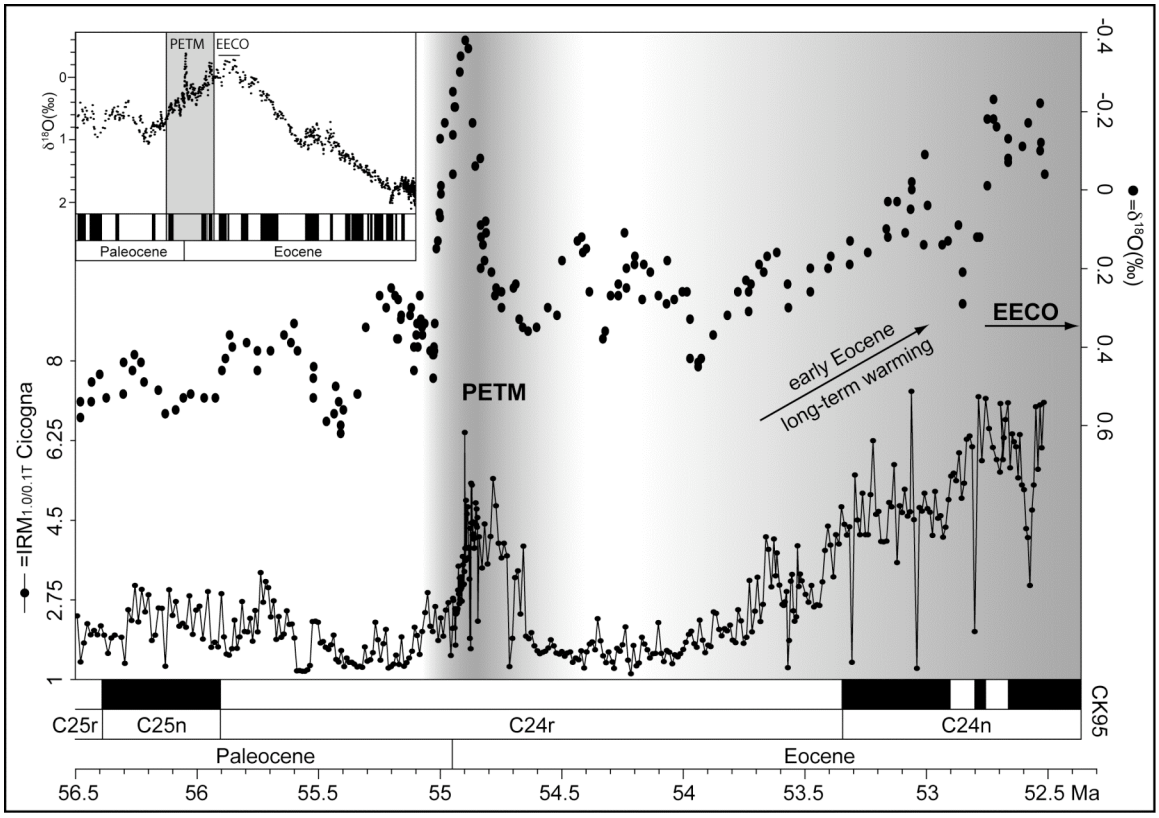

Figure 6.7. The Cicogna $IRM_{1.0/0.1T}$ dataset compared with the $\delta^{18}O$ record of Zachos et al. (2001) across the late Paleocene–early Eocene. Both datasets are placed onto the same timescale (CK95; Cande and Kent, 1995). The inset shows the $\delta^{18}O$ curve up to the Eocene–Oligocene boundary with indication (gray band) of the time interval spanned by the Cicogna section. See text for details.

To assess the robustness of the correlation between the $IRM_{1.0/0.1T}$ and the $\delta^{18}O$ time series we used the coherence function, which is the generalization of the correlation coefficient to the frequency domain. The range of frequencies for which the $IRM_{1.0/0.1T}$ data are coherent with the paleotemperatures proxy is readily visible from the plot of the squared coherence between the two dataset (Tauxe and Wu, 1990). We assigned a

squared coherence minimum value of 0.038 as 95% level of confidence, calculated using the relation given by Chave and Filloux (1985). As shown in Figure 6.8, the two records show coherence over the 0–6.3 Myr^{-1} range of frequencies, as well as between 10.6 – 11.3 Myr^{-1}; the highest values of squared coherence is reached at the 0 frequency, which implies a linear correlation between the two dataset along the ~4 Myr duration of the time series. The second peak of the squared coherence at the 4.75 Myr^{-1} frequency corresponds to the correlation along a wavelength of ~210 Kyr, which is approximately the duration of the oxygen isotopes excursion that occurred during the PETM. This statistical approach confirms both the long-term and the short-term correlation between the $IRM_{1.0/0.1T}$ and the $\delta^{18}O$ datasets.

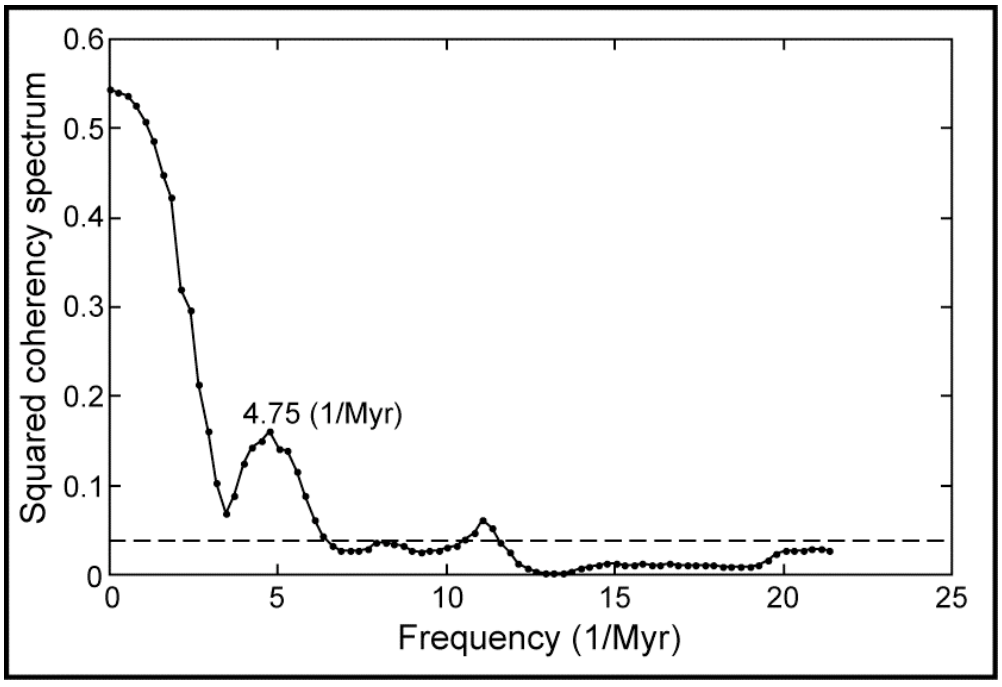

Figure 6.8. Squared coherence between the $IRM_{1.0/0.1T}$ magnetic parameter and the $\delta^{18}O$ record of Zachos et al. (2001); the dashed line represent the 95% confidence level. See text for details.

We believe that the tight temporal coupling between rock-magnetic properties and global climate observed at Cicogna agrees with the long-term climate stabilization mechanism first described by Walker et al. (1981). According to this model, carbon dioxide, which is released by volcanoes and metamorphism to the ocean-atmosphere system, is returned to the solid earth by the weathering of silicates followed by the deposition of carbonates. The intensity of the weathering depends on the surface temperatures, which in turn depend on carbon dioxide partial pressure (pCO_2) through the greenhouse effect (Walker et al., 1981; see also Velbel, 1993; Kump et al., 2000). The rate of silicate weathering therefore provides a negative feedback mechanism to buffer pCO_2 variations and consequently Earth's climate change, and the signature of this mechanism is apparently registered in the Belluno Basin by the deposition of detrital magnetic phases with oxidation states determined by the intensity of the land weathering processes that are in turn tied to global climate.

Table 1

		Low-field susc.	High-field susc.	$IRM_{0.1\,T}$	$IRM_{1.0\,T}$	$IRM_{1.0/0.1T}$
Zone 1 (0–28.7 m)	Max	10.32	6.13	19.55	26.93	3.35
	Min	3.24	4.90	0.16	0.19	1.18
	Mean	5.94	5.47	3.43	5.93	2.00
	St. Dev.	1.50	0.54	4.21	5.64	0.52
Zone 2 (28.7–36 m)	Max	23.63	15.64	33.65	71.76	6.43
	Min	3.12	4.31	0.44	0.83	0.90
	Mean	9.05	10.17	6.09	17.67	3.38
	St. Dev.	4.46	3.30	5.97	13.34	1.09
Zone 3 (36–47 m)	Max	48.20	6.41	147.34	183.7	2.34
	Min	4.69	4.72	2.32	2.91	1.13
	Mean	11.24	5.54	20.56	31.53	1.62
	St. Dev.	6.67	0.84	21.29	26.79	0.23
Zone 4 (47–74 m)	Max	11.76	6.53	13.23	31.43	7.33
	Min	2.60	3.31	0.36	0.48	1.24
	Mean	5.56	4.69	3.39	10.54	4.10
	St. Dev.	1.79	1.10	3.07	5.80	1.58

Table 6.1. List of the rock-magnetic parameters values for each rock-magnetic zone described in the text; low- and high-field susceptibilities are expressed in 10^{-8} m^3Kg^{-1}; $IRM_{0.1\ T}$ and $IRM_{1.0\ T}$ are expressed in 10^{-3} Am^2Kg^{-1}.

Acknowledgements

E. Dallanave and D. Rio were supported by MIUR-PRIN Grant # 2007W9B2WE_004. Acknowledgment is made to the Donors of the American Chemical Society Petroleum Research Fund for partial support of this research in the SIO laboratory.

Chapter 7

The Forada Section

7.1 Introduction

The upper Cretaceous to lower Eocene Forada section is located along the Forada riverbed (Fig. 2.1; 46.04°N, 12.07°E) and consists of ~62 m of pink-reddish limestones and marly limestones, referred to as the Scaglia Rossa Formation. The clay marl unit (CMU) of the Forada section, the base of which coincides with the Paleocene–Eocene transition, is 3.55 m-thick and was previously described by Giusberti et al. (2007), who pointed out that the CMU represents the lithological expression of the PETM. Data supportive of this interpretation include the presence in the CMU of (i) a major extinction event among benthic foraminifera, (ii) the calcareous nannofossils excursion taxa (CNET), which are restricted to the PETM (Aubry et al., 2002), and (iii) a marked negative $\delta^{13}C$ shift (Giusberti et al., 2007). Similar events associated with the PETM have been observed also elsewhere in outcropping sections (e.g. Dababiya in Egypt; Dupui et al., 2003) as well as in deep-sea sediments (e.g. ODP Stie 690; Bralower, 2002).

For the purposes of this thesis, I described and sampled the 8 m-thick part of the Forada section across the Paleocene–Eocene boundary, from 1.5 m below the CMU base to 2.95 m above the CMU top. I subdivided the sampled transect in three main lithological units, namely the pre-CMU, the CMU, and the post-CMU unit (Fig. 7.1).

Pre-CMU. From -1.5 m to -0.2 m, the section is comprised of reddish marly limestones with no apparent lithological rhythmicity. The upper ~0.2 m are constituted by greenish-gray limestones; they are characterized by the presence of ichnofossils

(zoophychos and chondrites); the uppermost 1.5–2.0 cm of this greenish-gray band are depleted in calcium carbonate and are dark gray in color.

CMU. The base of the CMU is marked by a ~0.3 cm-thick black clay lamina; above the black lamina, the CMU is constituted by ~0.6 m of greenish–gray clay marls, finely laminated at the base. From ~0.6 m to ~2.0 m the sediments are red marls abundantly mottled with centimetric gray-greenish spots and lenses (Photo A7.1 in Appendix). From ~2.0 m to the top of the CMU at 3.55 m, the prevalent color of the sediment is red, although the presence of gray-greenish levels persist (Photo A7.2 in Appendix).

Post-CMU. From level 3.55 m to the top of the measured section at 6.50 m, reddish marl–limestone couplets compose the sediments.

7.2 Material and Methods

A total of 153 samples were collected every 5 cm across the described section at Forada. Similarity to the analyses conducted on the Cicogna sediments (see **Chapter 6**), all the samples were first weighted, and the bulk susceptibility was then measured. The samples were successively magnetized in 0.1 T and 1.0 T fields and the values of the isothermal remanence (IRM) were measured on a 2G DC SQUID cryogenic magnetometer located at the Alpine Laboratory of Paleomagnetism (Peveragno, Italy). A set of 33 representative samples were magnetized in 2.5 T, 1.0 T and 0.1 T fields along three orthogonal axes; the samples were then subjected to alternating field (AF) demagnetization using a SI-4 specimen demagnetizer, following 13 demagnetization steps from 5 to 180 mT. After this procedure, the same set of samples plus 25 additional samples were magnetized along three orthogonal directions using the same fields, and

then subjected to thermal demagnetization adopting 18 demagnetization steps from room temperature to 670 °C (Lowrie, 1990). A total number of 10 red samples were characterized by the presence of grey levels or spots; in these cases, the two (red and green) lithologies were analyzed separately. Hysteresis parameters were also obtained by analyzing a selected suite of 19 ~0.02–0.03 g samples with a MICROMAG alternating gradient force magnetometer. Values of saturation magnetization (Ms), saturation remanence (Mr) and coercivity (Bc) were determined from the hysteresis loops after correction for a ubiquitous paramagnetic component. The values of the high-field magnetic susceptibility and of the coercivity of remanence (Bcr) were estimated as described in section **6.3** for the Cicogna section. The AF and thermal demagnetization of the three orthogonal IRMs and the hysteresis experiments were conducted at the paleomagnetic laboratory of the Scripps Institution of Oceanography (La Jolla, California).

7.3 Rock magnetic data

7.3.1 Pre-CMU unit. The low-field magnetic susceptibility of the pre-CMU interval shows an average value of 6.3 $x10^{-8}$ m^3kg^{-1} (Fig. 7.1, Table 7.1), similar to the 6.2 $x10^{-8}$ m^3kg^{-1}observed for the high-field susceptibility. The low-field susceptibility shows a rhythmicity that is not apparently related to lithologic variations visible in the field.

Thermal demagnetization of three components IRM (2.5T, 1.0T, and 0.1T) of the samples collected from -1.5 m to -0.2 m are dominated by a 1.0 T coercivity phase, which shows a smooth loss of magnetization between 300–400 °C, followed by a gently reduction between 400–600 °C and a subsequent abrupt decrease to zero values up to 670 °C.

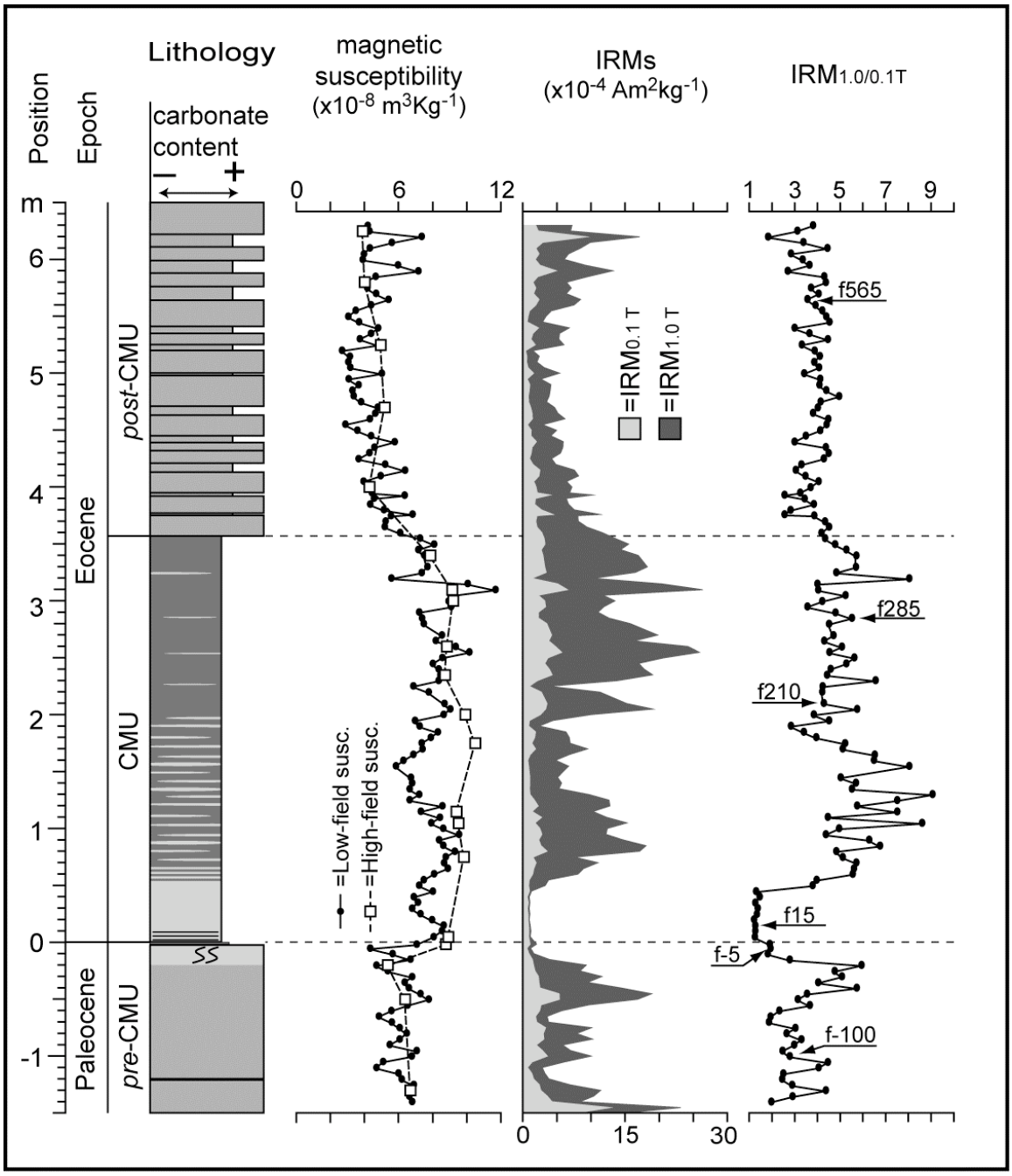

Figure 7.1. The Forada section; from the left: -lithological log of the section, with the subdivision in pre-CMU (clay marl unit), CMU, and post-CMU units; -rock-magnetic stratigraphy across the section, represented by the low- and high- fields susceptibility, the IRM at 0.1 T and 1.0T, and the ratio of these IRMs ($IRM_{1.0/0.1\ T}$).

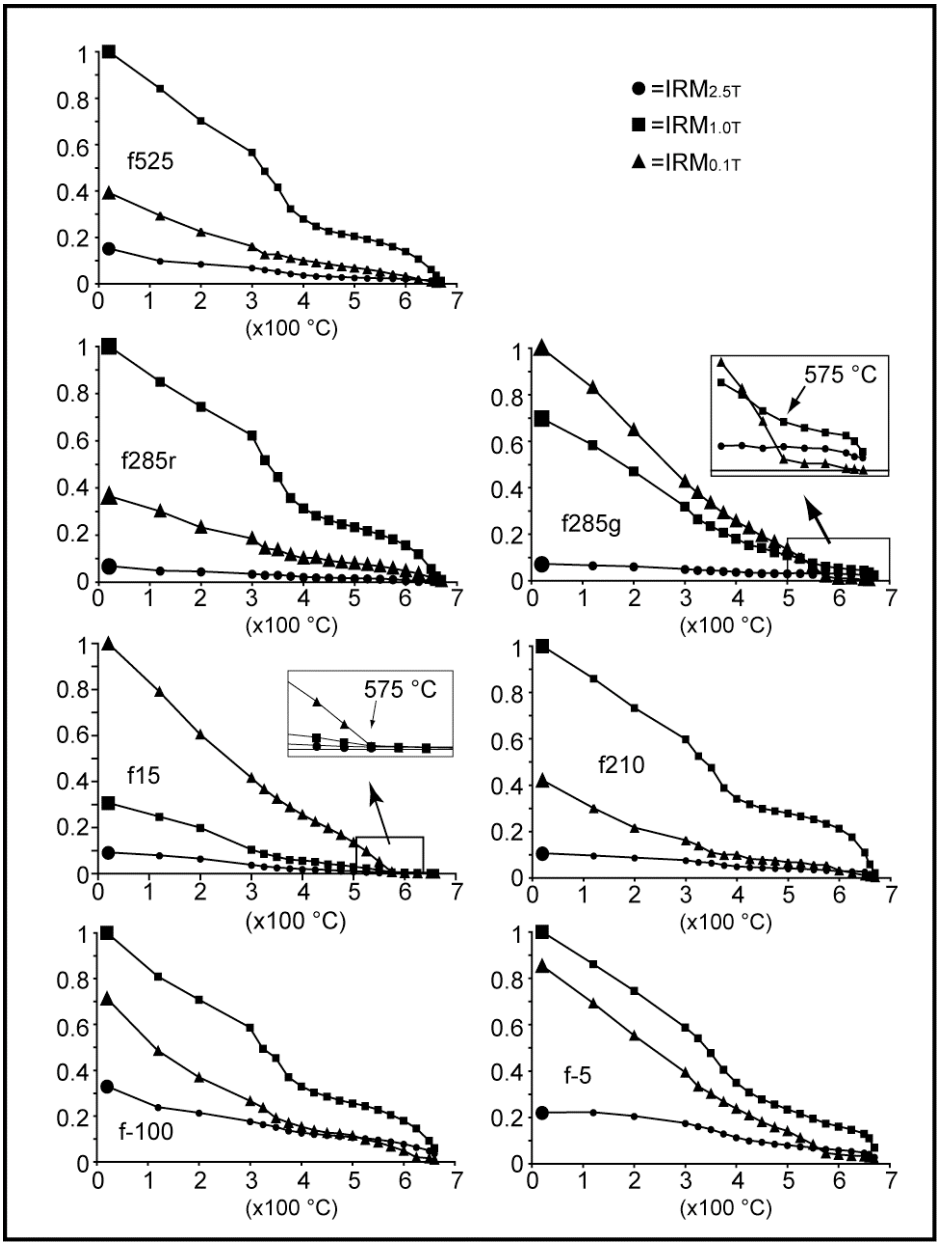

Fig. 7.2. Representative thermal demagnetization diagrams of three orthogonal components IRM. See text for details.

		Low-field susc.	High-field susc.	$IRM_{0.1\ T}$	$IRM_{1.0\ T}$	$IRM_{1.0/0.1T}$
Pre-CMU (-1.5 – 0 m)	Max	9.79	6.71	12.84	23.12	5.95
	Min	4.33	5.38	0.59	1.13	1.8
	Mean	6.28	6.16	2.91	8.45	3.12
	St. Dev.	1.07	0.69	2.4	5.21	1.18
CMU (0 – 3.55 m)	Max	11.69	10.5	6.54	26.37	9.06
	Min	5.56	7.86	0.65	0.92	1.21
	Mean	7.97	9.23	2.26	6.63	4.71
	St. Dev.	1.06	0.68	1.35	1.35	1.81
Post-CMU (3.55 – 6.5 m)	Max	7.34	5.19	9.39	17.11	4.96
	Min	2.67	3.91	0.38	1.47	1.82
	Mean	4.51	4.36	1.87	6.43	3.77
	St. Dev.	1.08	0.58	1.36	2.87	0.63

Table 7.1. Rock-magnetic values of the Forada lithologic units described in the text; low- and high-field susceptibilities are expressed in 10^{-8} m^3Kg^{-1}; $IRM_{0.1\ T}$ and $IRM_{1.0\ T}$ are expressed in 10^{-3} Am^2Kg^{-1}.

This magnetic phase co-exists with a 0.1 T and a minor 2.5 T coercivity phase, which persist respectively up to 650 °C and 670 °C (Fig 7.2, sample f-100). The red samples of the pre-CMU unit are interpreted as composed by a mixture of hematite (with maximum unblocking temperatures of 670 °C) and maghemite (as revealed by the 1.0 T intensity reduction at 300–400 °C and by a regular intensity decrease of the 0.1 T curve up to 650 °C; see section 6.4.1 for further details on this interpretation). The samples collected form the upper 0.2 m of the pre-CMU unit, which are gray-greenish in color, show a similar behavior (due to the presence of hematite and minor maghemite), save for a higher relative contribution of the 0.1 T magnetic coercivity phase that reaches very low values at 575 °C and is interpreted as magnetite (Fig 7.2, sample f-5).

AF demagnetization of the pre-CMU reddish samples reveals that the 1.0 T coercivity component drops by ~40–50% up to fields of ~180 mT, while the 0.1 T coercivity component is characterized by a virtually total (100%) drop of intensity by peak fields of 100 mT. AF demagnetization has no appreciable effect on the high

coercivity (2.5 T) component (Fig. 7.3, sample f-100). Gray-greenish samples from the upper 0.2 m of the pre-CMU show similar coercivity spectra, save for the higher relative contribution of the 0.1 T coercivity phase (Fig. 7.3, sample f-5).

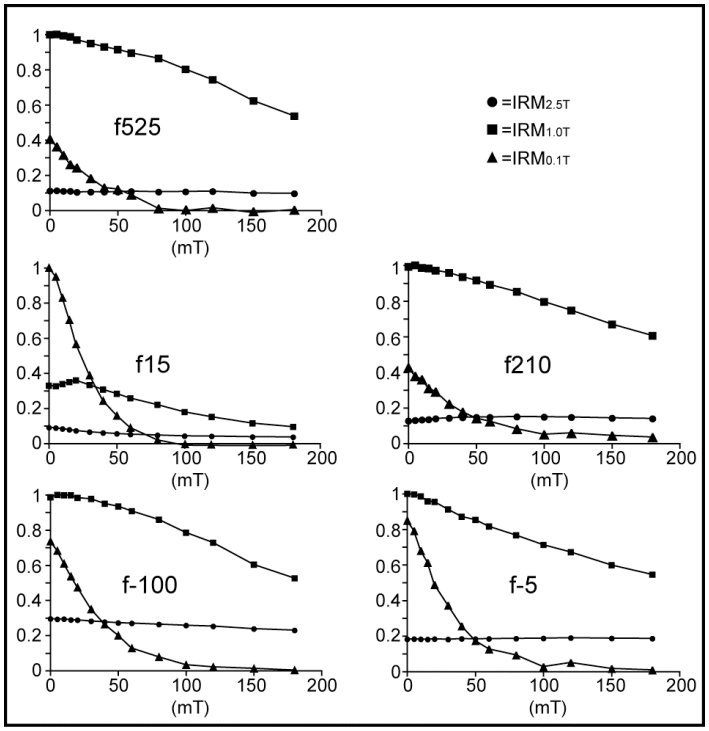

Figure 7.3. Representative alternating field (AF) demagnetization diagrams of three orthogonal components IRM.

The $IRM_{0.1T}$ and the $IRM_{1.0T}$ show a high variability. Both IRMs display an abrupt drop of values in correspondence of the gray-greenish sediment of the upper ~0.2 m of the pre-CMU (Fig. 7.1). The same drop of values is observed also in the $IRM_{1.0/0.1T}$ ratio.

After correction for a paramagnetic component, hysteresis loops of samples from the reddish pre-CMU sediments show a typical wasp-waisted shape (Fig. 7.4, sample f-50), confirming the presence of contrasting magnetic coercivity phases (e.g. Channell and McCabe, 1994; Muttoni, 1995; Roberts et al., 1995; Tauxe et al., 1996).

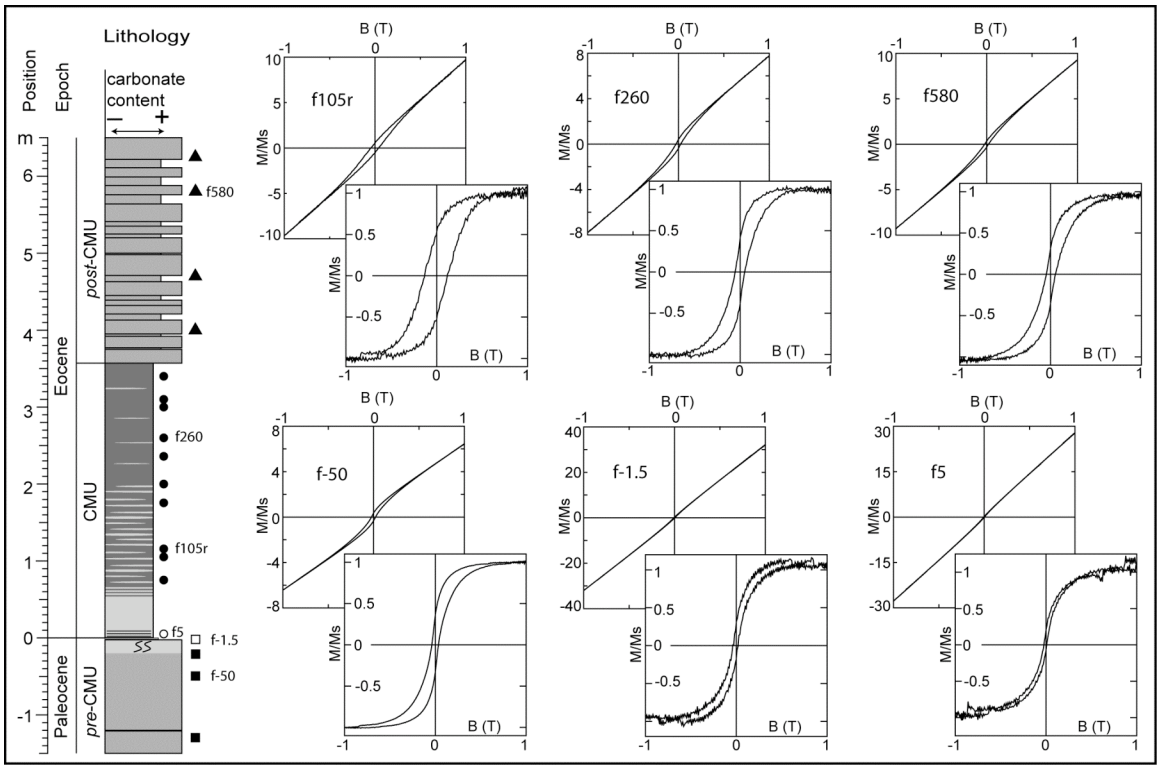

Figure 7.4. Hysteresis loops of representative samples from the Forada section with indication of stratigraphic position; the background and the foreground diagrams represent the loops before and after paramagnetic correction, respectively; the vertical axes of the diagrams represent the magnetization/saturation magnetization (M/Ms) ratio, while the horizontal axes the applied field (B) expressed in Tesla (T).

The Mr/Ms ratios of samples from the pre-CMU unit (squares in Fig. 7.5) are generally higher compared to that of a magnetite-bearing limestone reference distribution (crosses in Fig. 7.5; Channell and McCabe, 1994), and approach the single domain (SD) hematite + pseudo-single domain (PSD) magnetite mixture reference value of Roberts et al. (1995).

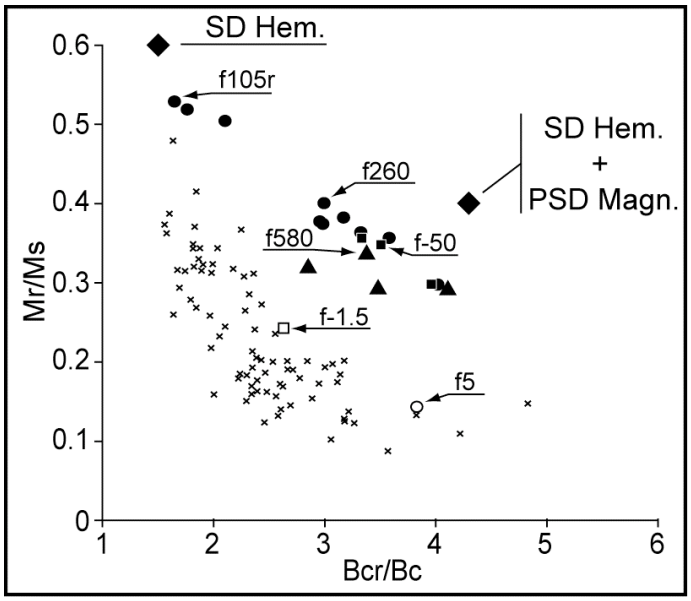

Figure 7.5. Plot of Mr/Ms versus Bcr/Bc (Mr= remanent magnetization; Ms= saturation magnetization; Bcr= coercivity of remanence; Bc= magnetic coercivity) of samples from the Forada section; squares refer to the pre-CMU samples, circles refer to CMU samples, and triangles refer to the post-CMU samples; the black symbols refer to red samples, while open symbols refer to gray-greenish samples (collected between -0.2 m (pre-CMU) and 0.5 m (CMU)). The Cicogna samples distribution is compared to a reference distribution of hysteresis parameters (black crosses) obtained for magnetite-bearing (i.e. low coercivity) limestones from the literature (Channell and McCabe, 1994). The black diamonds indicate the reference values for SD hematite and for a PSD magnetite+SD hematite mixture of Roberts et al. (1995).

In summary, a hematite phase associated with maghemite dominates the reddish sediments of the pre-CMU. A mixture of magnetite and hematite constitute the gray-greenish sediments of the upper 0.2 m of the pre-CMU, although the weak bend of the 1.0 T coercivity phase between 300–400°C observed in the IRMs thermal demagnetization diagrams reveals the presence of minor amounts of maghemite.

7.3.2 CMU unit. The low-field and the high-field magnetic susceptibility display generally higher values with respect to those observed in the pre-CMU sediments (Fig. 7.1, Table 7.1).

Thermal demagnetizations of three orthogonal IRMs (2.5T, 1.0T, 0.1T) of the gray-greenish samples from the basal ~0.6 m of the CMU unit are dominated by the 0.1 T coercivity phase, which approaches zero at 575 °C and is interpreted as magnetite. This phase coexists with minor 1.0 T and 2.5 T coercivity phases, with maximum unblocking temperatures >575 °C and interpreted as hematite. The red samples from the CMU unit contain a high contribution of the 1.0 T magnetic coercivity phase (Fig. 7.2, samples f210, f285r), with the usual loss of intensity between ~300–400 °C and maximum unblocking temperature of 670 °C, indicative of hematite coexisting with minor maghemite-coated grains (see section **6.4.1**). The samples collected from the gray-greenish levels observed in the red sediments of the CMU unit are instead dominated by the 0.1 T coercivity phase, which approaches zero at 575°C and is interpreted as magnetite; this magnetite phase coexists with minor 1.0 T and 2.5 T coercivity phases, which persist up to 670 °C and are interpreted as hematite (Fig. 7.2, sample f285g).

The AF demagnetization of three components IRM reveals that the low coercivity (0.1 T) component is characterized by a virtually total (100%) drop of intensity by peak fields of 100 mT, while the mid coercivity (1.0 T) component drops by ~40% in fields of ~180 mT. AF demagnetization has no appreciable effect on the high coercivity (2.5 T) component (Fig. 7.3, sample f210). These AF demagnetization spectra are analogous for both the gray-greenish and the red samples, although the proportions of the single coercivity components are different.

The $IRM_{0.1T}$ and the $IRM_{1.0T}$ vary significantly along the CMU; the lowest values are registered in the first ~0.6 m, while between ~2 m and ~3.5 m the IRMs reach the highest values. Analogously, the $IRM_{1.0/0.1\ T}$ values are lowest in the basal ~0.6 m of the CMU unit, to increase from level ~0.6 m to level ~2 m and maintain high values of ~5 up to the top of the CMU. In any case, the variability of the $IRM_{1.0/0.1\ T}$ parameter is very high, especially between 0.6–2.0 m, due to the presence of abundant gray-greenish levels and spots in the red sediments (Fig. 7.1, Table 7.1, Photo A7.2).

The hysteresis loops of the samples collected in the gray-greenish level at the CMU base are strongly dominated by paramagnetic minerals. After the high-field slope correction, the noisiness of the signal does not allow a reliable determination of the hysteresis parameters, except for the f5 sample (Fig. 7.4). In the red specimens collected from ~1 m to ~ 2 m within the CMU, the shape of the loops suggests that a single magnetic phase dominates (Fig. 7.4, Fig. 7.5, sample f105r) and the hysteresis parameters distribution approach the SD hematite reference value of Roberts et al. (1995). Nonetheless the thermal and AF demagnetization of three components IRM of the red specimens from the CMU revealed the presence of both high and low coercivity phases. From ~2 m upward the hysteresis loops show again the typical wasp-waisted shape (Fig. 7.4, Fig. 7.5, sample f260),

In summary, the gray-greenish samples collected from the basal ~0.6 m of the CMU, as well as from the gray-greenish levels observed within the rest of the CMU, are dominated by magnetite coexisting with a minor amount of hematite. A mixture of hematite and minor maghemite characterizes the red samples from the CMU.

7.3.3 Post-CMU unit. From the upper limit of the CMU (3.55 m) up to the ~4.7 m level, the low-field magnetic susceptibility generally decreases, showing a trend that follows tightly the marl–limestone couplets, whereby relative high (low) values correspond to the marls (limestones) levels; this coupling then persists up to the top of the sampled section (Fig. 7.1). The high-field and the low-field susceptibility are in general agreement, displaying similar values.

Thermal demagnetization of three orthogonal IRMs are dominated by the 1.0 T coercivity component, which displays a smooth loss of magnetization between 300–400 °C, approaching then zero value at 670 °C. This component coexists with relative minor 0.1 T and 2.5 T magnetic coercivity phases, which approach zero respectively at 650 °C and 670 °C (Fig. 7.2, sample f525). The samples from the post-CMU unit are thus interpreted as containing a mixture of hematite and maghemite.

AF thermal demagnetization revealed that the 1.0 T coercivity component drops by ~40–50% in fields of ~180 mT, while the 0.1 T coercivity component is characterized by a virtually total (100%) drop of intensity by peak fields of 100 mT. AF demagnetization has no appreciable effect on the high coercivity (2.5 T) component (Fig. 7.3, sample f525).

The $IRM_{0.1T}$ and the $IRM_{1.0T}$ show a trend that is similar to that observed for the low field susceptibility whereby they decrease up to ~4.7 m and then they increase again up to the unit top. The $IRM_{1.0/0.1\,T}$ ratio shows an average value of ~3.8 up to the unit top.

After the correction for the paramagnetic slope, a wasp-waisted shape characterizes the hysteresis loops of the post-CMU sediments (Fig. 7.4, sample f580), confirming the presence of distinct coercivity phases.

In summary, the red sediments composing the post-CMU are dominated by hematite, coexisting with minor maghemite.

7.3.4 Summary of the magnetic data. A mixture of hematite and maghemite dominates the red specimens from throughout the Forada section; this is suggested by the presence of a 1.0 T and a 2.5 T coercivity magnetic phases that persist up to 670 °C (hematite) and by the presence of a 0.1 T coercivity phase persisting up to 650 °C as well as by a 1.0 T intensity decrease between 300 and 400 °C (maghemite-coated grains) (see section **6.4.1** for details). The gray-greenish samples (from gray-greenish spots and levels scattered throughout the section) are instead dominated by magnetite coexisting with minor amounts of hematite, as revealed, respectively, by a 0.1 T coercivity phase approaching zero at 575 °C and by high (1.0 T and 2.5 T) coercivity phases persisting generally up to 670 °C.

7.4 Diagenesis at Forada

We observed several analogies between the Forada and the Cicogna datasets. There is a general tendency for the magnetic susceptibility and the IRMs data, especially the $IRM_{1.0/0.1T}$ ratio, to be higher in the CMU unit than in pre- and post-CMU units. This is reminiscent to what observed across the CMU at Cicogna and is interpreted as due to higher amounts of hematite phases during the PETM, when the silicate weathering machine was at full speed (see section **6.6** for details). However, the data from Forada are much less clear than those from the Cicogna section, due to a strong diagenetic overprint. Following the observation made at the Cicogna section, especially in the rock-magnetic zones 2,3, and 4 (see section **6.4.5**), the gray-greenish samples collected in abundant

gray-greenish levels and spots throughout the CMU at Forada are interpreted as derived by post-depositional chemical reduction processes of preexisting red sediments. I believe that these post-depositional chemical reduction processes operated at Forada much more widely than at Cicogna. This interpretation is confirmed by the rock-magnetic analyses; in particular, the IRM intensity of the gray-greenish samples is about one order of magnitude lower than that of the red samples (Fig. 7.6); this is because, under reductive conditions, the newly formed magnetite is readily dissolved (Fischer et al., 2007), decreasing the associated IRM values. These alteration processes are particularly evident from -0.2 m to 0.6 m (across the CMU onset; Fig. 7.1), where the lithology is predominantly gray-greenish in color; the measured $IRM_{0.1T}$, $IRM_{1.0T}$, and their ratio ($IRM_{1.0/0.1T}$) display the lowest values of the section. The same parameters display a high variability up to the top of the CMU, especially between 1.0 and 2.0 m, where the red sediments are characterized by abundant gray-greenish levels. I therefore conclude that the variations of the magnetic properties at Forada are strongly conditioned by the chemical processes occurred after the deposition of the sediments, and thus they hardly reflect primary (i.e. syndepositional) variations of the magnetic mineralogy of the sediments.

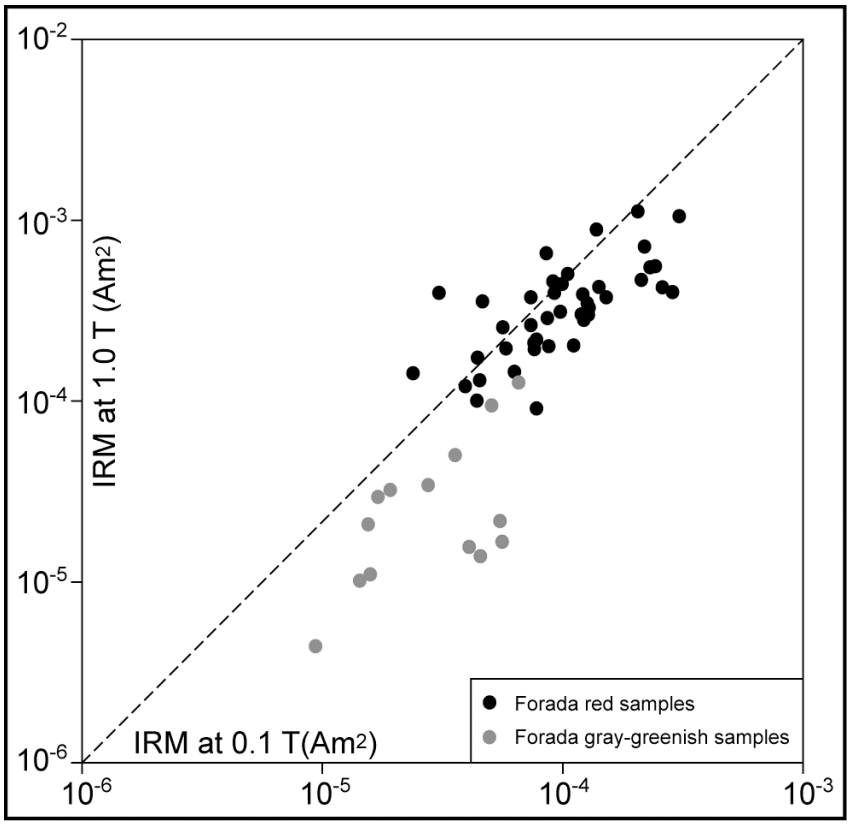

Figure 7.6. Logarithmic plot of IRMs at 0.1 T and 1.0 T of the thermally demagnetized representative samples; the gray–greenish samples display generally the lowest values.

7.5 Conclusions

At Cicogna (**Chapter 6**), I successfully used the $IRM_{1.0/0.1T}$ to monitor the relative amount variations of the ferromagnetic minerals across the section. I was then able to demonstrate that the relative increases of high coercivity hematite phases were related to enhanced continental weathering during times of globally warm conditions such as the PETM and the early Eocene (see section 6.6). At Forada, I described and sampled an 8 m-thick section across the lithological expression of the PETM – known as clay marl unit, or CMU – in order to refine what observed at Cicogna. The magnetic analyses,

associated with field observations, revealed however that the sediments of the Forada CMU section, while showing the same general picture as at Cicogna, underwent pervasive post-depositional chemical reduction processes that indelibly altered their original magnetic properties. I therefore conclude that the collected magnetic data and their stratigraphic variations, at least in the CMU, are not related to syndepositional processes and thus they cannot be readily interpreted in a paleoclimatic key.

Appendix 7

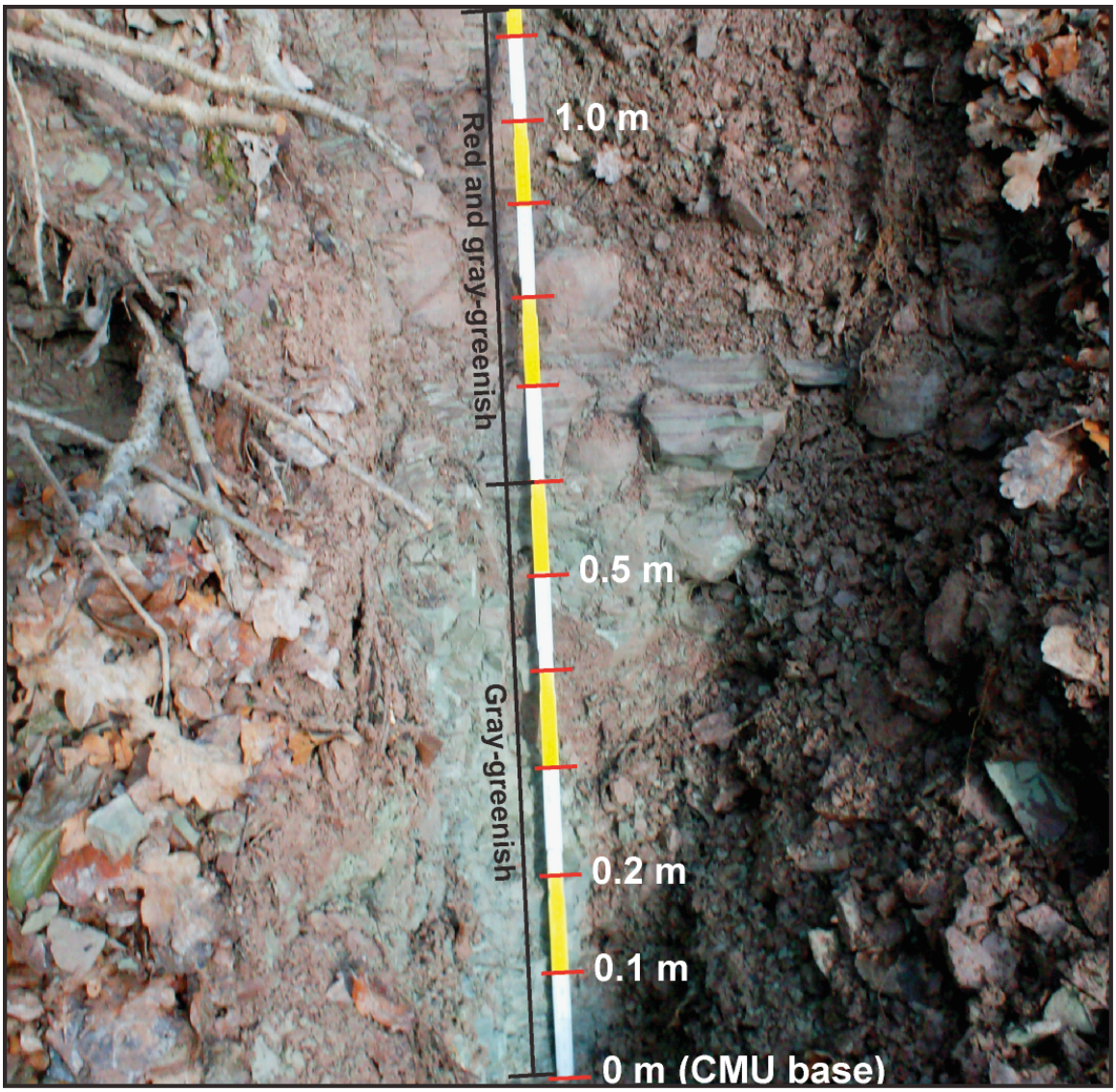

Photo A7.1. The Forada CMU (from 0.0 m to 1.0 m); between 0.0 – 0.5 m levels the lithology is gray-greenish in color, while above it is red with abundant gray-greenish levels.

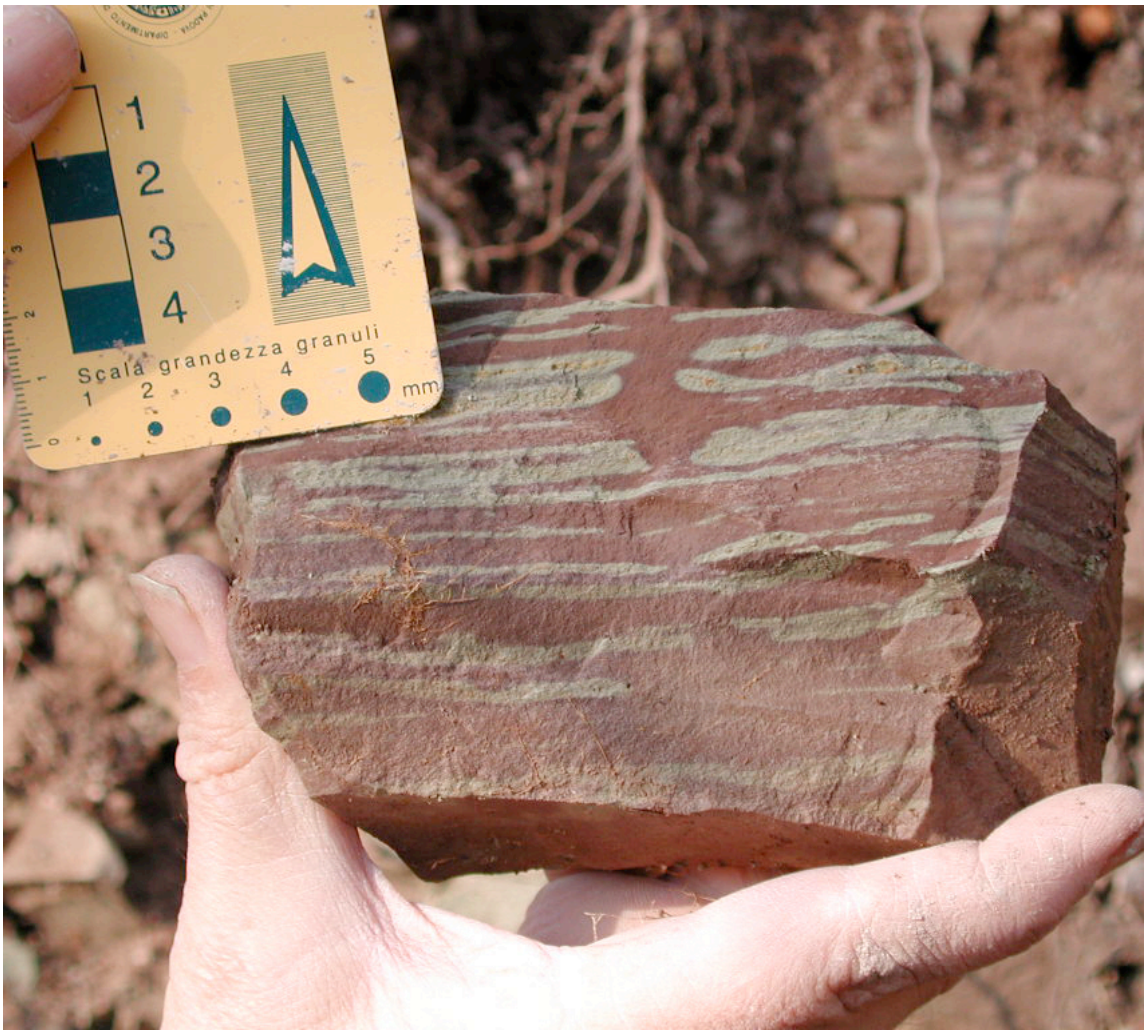

Photo A7.2. Rock sample collected from ~1.5 m level (CMU) at Forada; the lithology is characterized by red marls with abundant gray-greenish levels.

Chapter 8

Conclusions

In this thesis, I presented detailed magnetostratigraphic data from three early Paleogene Tethyan marine sections cropping out in the Belluno Valley (NE Italy), namely the Ardo section, the Cicogna section, and the Forada section (Fig. 1.1). The obtained dataset allowed to improve the current reference time scale (BKSA95; Berggren et al., 1995) for the Paleocene–early Eocene, specifically during Chron C24r, as well as to better understand the mechanisms behind the late Paleocene–early Eocene global climate evolution, as summarized hereafter.

Part 1. Improvement of the current early Paleogene time scale.

The Ardo and the Cicogna data provided an excellent record of the geomagnetic reversals across respectively the early Paleocene and the late Paleocene–early Eocene. The sequence of the reversals from both sections was used to construct age-depth plots by means of correlation with the CK95 geomagnetic polarity time scale (Cande and Kent, 1995). The derived age models and sediment accumulation rates are synthesized in Fig. 8.1. In detail, the Ardo section straddles Chrons from C29r to C26r; the sedimentation rates range from ~2.1 to ~4.0 m/Myr, with a mean of ~3.1 m/Myr. In this robust chronological calibrated framework, it will be possible to place the results of a detailed calcareous nannoplankton biostratigraphy, currently under study. The Cicogna section shows an overall sequence of 9 magnetozones, encompassing Chrons from C25r to C23r. The derived age model implies a relatively constant average sediment accumulation rate of ~18.2 m/Myr throughout the section.

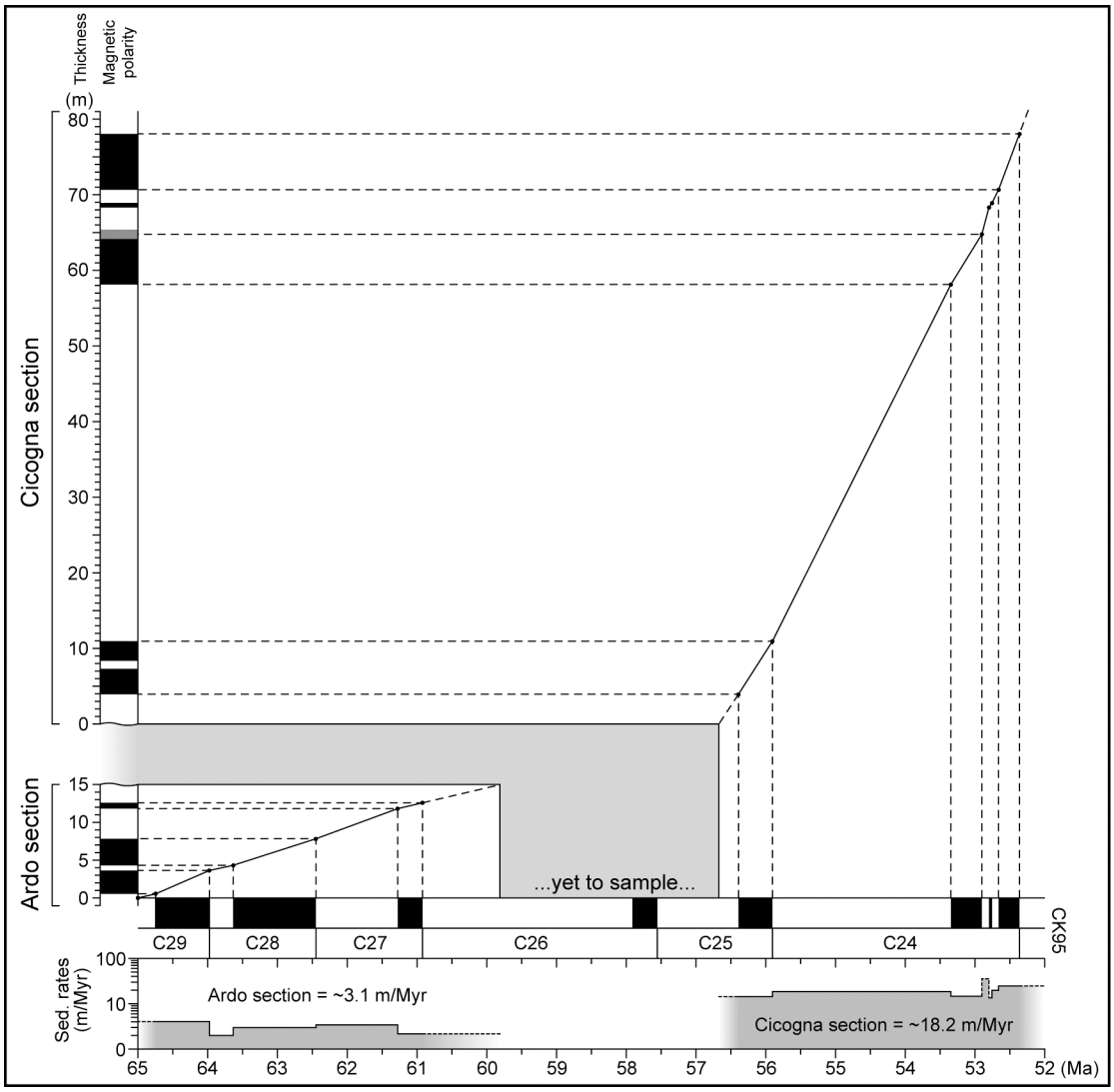

Figure 8.1. Age-depth models and derived sediment accumulation rates for the Ardo and the Cicogna sections, obtained by magnetostratigraphic correlation with the CK95 reference timescale (Cande and Kent, 1995).

The Cicogna age-depth function has been used to place the sequence of biohorizons recognized in the sediments in a temporal reference frame for comparison with similar bioevents reported in the BKSA95 time scale. Apart from standard biohorizons, whose ranking and spacing have found to be largely consistent with previous studies (e.g.,

Backman, 1986; Berggren et al., 1995; Raffi et al., 2005; Agnini et al., 2007 and references herein), the Cicogna section provides several new bioevents in the NP9–NP10 (CP8–CP9a) interval within Chron C24r that were not previously recognized (hence included) in the BKSA95 reference time scale; several of these new biohorizons have been recently observed also at ODP Site 1262. These new magneto-biostratigraphic data from the expanded and continuously exposed Cicogna section represent an improvement of the late Paleocene–early Eocene chronology, which is not well defined in the current BKSA95 time scale essentially because of the presence of unconformities in several deep-sea and shallow water sections from the literature (Aubry et al., 1996) and the substantial lack of reference sections provided with a complete and expanded Chron C24r interval.

Part 2. **Understanding the long-term late Paleocene–early Eocene climate evolution.**

The late Paleocene–early Eocene was characterized by a global warming trend that eventually culminated with the early Eocene climatic optimum (EECO, ~52–50 Ma). The EECO was characterized by warm climatic conditions even at extremely high latitudes (Fig. 8.2A) (McKenna, 1980; Moran et al., 2006); Atlantic bottom waters reached temperatures of 14 °C, as indicated by oxygen stable isotope data (Fig. 8.2B) (Zachos et al., 2001, Miller et al., 2005). The late Paleocene–early Eocene warming trend was punctuated by several short-lived hyperthermal events, the most prominent of which was the Paleocene–Eocene thermal maximum (PETM; e.g. Kennett and Stott, 1991). Existing records reveal that during the PETM, deep-sea temperatures increased by 5–6 °C in less

than 10 Kyr, whereas sea-surface temperatures increased by 8 °C at high latitudes (see section 6.1 for details).

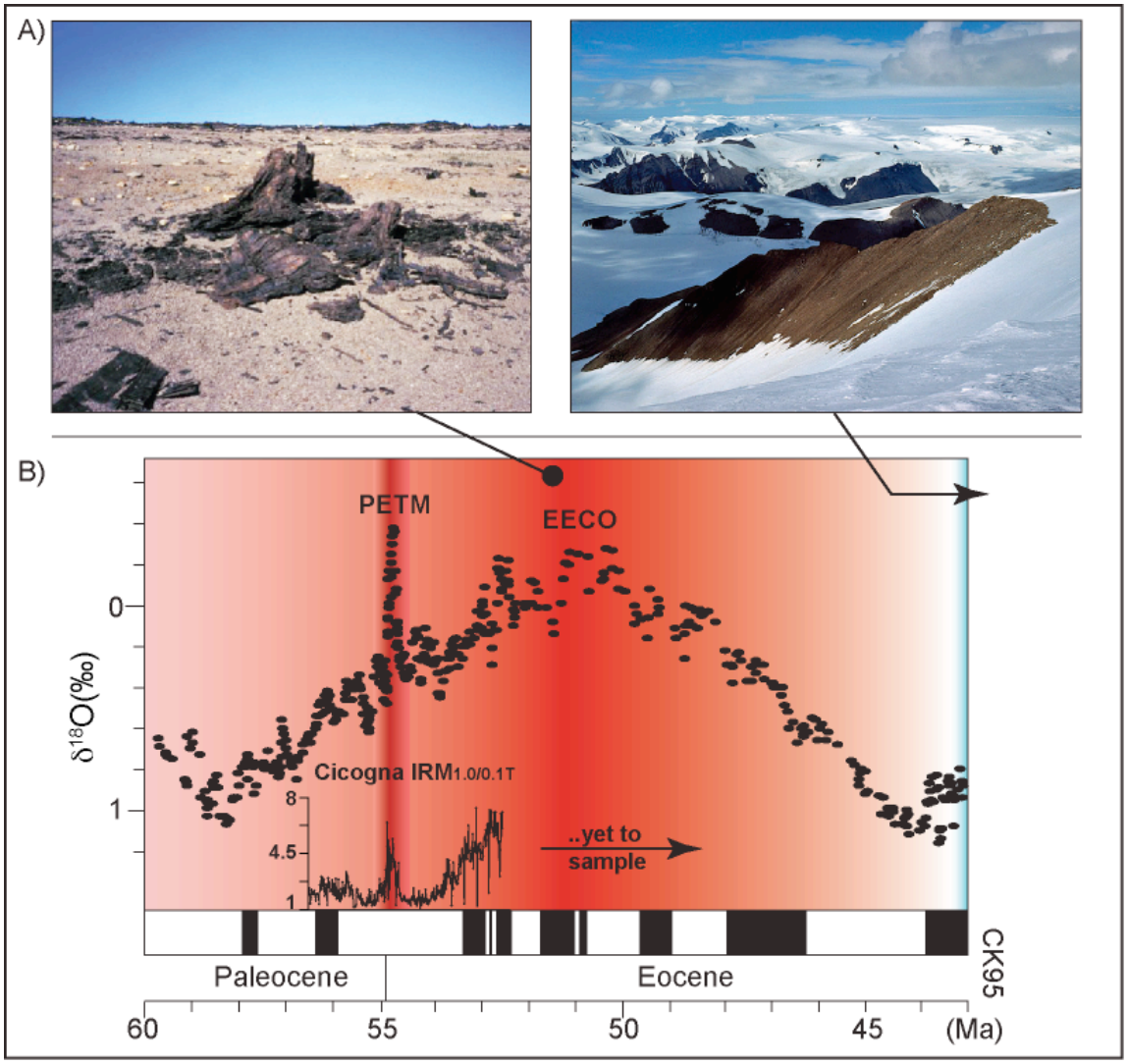

Fig. 8.2. A) Left: fossil of Eocenic conifer tree from the Axel Heiberg Island (Artic Canada; source: http://cgc.rncan.gc.ca/org/vancouver/gallery/index_e.php); right: the Axel Heiberg Island present-day landscape (source: http://www.swisseduc.ch/glaciers/axel_heiberg/astro_piper/index-en.html?id=12; B) $\delta^{18}O$ record of Zachos et al. (2001) across the 60–43 Ma time period, compared to the late Paleocene–early Eocene $IRM_{1.0/0.1T}$ record from the Cicogna section; both datasets are placed onto the same timescale (CK95; Cande and Kent, 1995).

The rock-magnetic dataset from the Cicogna section reveals a pronounced increase in the relative proportion of a high coercivity hematitic component of the sediments between ~54.9 and 54.6 Ma followed by a second, long-term increasing trend from ~54 Ma up to ~52.2 Ma at the section top. We speculate that the warm and humid climatic conditions typical of the PETM and the early Eocene warming trend leading to the EECO enhanced continental weathering of silicate rocks with the consequent production, transport, and sedimentation of hematite. This hypothesis is confirmed by a clear correlation between the rock-magnetic properties and global climate as revealed by a standard benthic oxygen isotope record from the literature (Zachos et al., 2001). Our temporal coupling between oxidation state of sedimentary magnetic phases and global climate therefore is consistent with the existence in the Paleocene–Eocene of the silicate weathering negative feedback mechanism for the long-term stabilization of the Earth's surfaces temperature first proposed by Walker et al. (1981).

To find a confirmation of what observed at Cicogna, I described and sampled an 8 m-thick section at Forada across the PETM. The rock-magnetic analyses, associated with field observations, revealed that the sediments of the Forada section underwent pervasive post-depositional chemical reduction processes. Therefore, rock-magnetic data from Forada, although they tend to confirm the general picture observed at Cicogna, can hardly be used to derive more detailed information on the mechanisms regulating silicate weathering during the PETM.

References

Agnini, C., Muttoni, G., Kent, D.V., Rio D., 2006. Eocene biostratigraphy and magnetic stratigraphy from Possagno, Italy: The calcareous nannofossils response to climate variability. Earth and Planetary Science Letters 241, 815–830.

Agnini, C., Forniaciari, E., Raffi, I., Rio, D., Röhl, U., Westerhold, T., 2007. High-resolution nannofossil biochronology of middle Paleocene to early Eocene at ODP Site 1262: Implications for calcareous nannoplankton evolution. Marine Micropaleontology 64, 215–248.

Agnini, C., Dallanave, E., et al., 2008. Il Paleogene inferiore in facies pelagica nel Veneto Nord-orientale. Rendiconti online Soc. Geol. It. 4, 5–12.

Arenillas, I., Molina, E., and Schmitz, B., 1999. Planktic foraminiferal and δ13C isotopic changes across the Paleocene/Eocene boundary at Possagno (Italy). International Journal of Earth Sciences 88, 352–364, doi: 10.1007/s005310050270.

Aubry, M.-P., Berggren, W.A., Stott, L., Sinha, A., 1996. The upper Paleocene–lower Eocene stratigraphic record and the Paleocene–Eocene boundary carbon isotopes excursion: implications for geochronology. Geological Society, London, Special Publications 101, 353-380. doi:10.1144/GSL.SP.1996.101.01.18

Aubry, M.-P., Cramer, B.S., Miller, K.G., Wright, J.D., Kent, D.V., Olsson, R.K., 2000. Late Paleocene event chronology: unconformities, not diachrony. Bull. Soc. Géol. France 171(3), 367–378.

Aubry, M.-P., Ouda, K., Dupuis, C., Van Couvering, J.A., and Members of the Working Group on the Paleocene/Eocene boundary, 2002. Proposal: Global Standard Stratotype

Section and Point (GSSP) at the Dababiya section (Egypt) for the base of the Eocene Series: International Subcommission on the Paleogene Stratigraphy, Internal Report, 58 pp.

Axelrod, D.I., 1984. An interpretation of Cretaceous and Tertiary biota in polar regions, Palaeogeogr. Palaeoclimatol. Palaeoecol. 45, 105–147.

Backman, J., Shackleton, N.J., 1983. Quantitative biochronology of Pliocene and early Pleistocene calcareous nannoplankton from theAtlantic, Indian and PacificOceans. Mar. Micropaleontol. 8, 141–170.

Backman, J., 1986. Late Paleocene to Middle Eocene calcareous nannofossil biochronology from the Shatsky Rise, Walvis Ridge and Italy. Palaeogeogr. Palaeoclimatol. Palaeoecol. 57, 43–59.

Barron, V., Torrent, J., 2002. Evidence for a simple pathway to maghemite in Earth and Mars soils. Geochimica et Cosmochimica Acta 66, 2801–2806.

Berggren, W.A., Kent, D.V., Swisher III, C.C., Aubry, M.-P., 1995. A revised Cenozoic geochronology and chronostratigraphy. In: Berggren, W.A., et al., eds, 1995. Geochronology, Time Scales and Global Stratigraphy Correlation. Soc. for Sediment. Geol., Tulsa, Okla., Spec. Publ., vol. 54, 129–212.

Berggren, W.A., Aubry, M.-P., van Fossen M., Kent, D.V., Norris, R.D., Quillévéré, F, 2000. Integrated Paleocene calcareous plankton magnetobiochronology and stable isotope stratigraphy: DSDP Site 384 (NW Atlantic Ocean). Palaeogeogr. Palaeoclimatol. Palaeoecol. 159, 1–51.

Berggren, W.A., Pearson, P.N., 2005. A revised tropical to subtropical Paleogene planktonic foraminiferal zonation. Journal of Foraminiferal Research 35, 279–298.

Berner, E.K., Berner, R.A., 1996. Global enviroment: water, air and geochemical cycles. Pretience-Hall, Upper Saddle River, N.J.

Berner, R.A., Canfield, D.E., 1989. A model for atmospheric oxygen over Phanerozoic time. Am. J. Sci. 289, 333–361.

Berner, R.A., 2004. The Phanerozoic Carbon Cycle; CO2 and O2. Oxford University Press, 150 pp.

Besse, J., Courtillot, V., 2002. Apparent and true polar wander and the geometry of the geomagnetic field over the last 200 Myr. J. Geophys. Res., 107(B11), 2300, doi:10.1029/2000JB000050.

Besse, J., Courtillot, V., 2003. Correction to ‘‘Apparent and true polar wander and the geometry of the geomagnetic field over the last 200 Myr’’. J. Geophys. Res., 108(B10), 2469, doi:10.1029/2003JB002684.

Bolle, M.-P., Adatte, T., 2001. Paleocene–early Eocene climatic evolution in the Tethyan realm: clay mineral evidence. Clay Minerals 36, 249–261.

Bowen, G.J., Beerling, D.J., Koch, P.L., Zachos, J.C., Quattlebaum, T., 2004. A humid climate state during the Paleocene/Eocene thermal maximum. Nature 432, 495–499.

Bowles, J., 2006. Data report: revised magnetostratigraphy and magnetic mineralogy of sediments from Walvis Ridge, Leg 208. Proc. Ocean Drill. Program Sci. Results 208, 1–24 (Http://www-odp.tamu.edu/publications/208_SR/VOLUME/CHAPTERS/206/.PDF).

Bralower, T.J., Premoli Silva, I., Malone, M., et al., 2002. Proccedings of the Ocean Drilling Program, Initial reports, Volume 198, http://www-odp.tamu.edu/publications/198_IR/198ir.htm.

Bralower, T.J., Zachos, J.C., Thomas, E., Parrow, M., Paull, K., Kelly, D.C., Premoli Silva, I., Sliter, W.V., Lohmann, K.C., 1995. Late Paleocene to Eocene paleoceanography of the equatorial Pacific Ocean: Stable isotopes recorded at Ocean Drilling Program Site 865, Allison Guyot. Paleoceanography 10 (4), 841–865.

Bukry, D., 1973. Low-latitude coccolith biotratigraphic zonation. Proc. Ocean Drill. Program Sci. Results 15, 685–703.

Butler R.F., 1998. Paleomagnetism: Magnetic domains to geologic terranes. Electronic Edition.

Cande, S.C., Kent, D.V., 1992. A new geomagnetic polarity time scale for the Late Cretaceous and Cenozoic. J. Geophys. Res. 97, 13917–13951.

Cande, S.C., Kent, D.V., 1995. Revised calibration of the geomagnetic polarity time scale for the Late Cretaceous and Cenozoic, J. Geophys. Res. 100 (B4), 6093–6096. doi:10.1029/94JB03098.

Castellarin, A., Cantelli, L., 2000. Neo-Alpine evolution of the Southern Eastern Alps. Journal of Geodynamics 30, 251–274.

Channell, J.E.T., McCabe, C., 1994. Comparison of magnetic hysteresis parameters of unremagnetized and remagnetized limestones. Journal of Geophysical Research 99 (B3), 4613–4623.

Cogné, J.P., 2003. PaleoMac: a Macintosh™ application for treating paleomagnetic data and making plate reconstructions. Geochem. Geophys. Geosyst., 4(1), 1007. doi:10.1029/2001GC000227.

Costa, V., Doglioni, C., Grandesso, P., Masetti, D., Pellegrini, G.B., Tracanella, E., 1996. Carta Geologica d'Italia, Foglio 063, Belluno. Roma, Servizio Geologico d'Italia, scale 1:50,000, 1 sheet + 74 p.

Cramer, B.S., Wright, J.D., Kent, D.V., Aubry, M.-P., 2003. Orbital climate forcing of d13C excursions in the late Paleocene – early Eocene (chrons C24n–C25n). Paleoceanography 18(4), 1097, doi:10.1029/2003PA000909.

Cramer, B.S., Kent, D.V., 2005. Bolide summer: The Paleocene/Eocene thermal maximum as a response to an extraterrestrial trigger. Palaeogeogr. Palaeoclimat. Palaeoecol. 224, 144–166.

Crowley, T.G., Berner, R.A., 2001. CO_2 and climate change. Science 292, 870–872, doi: 10.1126/science.1061664.

Dallanave, E., Agnini, C., Muttoni, G., Rio, D., 2009. Magneto-biostratigraphy of the Cicogna section (Italy): Implication for the late Paleocene–early Eocene time scale. Earth and Planetary Science Letters 285, 39–51.

Dessert, C., Dupre, B., Gaillarde, J., Francois, L.M., Allegre, C.J., 2003. Basalt weathering laws and the impact of basalt weathering on the global carbon cycle. Chem. Geol. 202, 257–273.

Dickens, G.R., O'Neil, J.R., Rea, D.K., Owen, R.M., 1995. Dissociation of oceanic methane hydrate as a cause of the carbon isotope excursion at the end of the Paleocene. Paleoceanography 10 (6), 965–971.

Di Napoli Alliata, E., Proto Decima, F., Pellegrini, G.B., 1970. Studio Geologico, Stratigrafico e Micropaleontologico dei Dintorni di Belluno. Memorie della Società Geologica Italiana 9, 1–28.

Dinarès-Turell, J., Baceta, J.I., Pujalte, V., Orue-Etxebarria, X., Bernaola, G., 2002. Magnetostratigraphic and cyclostratigraphic calibration of a prospective Paleocene/Eocene stratotype at Zumaia (Basque Basin, northern Spain). Terra Nova 14, 371–378.

Dinarès-Turell, J., Baceta, J.I., Pujalte, V., Orue-Etxebarria, X., Bernaola, G., Lorito, S., 2003. Untantling the Paleocene climatic rhythm: an astronomically calibrated Early Paleocene magnetostratigraphy and biostratigraphy at Zumaia (Basque Basin, northern Spain). Earth and Planetary Science Letters 216, 483–500.

Dinarès-Turell, J., Baceta, J.I., Bernaola, G.,Orue-Etxebarria, X., Pujalte, V., 2007. Closing the Mid-Paleocene gap: Toward a complete astronomically tuned Paleocene Epoch and Selandian and Thanetian GSSPs at Zumaia (Basque Basin, W Pyrenees). Earth and Planetary Science Letters 262, 450–467.

Dingle R.V., Marenssi S.A., Lavelle, M., 1998. High latitude Eocene climate deterioration: evidente from the northern Antartic Peninsula. Journ. Of South American Earth Science 11 (6), 571–579.

Doglioni, C., Bosellini, A., 1987. Eoalpine and meso-alpine tectonics in the Southern Alps. Geologische Rundschau 77, 734–754.

Dupuis, C., Aubry, M.-P., Steurbaut, E., Berggren, W., Ouda, K., Magincalda, R., Cramer, B.S., Kent, D.V., Speijer, R.P., Heilmann-Clausen, C., 2003. The Dababiya Quarry section: Lithostratigraphy, geochemistry and paleontology, in: Ouda, K.,

Aubry, M.-P., eds., The upper Paleocene–lower Eocene of Upper Nile Valley: Part 1, Stratigraphy. Micropaleontology 49(1), 41–59.

Ebelmen, J.J., 1845. Sur les produits de la decomposition des especes minerals de la famile des silicates. Annu. Rev. Moines 12, 627–654.

Estes, R., Hutchison, J.H., 1980. Eocene lower vertebrates from Ellesmere Island, Canadian Arctic Archipelago, Palaeogeogr. Palaeoclimatol. Palaeoecol. 30, 325–347.

Fischer, H., Lustre, J., Gehring, A.U., 2007. EPR evidente for maghemitization of magnetite in a tropical soil. Geophys. J. Int. 169, 909–916.

Gaetani, M., Jadoul, F., 1979. The structure of Bergamasc Alps. Rend. Azz. Naz. Lincei, 8, 66, 5, 411–416.

Garrels, R.M., Mackenzie, F.T., Hunt, C., 1975. Chemical Cycles and the Global Environment: Assessing Human Influences. Los Altos, CA: William Kaufmann, Inc. 206 pp.

Gibbs, M.T., Bluth, G.S., Fawcett, P.J., Kump, L.R., 1999. Chemical weathering over the last 240 Myr: variations due to changes in paleogeography, paleoclimate, and paleogeology. Am. J. Sci. 299, 611–651.

Giusberti, L., Rio D., Agnini, C., Backman, J., Fornaciari, E., Tateo, F., Oddone, M., 2007. Mode and tempo of the Paleocene-Eocene thermal maximum in an expanded section from the Venetian pre-Alps. Geological Society of America Bulletin 119, 391–412. doi:10.1130/B25994.1

Holland, H.D., 1978. The chemistry of the atmosphere and oceans. Wiley, New York.

Kelly, D.C., Bralower, T.J., Zachos, J.C., Premoli Silva, I., Thomas, E., 1996. Rapid diversification of planktonic foraminifera in the tropical Pacifi c (ODP Site 865) during the late Paleocene thermal maximum. Geology 24, 423–426.

Kennett, J.P., Stott, L.D., 1991. Abrupt deep-see warming, paleoceanographic changes and benthic extinctions at the end of the Paleocene. Nature 353, 225–229.

Kent, D.V., Olsen, P.E., Witte, W.K., 1995. Late Triassic–earliest Jurassic geomagnetic polarity sequence and paleolatitudes from drill cores in the Newark rift basin, eastern North America, J. Geo-phys. Res. 100, 14965–14998.

Kent, D.V., Cramer, B.S., Lanci, L., Wang, D., Wright, J.D., Van der Voo, R., 2003. A case for a comet impact trigger for the Paleocene/Eocene thermal maximum and carbon isotope excursion. Earth and Planetary Science Letters 21, 13–26.

Kent, D.V., Tauxe, L., 2005. Corrected late Triassic Latitudes for Continents adjacent to the North Atlantic. Science 307, 240–244.

Kent, D.V., Muttoni, G., 2008. Equatorial convergence of India and early Cenozoic climate trends. Proceedings of the National Academy of Sciences 105 (42), 16065–16070.

King, R.F., 1955. The remanent magnetism of artificial deposited sediments. Mon. Nat. R. Astr. Soc. Geophys. Suppl. 7, 115–134

Kirschvink, J.L., 1980. The least-squares line and plane and analysis of paleomagnetic data. Geophys. J. R. Astron. Soc. 62, 699–718.

Koch, P.L., Zachos, J.C., and Gingerich, P.D., 1992. Correlation between isotope records in marine and continental carbon reservoirs near the Palaeocene/Eocene boundary. Nature 358, 319–322, doi: 10.1038/358319a0.

Kodama, K.P., 1982. Magnetic effects of maghemitization of Plio-Pleistocene marine sediments, Northern California. Journal of Geophysical Research 87 (B8), 7113–7125.

Krauskopf, K.B., 1979. Introduction to geochemistry. In: International Series in the Earth and Planetary Science, ed. Krauskopf, K.B., Emery, K.O., Legget, R.F., Murray, B., Sloss, L.L. 617 pp. New York: McGraw–Hill. 2nd ed.

Kump, L.R., Brantley, S.L., Arthur, M.A., 2000. Chemical weathering, Atmospheric CO_2, and Climate. Annu. Rev. Earth Planet. Sci. 2000. 28, 611–667.

Lowenstein, T.K., Demicco, R.V., 2006. Elevated Eocene atmospheric CO2 and its subsequent decline. Science 313, 1928–1929.

Lowrie, W., 1990. Identification of ferromagnetic minerals in a rock by coercivity and unblocking temperature properties. Geophys. Res. Lett. 17, 150–162.

Lowrie, W., Alvarez, W., 1977. Upper Cretaceous–Paleocene magnetic stratigraphy at Gubbio, Italy: III. Upper Cretaceous magnetic stratigraphy, Geol. Soc. Amer. Bull. 88, 374–377.

Lowrie, W., Alvarez, W., Napoleone, G., Perch-Nielsen, K., Premoli Silva, I., Toumarkine, M. 1982. Paleogene magnetic stratigraphy in Umbrian pelagic carbonate rocks: The Contessa sections, Gubbio. Geological Society of America Bulletin 93, 414–432.

Mackenzie, F.T., Garrels, R.M., 1966. Chemical mass balance between rivers and oceans. Am. J. Sci. 264, 507–525.

Martini, E., 1971. Standard Tertiary and Quaternary calcareous nannoplankton zonation. In: Farinacci, A. (Ed.), Proceedings of the 2nd Planktonic Conference, 2, Ed. Tecnoscienza, Roma, 739–785.

McFadden, P.L., McElhinny, M.W., 1990. Classification of the reversal test in paleomagnetism. Geophys. J. Int. 103, 725–729.

McKenna, M.C., 1980. Eocene paleolatitude, climate, and mammals of Ellesmere Island. Palaeogeogr. Palaeoclimatol. Palaeoecol. 30, 349–362.

Miller, K.G., Wright, J.D., Fairbanks, R.G., 1991. Unlocking the ice house: Oligocene-Miocene oxygen isotopes, eustasy, and margin erosion. Journal of Geophysical Research 96, 6829–6848.

Miller, K.G., Wright, J.D., Browning, J.V., 2005. Visions of ice sheets in a greenhouse world, Marine Geology 217, 215–231.

Monechi, S., Thierstein, H.R., 1985. Late Cretaceous–Eocene nannofossil and magnetostratigraphic correlations near Gubbio, Italy. Mar. Micropaleontol. 9, 419–440.

Moran, K., Backman, J., Brinkhuis, H., Clemens, S.C., Cronin, T., Dickens, G.R., Eynaud, F., Gattacceca, J., Jakobsson, M., Jordan, R.W., Kaminski, M., King, J., Koc, N., Krylov, A., Martinez, N., Matthiessen, J., McInroy, D., Moore, T.C., Onodera, J., O'Regan, M., Pälike, H., Rea, B., Rio, D., Sakamoto, T., Smith, D., Stein, R., St John, K., Suto, I., Suzuki, N., Takahashi, K., Watanabe, N., Yamamoto, M., Farrell, J., Frank, M., Kubik, P., Jokat, W., Kristoffersen, Y., 2006. The Cenozoic palaeoenvironment of the Arctic Ocean. Nature 441, 601–605.

Muttoni, G., 1995. "Wasp-waisted" hysteresis loops from a pyrrhotite and magnetite-bearing remagnetized Triassic limestone. Geophysical Research Letters 22 (23), 3167–3170.

Muttoni, G., Garzanti, E., Alfonsi, L., Cirilli, S., Germani, D., Lowrie, W., 2001. Motion

of Africa and Adria since the Permian: paleomagnetic and paleoclimatic constraints form northern Libya. Earth and Planetary Science Letters 192, 159–174.

Muttoni, G., Kent, D.V., Garzanti, E., Brack, P., Abrahamsen, N., Gaetani, M., 2003. Early Permian Pangea “B” to Late Permian Pangea “A”. Earth Planet. Sci. Lett. 215, 379–394.

Muttoni G., Kent D.V., Garzanti E., Brack P., Abrahamsen N., & Gaetani M., 2004. Erratum to Early Permian Pangea "B” to LatePermian Pangea “A”: [Earth Planet Sci. Lett. 215, 2003, 379–394]. Earth Planet. Sci. Lett. 218, 539–540.

Muttoni, G., Kent, D.V., 2007. Widespread formation of cherts during the early Eocene climate optimum. Palaeogeogr. Palaeoclimatol. Palaeoecol. 253, 348–362.

Napoleone, G., Premoli, Silva, I., Heller, F., Cheli, P., Corezzi, S., Fischer, A.G., 1983. Eocene magnetic stratigraphy at Gubbio, Italy, and its implications for Paleogene geochronology. Geological Society of America Bulletin 94, 181–191.

Okada, H., Bukry, D., 1980. Supplementary modification and introduction of code numbers to the low-latitude coccolith biostratigraphic zonation (Bukry, 1973; 1975). Mar. Micropaleontol. 5, 321–325.

Özdemir, Ö., Dunlop, D.J., 1988. Crystallization remanent magnetization during the transformation of maghemite to hematite. Journal of Geophysical Research 93 (B6), 6530–6544.

Pagani, M., Zachos, J.C., Freeman, K.H., Tipple, B., Bohaty, S., 2005. Marked decline in atmospheric carbon dioxide concentrations during the Paleogene. Science 309, 600–603.

Pagani, M., Caldeira, K., Archer, D., Zachos, J.C., 2006. An ancient carbon mistery. Science 314, 1556-1557. doi: 10.1126/science.1136110

Pearson, P.N., Ditchfield, P., Singano, J., Harcourt-Brown, K.G., Nicholas, C.J., Olsson, R.K., Shackleton, N., Hall, M.A., 2001. Warm tropical sea surface temperatures in the Late Cretaceous and Eocene epochs. Nature 413, 481–487.

Perch-Nielsen, K., 1985. Cenozoic calcareous nannofossils. In: Bolli, H.M., et al. (Ed.), Plankton Stratigraphy. Cambridge University Press, New York, 427–554.

Raffi, I., Backman, J., Pälike, H., 2005. Changes in calcareous nannofossil assemblage across the Paleocene/Eocene transition from the paleo-equatorial Pacific Ocean. Palaeogeogr. Palaeoclimatol. Palaeoecol. 226, 93–126.

Rio, D., Raffi, I., Villa, G., 1990. Pliocene–Pleistocene calcareous nannofossil distribution patterns in the western Mediterranean. Proc. Ocean Drill. Program Sci. Results 107, 513–533.

Robert, C., Kennett, J.P., 1994. Antartic subtropical humid episode at the Paleocene–Eocene boundary: Clay-mineral evidence. Geology 22, 211–214.

Roberts, A.P., Cui, Y., Verosub, K.L., 1995. Wasp-waisted hysteresis loops: Mineral characteristic and discrimination of components in mixed magnetic systems. Journal of Geophysical Research 100 (B9), 17909–17924.

Röhl, U., Westerhold, T., Bralower, T.J., Zachos, J.C., 2007. On the duration of the Paleocene-Eocene thermal maximum (PETM). Geochemestry Geophysic Geosystem 8,Q12002 ,doi:10.1029/2007GC001784.

Rosenbaum, G., Lister, G.S., Duboz, C., 2004. The Mesozoic and Cenozoic motion of Adria (central Mediterranean): a review of constraints and limitations. Geodin. Acta 17 (2), 125–139.

Schmitz, B., Pujalte, V., 2007. Abrupt increase in seasonal extreme precipitation at the Paleocene-Eocene boundary. Geolog. Soc. of America 35, 215–218.

Schwertmann U., 2008. Iron Oxides, in: Chesworth W., Encyclopedia of Soil Science, *Springer*, Netherland, pp. 363-369.

Singer, M.J., Verosub, K.L., Fine, P., TenPas, J., 1996. A conceptual model for the enhancement of magnetic susceptibility in soils. Quaternary International 34–36, 243–248.

Sloan, L.C., Rea, D.K., 1995. Atmospheric carbon dioxide and early Eocene climate: A general circulation modeling sensitivity study. Palaeogeography, Palaeoclimatology, Palaeoecology 119, 275–292.

Stefani, C., Grandesso, P., 1991. Studio preliminare di due sezioni del Flysch Bellunese. Rendiconti della Società Geologica Italiana 14, 157–162.

Sundquist, E.T., 1991. Steady state and non-steady state carbonate-silicate controls on atmospheric CO_2. Quaternary Sci. Rev. 10, 283–296.

Svensen, H., Planke, S., Malthe-Sørenssen, A., Jamteveit, B., Myklebust, R., Rasmussen Eidem, T., Rey, S.S., 2004. Release of methane from a volcanic basin as a mechanism for initial Eocene global warming. Nature 429, 542–545.

Tauxe, L., 2010. Essentials of Paleomagnetism, Univ. California Press, Berkeley.

Tauxe, L., Kent, D.V., 1984. Properties of detrital remanence carried by hematite from study of modern river deposits and laboratory redeposition experiments. Geophys. J.

Roy. Astr. Soc. 76, 543–561.

Tauxe, L., Kent, D.V., 2004. A simplified Statistical Model for the Geomagnetic Field and the Detection of Shallow Bias in Paleomagnetic Inclinations: Was the Ancient Magnetic Field Dipolar? In: J.E.T. Channell, D.V. Kent, W. Lowrie and J.G. Meert, Editors, 2004. *Timescales of the paleomagnetic field*, *AGU monograph*, American Geophysical Union, Washington, DC.

Tauxe, L., Mullender, T.A.T., Pick, T., 1996. Potbellies, wasp-waists, and superparamagnetism in magnetic hysteresis. Journal of Geophysical Research 101 (B1), 571–583.

Tauxe, L., Kodama, K.P., Kent, D.V., 2008. Testing corrections for paleomagnetic inclination error in sedimentary rocks: A comparative approach. Physics of the Earth and Planetary Interiors 169, 152–165.

Thomas, E., Shackleton, N.J., 1996. The Paleocene-Eocene benthic foraminiferal extinction and stable isotope anomalies, in Knox, R.W.O'B., et al., eds., Correlation in the Early Paleogene in Northwest Europe: Geological Society of London Special Publication 101, 401–441.

Thomas, D.J., Bralower, T.J., 1999. New evidente for subtropical warming durino the late Paleocene thermal maximum: Stable isotopes from Deep Sea Drrilling Project Site 527, Walvis Ridge. Paleoceanography 14 (5), 561–570.

Thomas, E., 2008. Descent into the Icehouse. Geology 36(2), 191–192.

Torrent, J., Barrón, V., Liu, Q., 2006. Magnetic enhancement is linked to and predes hematite formation in aerobic soil. Geophysical Research Letters 33, L02401, doi: 10.1029/2005GL024818.

Velbel, M.A., 1993. Temperature dependance of silicate weathering in nature: How strong a negative feedback on long-term accumulation of atmospheric CO_2 and global greenhouse warming? Geology 21, 1059–1062.

Walker, J.C.G., Hays P.B., Kasting, J.F., 1981. A negative feedback mechanism for the long-term stabilization of the Earth's surfaces temperature. Journal of Geophysical 86, 9776–9782.

Wang, X., Yang, Z., Løvlie, R., Min, L., 2004. High-resolution magnetic stratigraphy of fluvio-lacustrine succession in the Nihewan Basin, China. Quaternary Science Reviews 23, 1187–1198.

Watson, G., 1983. Large sample theory of the Langevin distributions. J. Stat. Plann. Inference 8, 245–256.

Wilson, M.J., 2004. Weathering of the primary rock-forming minerals: processes, products and rates. Clay Minerals 39, 233–266.

Winterer, E.L., Bosellini, A., 1981. Subsidence and sedimentation on Jurassic passive continental margin, Southern Alps, Italy. American Association of Petroleum Geologists Bulletin 65, 394–421.

Wise, S.W., Breza, J.R., Harwood, D.M., Wei W., 1991. Palaeogene glacial history of Antarctica. In: Mãœller III, D.W., McKenzie, J.A., Weissert, H. (Eds.), Controversies in Modern Geology: Evolution of Geological Theories in Sedimentology, Earth History and Tectonics. Academic Press, London, 133–171.

Wolfe, J.A., 1980. Tertiary climates and floristic relationships at High latitudes in the northern hemisphere, Palaeogeogr. Palaeoclimatol. Palaeoecol. 30, 313–323.

Yapp, C.J. 2004. Fe(CO3)OH in goethite from a mid-latitude North American Oxisol: estimate of atmospheric CO2 concentration in the Early Eocene "climatic optimum". Geochimica et Cosmochimica Acta 68(5), 935-947.

Zachos, J.C., Stott, L.D., Lohmann, K.C., 1994. Evolution of marine temperatures during the Paleogene, Paleoceanography 9, 353–387.

Zachos, J.C., Pagani, M., Sloan, L., Thomas, E., Billups, K., 2001. Trends, Rythms and Aberrations in Global Climate 65 Ma to Present. Science 292, 686–693.

Zachos, J.C., Wara, M.W., Bohaty, S., Delaney, M.L., Petrizzo, M.R., Brill, A., Bralower, T.J., Premoli Silva, I., 2003. A transient rise in tropical sea surface temperature during the Paleocene-Eocene thermal maximum. Science 302, 1551–1554.

Zachos, J.C., Röhl, U., Schellenberg, S.A., Sluijs, A., Hodell, D.A., Kelly, D.C., Thomas, E., Nicolo, M., Raffi , I., Lourens, L.J., McCarren, H., and Kroon, D., 2005. Rapid acidification of the ocean during the Paleocene-Eocene thermal maximum. Science 308, 1611–1615. doi: 10.1126/science.1109004.

Zattin, M., Cuman, A., Fantoni, R., Martin, S., Scotti, P., Stefani, C., 2006. From Middle Jurassic heating to Neogene cooling: The thermochronological evolution of the southern Alps. Tectonophysics 414, 191–202.

Zijderveld, J.D.A., 1967. A.C. demagnetization of rocks: analysis of results. In: Collinson, D.W. et al., eds., 1967. Methods in Paleomagnetism, Elsevier, Amsterdam, 254–286.